Chi Meson Production in Proton-Antiproton Interactions at a Center of Mass Energy of 1.8 TeV

by

Christopher Mark Boswell

A dissertation submitted to

The Johns Hopkins University

in conformity with the requirements for the

degree of Doctor of Philosophy

Baltimore, Maryland

November, 1993

Chi Meson Production in Proton-Antiproton Interactions at a Center of Mass Energy of 1.8 TeV

Christopher Mark Boswell, *The Johns Hopkins University*, 1993.

Abstract

We report the full reconstruction of χ_c mesons through the decay chain $\chi_c \rightarrow J/\psi\ \gamma$, $J/\psi \rightarrow \mu^+\ \mu^-$, using data obtained at the Collider Detector at Fermilab in $\bar{p}\ p$ collisions at $\sqrt{s} = 1.8$ TeV. This exclusive χ_c sample, the first observed at $\sqrt{s} = 1.8$ TeV, is used to measure the χ_c meson production cross section times branching fractions. We obtain $\sigma \cdot Br = 3.2 \pm 0.4(\text{stat}) \pm^{1.2}_{1.1}(\text{syst})$ nb for χ_c mesons decaying into J/ψ mesons with $P_T > 6.0$ GeV/c^2 and pseudorapidity $|\eta| < 0.5$. From this and the inclusive J/ψ cross section we calculate the inclusive b-quark cross section to be 12.0 ± 4.5 μb for $p_T^b > 8.5$ GeV/c and $|y^b| < 1$.

This thesis was prepared under the guidance of Professor Bruce A. Barnett.

Acknowledgements

To begin with, I would like to thank the maker of subatomic particles. They are cool, and I hope you like my study of them.

I would also like to thank my parents. Mom, you've always shown me love and support. Dad, you've encouraged me from the beginning right down to the wire, plus taught me to make my first physical measurements one day with your aviator stopwatch for timing the distance of lightning using thunder. I love you both.

I would like to thank the people of the CDF collaboration, each of which made this measurement possible. Thanks are especially due to a few individuals: Tim Rohaly, for using J/ψ's to first look at B and χ_c physics, and having a good attitude about being a graduate student. Avi Yagil, for first using a low energy electron/photon finder to reconstruct χ_c mesons, for being so helpful in this analysis, and for being a general fun guy. Bob Blair, for so much help on the details of photons in our detector and the efficiency measurement, along with photon guys Steve Kuhlmann and Rob Harris, and the whole γ group. (Those evil photon guys, eh, Avi?) Richard Hughes, who trudged through some of these efficiency calculations as a pioneer. Fritz DeJongh, as a B-physics starter. Alain Gauthier and Dan Frei, muon types who really laid some groundwork. Alberto Etchegoyen (hope things are well in Argentina) Vaia Papadimitriou, and Theresa Fuess for the J/ψ and $\psi(2S)$ expertise. Paris Sphicas and Allesandra Caner, for help on the ISACHI Monte Carlo generator. Michelangelo Mangano for more help with Monte Carlo generation, and χ_c production in general. Bill Carithers, Jaco Konigsberg, and Mike Albrow, for godfathering the analysis and many good suggestions. Jim Mueller for B expertise, and Barry Wicklund who always seems to understand what's going on. And, of course, since it is late, I've forgotten you. Yes, you! But you know that I'm thinking of you.

Many thanks to Nigel Glover for the discussions on J/ψ production, the theory curves plotted for us and all the other studies.

Thanks also to Brian Harral, and I'm glad you were out there for a while. Slack be unto you. What a kind guy. What else is there to say, maybe we'll be related somehow someday?

Steve Vejcik deserves special thanks. Man, it was cool living out there, and we are more or less sane. Thanks for all your help, and the discussions – if people could think like you or I, we'd still all disagree, but at least we could talk about it. Thanks for the friendship.

While I'm at it, thanks to all the vermin: Steve, Colin, Amy, Dan, and Mark. Dudes! Hi Judy, thanks for the pitchers. Bob Mattingly, here's to you. Alan and Jeff, you guys have definately learned to hone the grad student cynicism. Keep up the good work.

To John Ellison and the whole UCR D0 group: thanks for the opportunities and the support.

Thanks, also to Rick Snider, who was so instrumental in getting the synopsis of this analysis published (finally, in Physical Review Letters 71 2537-2541 (1993), alright! Thanks so much for the help).

Thanks a million to my advisor, Bruce Barnett, who went to bat for me so many times in my early grad school career and helped make this thesis as good as it is. I've learned a lot. One hears a great many stories about graduate advisors, and I'm glad to have had one of the good ones.

Thanks most of all to my wife, Amy, who was willing to be courted by a graduate student, and has survived the process. Thank you, dearest, for all the good and for weathering the difficult.

Contents

Chapter 1

Introduction

> And God blessed them, and God said unto them"Be fruitful, and multiply, and fill the earth, and conquer it: and have dominion..." Genesis 1:28

With these words, some say, the process of mankind discovering, modeling, and controlling physical processes and entities began [1]. The frontiers of this discovery process have utilized a method of model testing useful for finding either a need for minor alterations or variations of the model, or pointing the way for some to propose entirely new models [2]. This thesis measures the rate of a process that has been calculated in the framework of current physical models, in the hope of verifying the model or showing differences which need to be addressed. It is expected that minor tuning is all that will need to be performed on the model to match the measurement.

1.1 Physics to High Energy Particle Physics

The attempt to understand what the world is made of and how it works has a long history, full of the stories of people who made discoveries or descriptions we deem important today.

However, the history of science is primarily the history of physical models. These models are like "maps" describing the ordered universe. The apparent atomic order, or structure of the behavior of the elements, was codified by Mendeleev and pointed the way to atomic substructure. Maxwell's equations remain the mathematical model for classical electromagnetism, used today to describe such things as radio signal propagation. The discovery of electrons and nucleons resulted in an atomic model describing why Mendeleev's structure works. The nucleons, neutrons and protons, form the nucleus of an atom, with the electrons in the space around the nucleus. Additionally, quantum mechanics, which arose initially for describing the radiation spectra of warm bodies, is a model well suited to characterize the behavior of atomic spectra. Finally, the "particle zoo" or proliferation of discovered particles after the advent of the particle accelerator, led to the quark model, depicting nucleons as made of partons called quarks.

1.2 The Standard Model

The current representation of our knowledge of the makeup of the physical world delineates matter into families of fundamental fermions (quarks and leptons), with forces being mediated by fundamental bosons. Table 1.1 contains the names of the fundamental fermions. These each have antimatter counterparts. Thus an anti-c quark is delineated as a $\bar{c}$ quark. Each column in this table is a group called a family. Most matter is made of bound states of the charged fermions in the first family. For example, the proton is a bound state of three quarks, uud, and a neutron is a bound state of three quarks, udd. The binding is done by the strong bosons, called gluons, which will be discussed in more detail in the next section. The forces providing this binding are described as following from interactions of bosons. For instance, electromagnetic forces can be thought of as interchanges of photons,

leptons	charge 0	ν_e	ν_μ	(ν_τ ?)
leptons	charge -1	e	μ	τ
quarks	charge $+\frac{2}{3}$	u	c	(t ?)
quarks	charge $-\frac{1}{3}$	d	s	b

Table 1.1: The fundamental fermions of the Standard Model.

the most common fundamental boson. Photons are "particles of light". The photon, γ, has no antiparticle (or is its own antiparticle), and no charge. The description of quantum electrodynamics, or QED, has been extremely successful in predicting the behavior of charged particles.

There are weak forces which are understood as being interchanges of more massive bosons, the W^+, W^- and Z^0 bosons. These weak interactions include those like the diagram in Figure 1.1 which is responsible for β decay of neutrons, $n \rightarrow e^- \bar{\nu}_e p$. The photon and

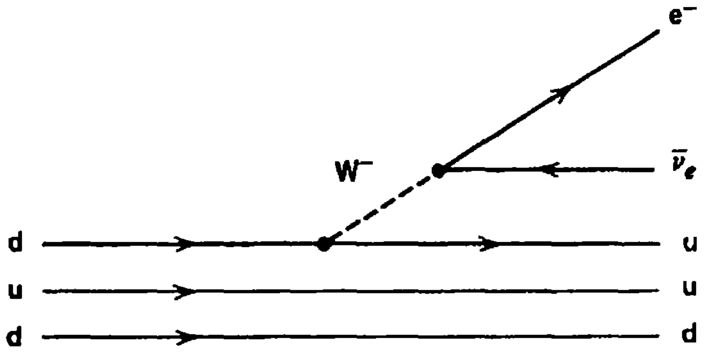

Figure 1.1: A diagram of beta decay

the weak bosons are seen to be interrelated [3], and all four are known as the electroweak bosons.

Mesons are bound states of a quark and an antiquark. For instance, a B_u^+ meson is a bound state of $\bar{b}u$, while a B_d^0 meson is $\bar{b}d$. Any meson containing only one b or $\bar{b}$ is termed a B meson, in general, or also a bottom meson or a b-flavored meson. The $\bar{b}b$ mesons are a special case briefly mentioned in Section 1.5. The naming of mesons by their quark content is discussed in detail in Reference [4].

1.3 QCD

In addition to explaining the electroweak forces, the current models attempt to explain the so called strong forces. These are the forces which are thought to bind quarks together to form mesons ($q\bar{q}$ bound states) or baryons (qqq or $\bar{q}\bar{q}\bar{q}$ bound states). It was called the strong force because the magnitude of this binding energy is higher, and the coupling between the boson and fermion fields is larger, than for the other known forces.

Due to the rather unique three-fold symmetry needed to describe strong interactions, this field is called quantum chromodynamics, or QCD, drawing an analogy to color theory, where red + green + blue = colorless. The QCD model starts with fundamental bosons called gluons which carry the strong force via "color charge". Each quark can be in any of three colors, actually called red, green, and blue. Antiquarks come in anticolors, and gluons carry a color and an anticolor, such as a red-antigreen gluon. Any free particle state must be colorless, which explains why no free quark or free diquark bound states exist. The strong coupling, α_s, is dependent on the energy of the given interaction. In fact, α_s decreases as the energy increases.

This decreasing of the QCD coupling with increasing energy is due to the gluon self coupling, and is called anti-screening (analogous to the screening that allows the charges in electromagnetism to appear less strong at larger distances). The self coupling leads to a

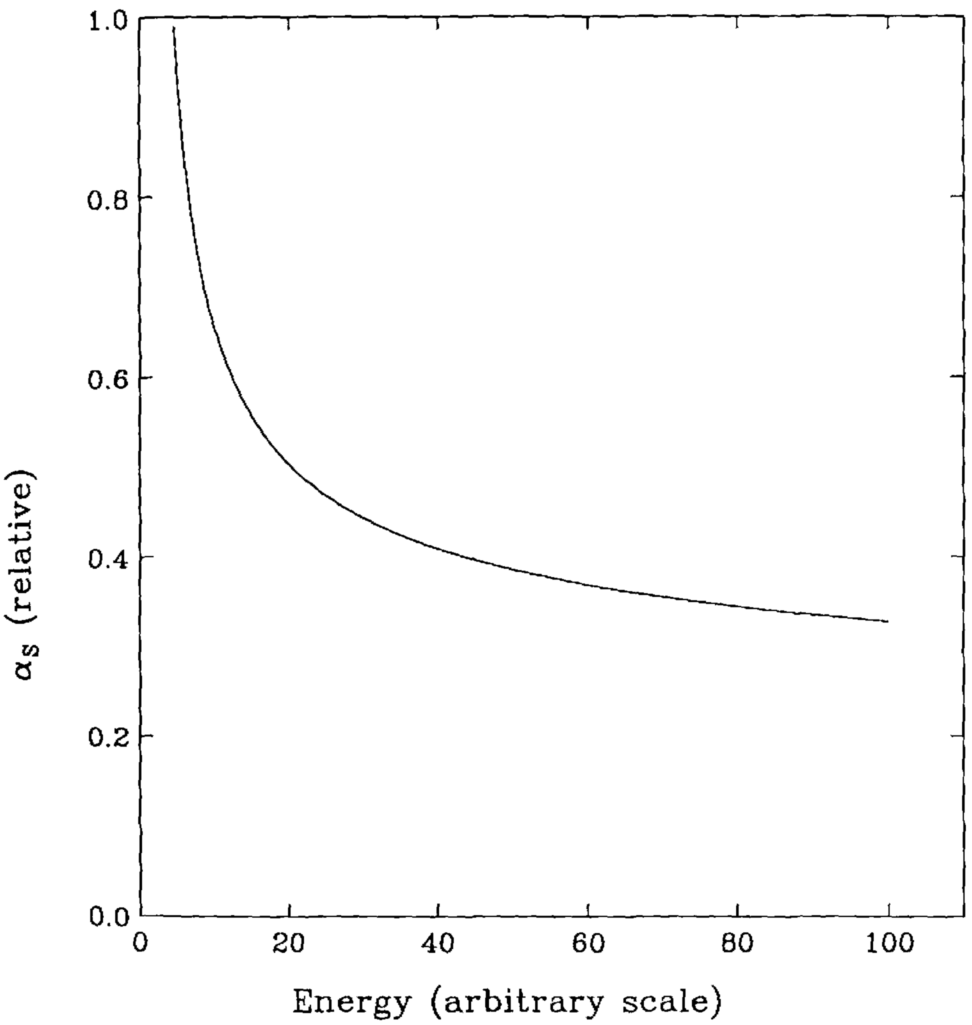

Figure 1.2: The energy dependence of α_s

decreasing dependence of the strong coupling constant α_s on the energy of the interaction, as shown in Figure 1.2. At higher values of energy, there is less coupling strength, while at lower energies, the coupling is higher. The higher energies probe smaller distances, and the low coupling region is termed the asymptotic freedom region.

1.4 Interactions

Discussion of the processes in the model will include mention of quantities which depend on the energies and momenta of the particles involved. It is therefore useful to define some of these quantities by examination of a simple two-body reaction. Figure 1.3 shows a schematic of a two-body process, with particles labelled (1) and (2) coming in, and particles labelled (3) and (4) flying out. The momenta and masses of these particles are labelled p_i and m_i, where i is the label number.

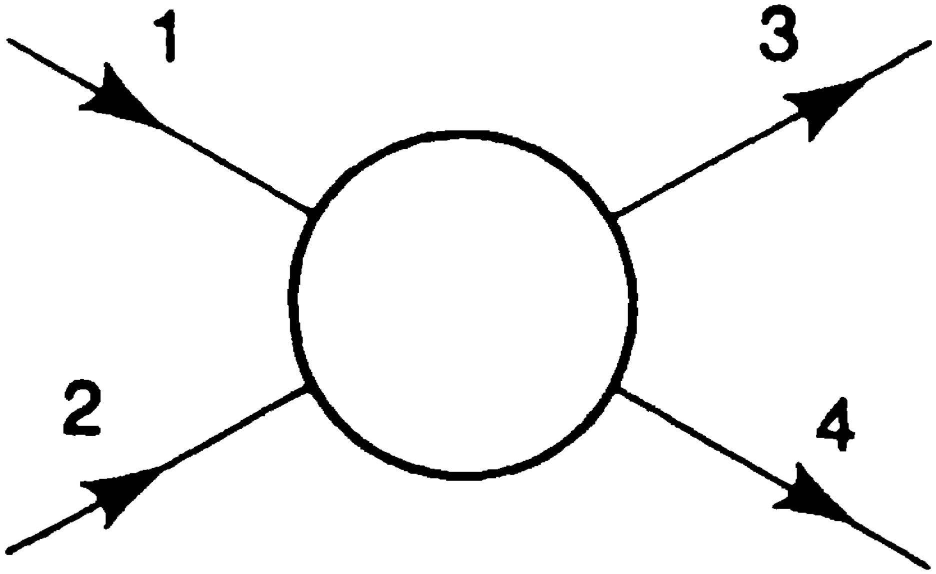

Figure 1.3: A two-body reaction

The first set of variables to be defined are the Lorentz invariant Mandelstam variables, s, t and u, defined by

$$s = (p_1 + p_2)^2 = (p_3 + p_4)^2 \tag{1.1}$$

$$t = (p_1 - p_3)^2 = (p_2 - p_4)^2 \tag{1.2}$$

$$u = (p_1 - p_4)^2 = (p_2 - p_3)^2 \tag{1.3}$$

which satisfy the relationship

$$s + t + u = m_1^2 + m_2^2 + m_3^2 + m_4^2. \tag{1.4}$$

The entire energy available in the center of momentum frame of the interaction is

$$E_{cm} = \sqrt{s}. \tag{1.5}$$

Reaction rates for particle interactions can be conveniently quantified by a cross sectional area. This is an effective area which the particles present to one another for each specific process (or final state). The name for the units for cross section, σ, probably arose from jokes about being able to hit a broad side of a barn. The barn (b) is defined by $1b = 10^{-28}m^2$, and many high energy processes have cross sections on the order of 10^{-9} barns, or a nanobarn (nb). Likewise one picobarn (pb) is 10^{-12} barns. The reaction rate measured in this thesis is expressed in nanobarns.

There are additional variables useful in colliders where the incoming particles are heading toward one another down the beamline, as mentioned in Chapter 3. The momentum of any particle can be decomposed into the momentum parallel to the beam (p_z if the z direction is defined to be the z-axis direction), and the momentum transverse to the beam (p_T). Another useful quantity, to determine the angle a particle is travelling with respect to the beamline, is the pseudorapidity η, defined from the momentum by $\eta = \frac{1}{2} ln \frac{p+p_z}{p-p_z}$.

As mentioned previously, the forces are carried by the exchange of bosons. If the four momentum of the boson is Q, the quantity Q^2 is Lorentz invariant and a useful measure of the momentum transfer or energy of the interaction. It should be noted that Q^2 is not the mass squared of the boson (unless the boson doesn't interact ever again) and thus the boson is virtual, or "off the mass shell".

Of course, since protons are made of quarks and gluons, any description of proton interactions with sufficiently high energy to probe this substructure must take this into account. At the energies discussed in the following chapters, it is necessary to define the Mandelstam variables for the incoming quarks and gluons for a given partonic interaction, given the labels $\hat{s}$, $\hat{t}$ and $\hat{u}$. These allow calculation of the partonic cross sections $\hat{\sigma}$, that piece of the total cross section coming from the parton in question. The observable cross section is a sum of the $\hat{\sigma}$ from each of the types of partons coming in, as well as integrated over the initial parton distributions. If x is $p(parton)/p(nucleon)$, the probability distribution that a parton will have a momentum fraction x is given by $F(x, Q^2)$. Note that the distribution not only depends on the momentum fraction, but also varies with the momentum transfer probing the interaction Q^2. The total cross section is calculated by

$$\sigma = \Sigma \int F_a(x_1, Q^2) F_b(x_2, Q^2) \hat{\sigma} dx_1 dx_2 \tag{1.6}$$

where the sum is over the different types of initial particles a and b. The types of initial particles are the constituents of the nucleons being collided, like gluons and quarks.

1.5 Quarkonia

With the discovery of the J/ψ mesons [5], and the description of the spectroscopy of the $c\bar{c}$ system [6], and later the Υ meson ($b\bar{b}$) system [7], the physics of heavy quark - heavy antiquark bound systems was on its way. These mesons, called quarkonia, or just 'onia' signified by the symbol $\mathcal{O}$, are bound states of a heavy quark and its anti-quark. Since the masses of the heavy quarks $Q = c$ or b are very large, they provide a $Q\bar{Q}$ bound-state size small enough to come near to the asymptotically free regime of the binding α_s. This means the $Q\bar{Q}$ system is probably well described by a perturbative QCD theory. (Mesons with smaller quark masses are not described well by the first few orders of perturbative QCD). Comparison of perturbative calculations with experimental observations has yielded information of the strong interaction. In fact, the J/ψ and the $\psi(2S)$ were the only charmonia mesons discovered when the relative masses of the other states were predicted [6], especially the three triplet P states known as the χ_c states. The production rate of these χ_c states in the $\bar{p}p$ interactions is the subject of this thesis.

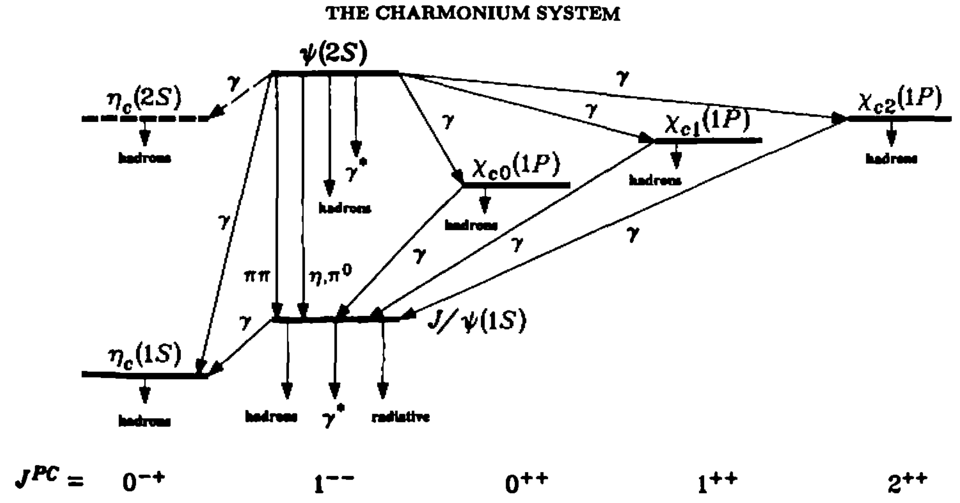

Figure 1.4: The charmonium system, from Reference [4]. Uncertain states are indicated by dashed lines, and undiscovered states expected are not shown.

The $Q\bar{Q}$ states exhibit a spectroscopy of different energy levels and quantum numbers, analogous to atomic spectra, or energy levels in the positronium (e^+e^-) bound state. The charmonium system, of $c\bar{c}$ bound states, is summarized in Figure 1.4, and the $b\bar{b}$ states are summarized in Figure 1.5. The mesons are represented in these figures as a line above the

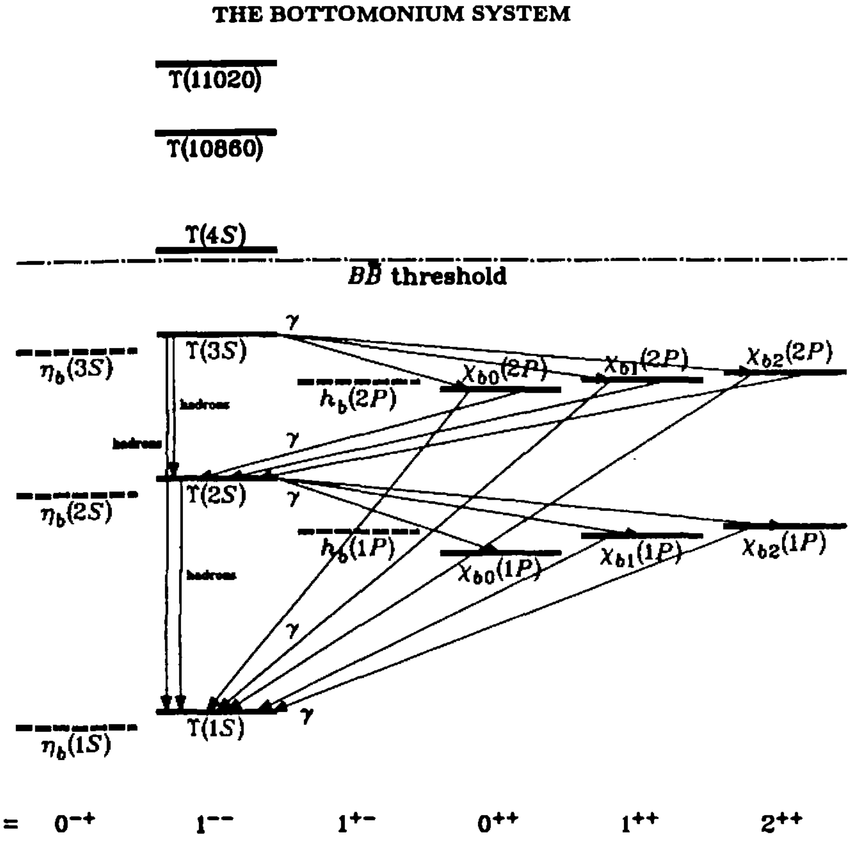

Figure 1.5: The $b\bar{b}$ system, from Reference [4]. Uncertain states are indicated by dashed lines.

respective quantum numbers of each state, higher for the higher mass states, and showing allowed decays and transitions. The quantum numbers shown are total angular momentum (J), parity (P), and charge conjugation (C) quantum numbers. Other representations of these states can be written in terms of the orbital angular momentum (L), and the spin (S) along with J in spectroscopic notation, written in the form $^{2S+1}L_J$. In spectroscopic notation, instead of writing the number value for L, it is denoted by a letter code (S for $L = 0$, P for $L = 1$, D for $L = 2$, etc. [8]). Thus the η_c states are $^1S_0$ states, while the J/ψ meson is the first $^3S_1$ state. The radial excitations are named with the principal quantum numbers, and since the naming scheme for hadrons [4] includes the rule that $^3\mathrm{S}_1$ states above the J/ψ are named with the greek letter ψ, the next state is labelled the $\psi(2S)$. The $^3\mathrm{P}_J$ states of charmonia are labelled by χ_{cJ}, or χ_{c0},χ_{c1}, and χ_{c2}. The $b\bar{b}$ system has a similar naming scheme with Υ denoting the $^3\mathrm{S}_1$, and η_b and χ_{bJ} used for the $^1\mathrm{S}_0$ and $^3\mathrm{P}_J$ mesons respectively.

The χ_c states can decay electromagnetically into a photon and a J/ψ. This is not the only decay mechanism for the χ_c states, but can be significant, (27.3 ± 1.6)% for $\chi_{c1} \rightarrow J/\psi\gamma$ [4]. The $^3\mathrm{S}_1$ states, having the same quantum numbers as the photon, can decay via the annihilation of the c and $\bar{c}$ through a virtual photon which can lead to many final states, including $\mu^+\mu^-$. Decays into one virtual gluon are forbidden since the mesons must be color neutral, and 2 gluon decays are accessible only from the states with $C = +1$. Thus the J/ψ and $\psi(2S)$ states would decay by three gluons or more. The dilepton final states can be readily identified (as will be shown in subsequent chapters), so the decays which will be reconstructed here are $\chi_c \rightarrow J/\psi\gamma$, with $J/\psi \rightarrow \mu^+\mu^-$.

1.6 Outline of This Thesis

Some details of the model for charmonia production will be discussed in Chapter 2, listing the processes to be investigated. The assumptions of this model will be pointed out, and the processes taken into account will be listed.

The devices for producing and observing these particles will be discussed in Chapter 3, with emphasis on those parts of the detector which measure muon and photon properties. Chapter 4 will discuss the collection of the dimuon events with a trigger, and Chapter 5 will delineate the algorithms for reconstruction of the muon and photon candidate objects in the events gathered. The photon reconstruction is central to the $\chi_c \rightarrow J/\psi\gamma$ analysis, and will be examined in detail in Chapter 6.

The determination of the overall efficiency of the reconstruction methods used is discussed in Chapter 7. Details of the final event selection and reconstruction are in Chapter 8. The cross sections are derived from the measurement in Chapter 9, and conclusions are presented in the final chapter.

Chapter 2

Charmonia Production

All charmonia states can be produced in hadronic collisions, and studies of the hadronic production of these states have yielded more tests for production models than e^+e^- collisions. At low p_T, the lowest order diagrams (See Figure 2.1) are important, with $gg \rightarrow \mathcal{O}$

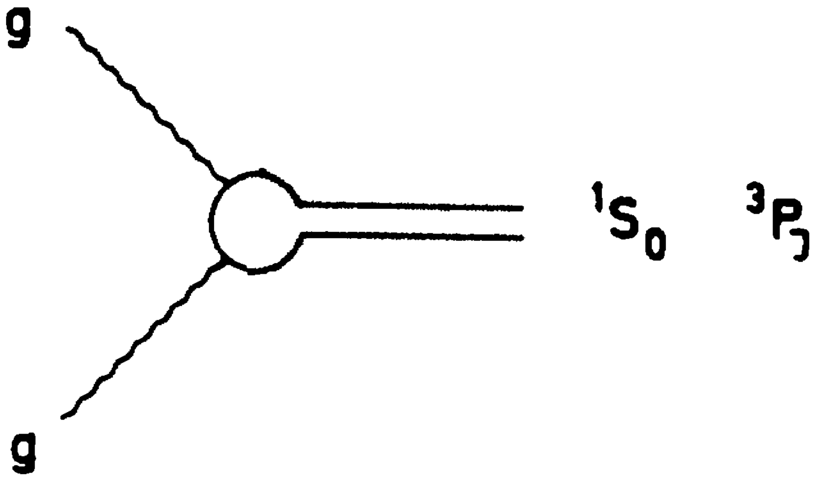

Figure 2.1: Lowest order diagrams for charmonia production

becoming increasingly dominant (compared to low p_T $qq \rightarrow \mathcal{O}$) as the (energy) $\hat{s}$ of the reaction increases [9, 10]. (The J/ψ is not made by $gg \rightarrow J/\psi$, because of charge conjugation invariance (The J/ψ and $\psi(2S)$ are C odd eigenstates), so the statements do not all hold equally for χ and J/ψ).

For high p_T charmonia production, higher order diagrams (as in Figure 2.2) become more significant. In fact, the expectation is that the process $gg \rightarrow \mathcal{O}g$ will constitute the majority of the production cross section (over the first order processes discussed above) at collision energies above a few hundred GeV. All these mechanisms are referred to as direct charmonia production.

Charmonia can also arise from the decays of heavier particles. Decays of b-flavored mesons into charmonia (via diagrams like that shown in Figure 2.6) have been observed, and the branching fractions measured in parts per thousand [4]. Because of this the process

$$gg \rightarrow b\bar{b}X \rightarrow BX \rightarrow \mathcal{O}X \tag{2.1}$$

must be taken into account. This process, referred to as indirect charmonia production, can result in high p_T charmonia. From the measured cross section, $\sigma(b)$ [11, 12], and branching fractions of $B \rightarrow J/\psi X$ and $B \rightarrow \chi_{c1}X$, indirect production of charmonia is expected to be significant.

The J/ψ mesons can be produced in ways other than B decay. Feeddown from other charmonia states, such as $\chi_c \rightarrow J/\psi\gamma$ is expected to account for much of J/ψ production. Direct J/ψ production is expected to be small compared to feeddown and B decay production at high transverse momenta [9]. In the following sections, direct χ_c production and $b\bar{b}$ production are outlined.

2.1 Direct Charmonia Production

The theoretical model for direct charmonia production discussed here has been outlined in References [9, 13]. The calculations rest on several assumptions. The first assumption is that $\mathcal{O}$ are non-relativistic $Q\bar{Q}$ bound states (with Q denoting a heavy quark). Most potential models for describing charmonia spectroscopy rest on this assumption. The non-relativistic assumption predicts the proper relative energy levels for the $Q\bar{Q}$ states, but does not work for quark masses smaller than the charm mass. Secondly, it is supposed that at large p_T, $\mathcal{O}$ production is dominated by order α_s^3 processes, as $gg \rightarrow Q\bar{Q}g$, $gq \rightarrow Q\bar{Q}q$, and $qq \rightarrow Q\bar{Q}g$. A series of Feynman diagrams can be imagined where the initial light quarks and/or gluons are constituents of the colliding particles, while the final light quark or gluon result in recoil jets to offset the transverse momentum of the $\mathcal{O}$.

Another major axiom of the model is the mechanism by which these diagrams containing $Q\bar{Q}$ form bound states. It is postulated that the coupling of the bound state $\mathcal{O}$ to the $Q\bar{Q}$ pair is directly determined by the appropriate wave function of the state. The wave function depends on the quantum numbers for spin, angular momentum, and charge conjugation as well as the color singlet nature of the bound state constructed. This implies that the direct formation of heavy resonances occurs at short distances, or at least that the $Q\bar{Q}$ eventually form final states with a probability determined by the quantum wave functions alone. This assumption of direct formation at short distances leads to spin and color selection rules which affect the relative weight of contributions from each diagram. This postulate is taken over an opposing model in which unbound $Q\bar{Q}$ are first produced and then transformed to $\mathcal{O}$ by soft processes, leading to a non-perturbative description [14]. Although it has been attempted [14], production rates would be extremely difficult to calculate for any non-perturbative model.

2.1.1 Matrix Elements

Charmonia production is then calculated starting from the assumptions of the model. Typical Feynman diagrams are shown in Figure 2.2. Those additional diagrams necessary for

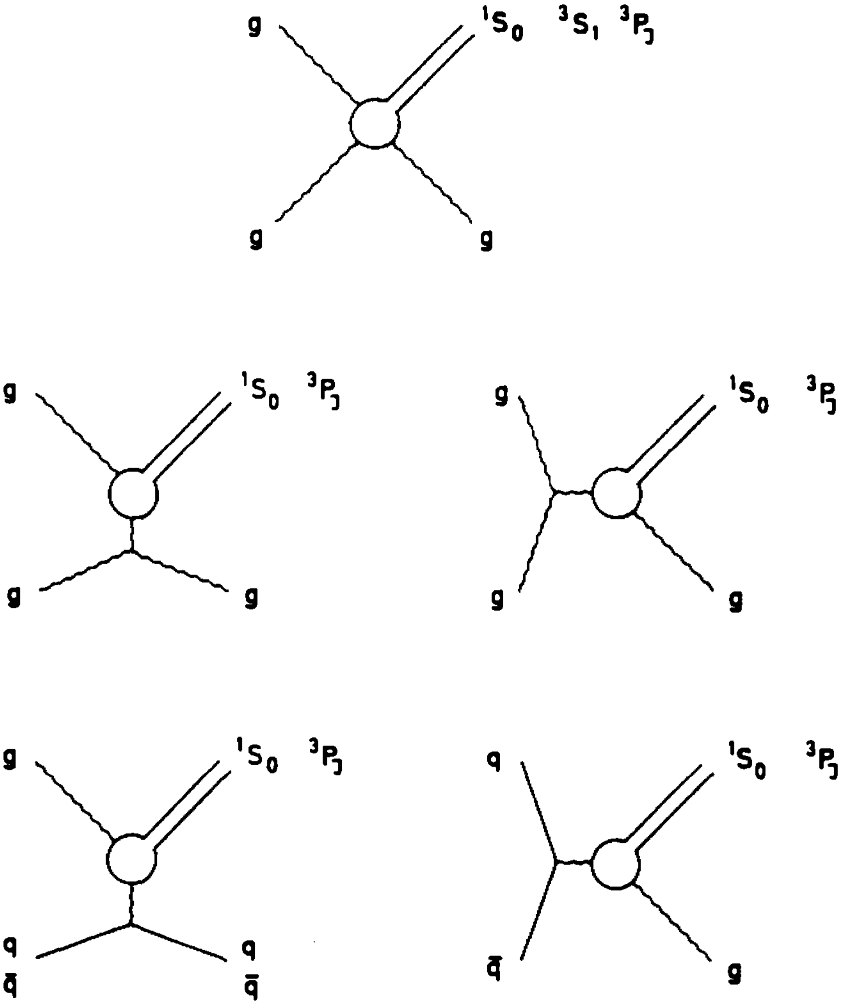

Figure 2.2: Order α_s^3 diagrams for charmonia production, from Reference [17]

gauge-invariant terms in α_s^3 are constructed by permuting the gluon lines. The parton level cross sections have the form [9, 13]:

$$\frac{d\hat{\sigma}}{d\hat{t}} = \frac{\alpha_s^3}{\hat{s}^2}\omega f(ab \rightarrow {}^{2s+1} L_{j\ c}; \hat{s}, \hat{t}, \hat{u}, M^2) \tag{2.2}$$

where f is a function depending only on selection rules, quantum numbers and the variables listed, while ω depends on the wave function. For P-wave states

$$\omega = |R'_P(0)|^2/M^5 \tag{2.3}$$

where $|R'_P(0)|$ is the magnitude of the derivative of the radial part of the wave function, evaluated at the origin and M is the mass of the state.

The full cross section, of course, depends on the parton structure of the colliding particles and is written

$$\frac{d\sigma}{d\hat{t}} = F_1(x_1, Q^2)F_2(x_2, Q^2)K\frac{d\hat{\sigma}}{d\hat{t}}. \tag{2.4}$$

This full cross section calculation has many uncertainties, first among them being uncertainties of the parton structure functions. Second, the strong coupling is calculated by

$$\alpha_s = 12\pi/[(33 - 2n_f)\ln\frac{Q^2}{\Lambda^2}], \tag{2.5}$$

leaving a choice of scale ambiguity (represented by the choice of Q^2/Λ^2). Third, since ω depends on the wave functions, it depends on the potential model used and may not be well known. Finally, a K factor has been introduced to take into account higher order terms, and is an additional uncertainty in the calculation. For these reasons, estimations of the theoretical uncertainties range from ±50% to claims that the predictions should be within an order of magnitude [9, 13, 15, 16, 17, 18, 19].

2.1.2 Theoretical Uncertainties

The inputs to the theoretical calculation of direct charmonia production include many quantities which are not precisely known. The derivative of the wave function at the origin, the scale chosen to compute α_s, and the gluon structure functions will each contribute to the uncertainty. Furthermore, the K factor, explained as a correction for uncalculated higher order terms was chosen primarily to fit experimental results at lower energies [9], specifically J/ψ spectra measured at the ISR [20]. The extrapolation that the cross section at higher energies will contain the same K factor is another assumption of the model.

The derivative of the wave function at the origin has been examined experimentally by measuring the hadronic partial width of χ_c decays. Under the assumptions of the model, the value was found from the partial width of the χ_{c2} state to be $|R'_P(0)|^2 = 0.088 \pm 0.012$ GeV^5 [21]. This leads to a value for $\omega = (1.547 \pm 0.211) \times 10^{-4}$ for the χ_{c2} state. Inputs to most calculations have been in the range $10^{-4} < \omega < 2.3 \times 10^{-4}$ [21]. The effect of any change in ω would be to scale all cross sections by a constant value. Slopes of p_T distributions and relative rates of each angular momentum state would be relatively unaffected.

The calculation of α_s presents a different problem. Since the cross sections will scale as α_s^3, small variations in the Λ^2 choice will be amplified in the cross section measurements. This would change the calculated cross section for all states and momenta. However, changing the momentum transfer from $Q^2 = (p_T^2 + m_\chi^2)/4$ to $Q^2 = m_\chi^2$ (reasonable values due to the uncertainty of the Q^2 of the interaction) would not only change the overall scale, but would introduce p_T dependent effects, which would change the relative production of the χ_c states as well as affecting the calculations of detector acceptance and efficiency.

The gluon structure functions introduce another major theoretical uncertainty. The x values probed in this analysis ran mostly in the range $0.007 < x < 0.02$, while the momentum transfer was around $9 < Q^2 < 200$ GeV^2. The majority of the cross section was at the lower end of both of these ranges. Monte Carlo studies indicated that most substitutions for gluon structure functions available would not change the p_T spectra dramatically, but would change the overall normalization. Using more recent paramaterizations of the structure functions [22] would help in predicting the magnitude of the direct cross section expected, but the acceptance calculations should be relatively unaffected by them [16].

2.2 B Decay to Charmonia

The production rate of b-quarks is thought to be a good place to test QCD. Since the b quark has a large mass, the momentum transfer of any interaction involving b-quarks should also be large, on the order of the mass: $Q^2 \simeq m_b^2$. From Equation 2.5 it is clear that the larger values of Q^2 will provide smaller values of α_s. In b-quark production theories, α_s is about 0.2. This means that the lower order diagrams will be more important than higher order diagrams to the full cross section, since with two gluon vertices in a diagram the contribution is proportional to α_s^2, while three gluon vertices contribute proportional to α_s^3. Each higher order term should be smaller, and, hopefully, perturbative calculations will be precise enough to allow a rigorous test of the production theory.

Models of b-hadron production start with parton-parton scattering. The cross section for b-quark production is calculated. Then, the hadronization of b-quarks into b-hadrons is modelled. The decomposition of the entire process into hard scattering and soft hadronization is a key part of the theory explained here.

2.2.1 b Quark Production

The parton level b quark processes are simplest for the order α_s^2 diagrams, shown in Figure 2.3. Diagrams with three gluon vertices, as in Figure 2.4, will contribute to order α_s^3. Due to interference terms, the order α_s^3 calculation must include the four gluon vertex diagrams such as in Figure 2.5. These interfere with the 3 gluon vertex diagrams, and are taken

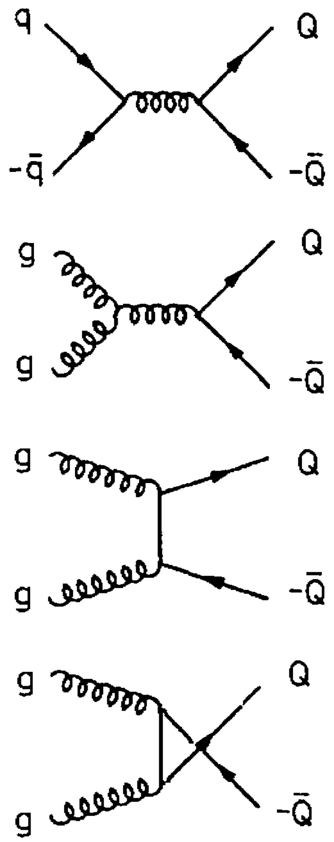

Figure 2.3: Lowest order diagrams for b quark production

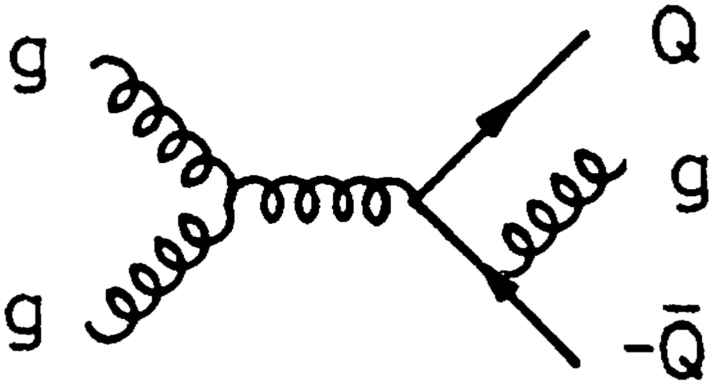

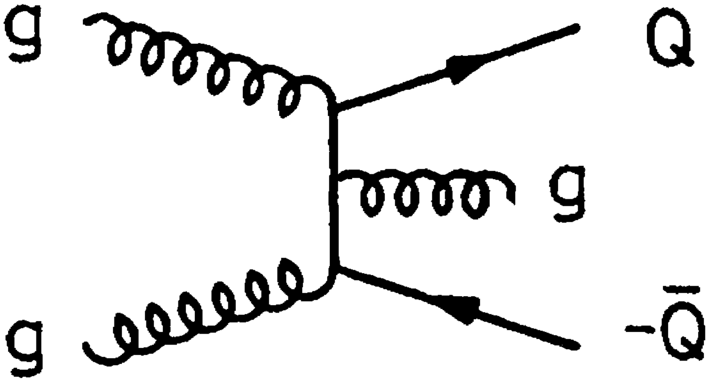

Figure 2.4: Order α_s^3 diagrams for b-quark production

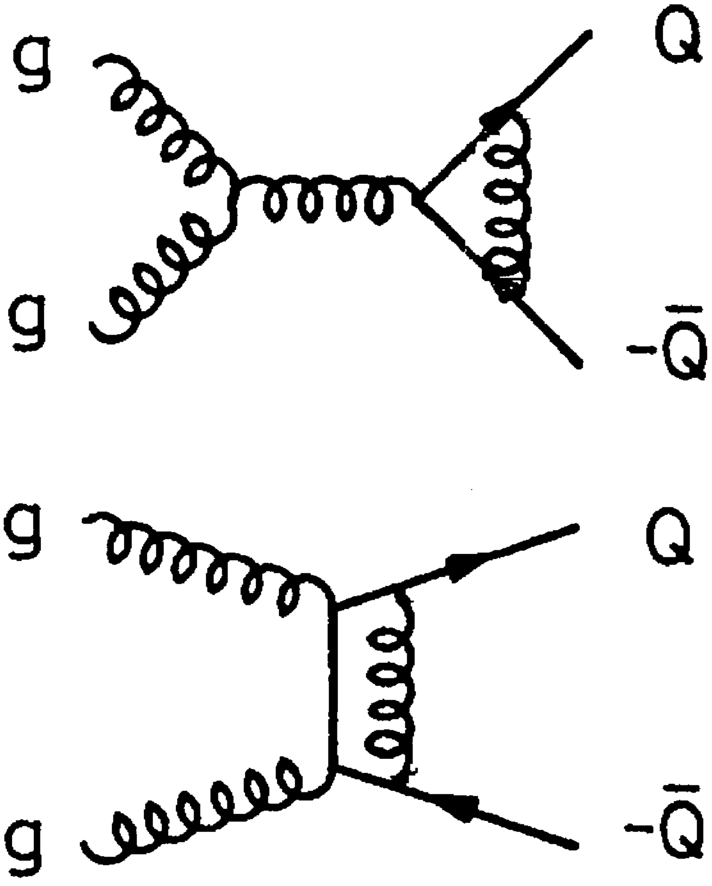

Figure 2.5: Order α_s^4 diagrams for b-quark production

into account in the α_s^3 calculation performed by Nason, Dawson, and Ellis (NDE) [23]. The NDE matrix elements were used in the b Monte Carlos for this analysis.

The details of the NDE calculation will not be described here but it should be noted that the same types of uncertainties arise in this QCD calculation as in the direct χ_c production theory. For instance, the exact Q^2 to use is unclear, and the same range of choices is available, for instance $Q^2 = p_T^2 + m_b^2$ or $Q^2 = 4m_b^2$. The gluon structure function drives the magnitude of the cross section as well. While the larger mass of the b quark should decrease the importance of higher order terms, the value for the mass has an additional uncertainty. For instance, theoretical inputs to models usually place the b quark mass between 4.5 and 5 GeV/c^2.

2.2.2 b Fragmentation

A simulation of b-quark fragmentation relied on the Peterson fragmentation model [24]. The b-hadron was assigned a transverse momentum that was some fraction of the initial quark transverse momentum. If z is the ratio of the final b-hadron p_T and the initial b-quark p_T, the distribution of the number of B-mesons (N) versus z follows

$$\frac{dN}{dz} \propto \frac{z(1-z)^2}{[\epsilon_P z + (1-z)^2]^2} \tag{2.6}$$

with the Peterson parameter ϵ_P an input to the theory. Experimental results indicate $\epsilon_P = 0.006 \pm 0.002$ [25]

When the b-quark pulls an antiquark out of the vacuum to become a meson, the antiquark can be any flavor, although the higher mass flavors are much less likely. In fact, the c and b contributions out of the vacuum can be neglected, and the u and d are about equal. This leads to the definition of λ_s, which is the ratio of s quarks with respect to the two light quarks pulled out of the vacuum, i.e. u:d:s = 1:1:λ_s. Experimentally, λ_s has been measured

Decay	Branching Ratio
$B \to J/\psi X$	$(1.12 \pm 0.16)\%$ [4]
$B \to \psi(2S)X$	$(0.46 \pm 0.20)\%$ [4]
$B \to \chi_{c1}X$	$(0.64 \pm 0.20)\%$ [26]

Table 2.1:

to be around 0.33 to 0.4, giving (with a normalization change)

$$u : d : s = 0.4 : 0.4 : 0.2 \tag{2.7}$$

which is used as the relative probability of producing the B_u, B_d, and B_s mesons.

2.2.3 *b* Flavored Hadron Decay to χ_c

The *b*-hadrons can decay into charmonia by diagrams such as Figure 2.6. Branching ratios for some of these decays have been measured, and are summarized in Table 2.1 [4, 26]. Since the branching ratio for the decay $\chi_{c1} \to J/\psi\gamma$ is $(27.3 \pm 1.6)\%$ [4], the branching ratio for the decay chain $B \to \chi_{c1}X \to J/\psi\gamma X$ is $(0.17 \pm 0.06)\%$. The amount of the total branching

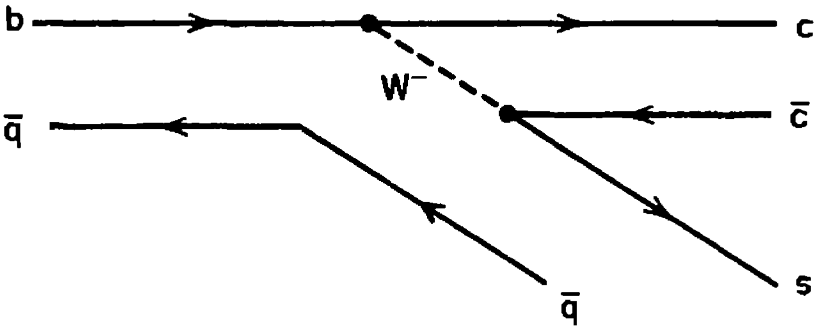

Figure 2.6: A B-meson decaying into charmonia

fraction to J/ψ due to decays through χ_{c1} is then

$$r_\chi = \frac{Br(B \to \chi_{c1}X \to J/\psi\gamma X)}{Br(B \to J/\psi X)} = 0.15 \pm 0.05. \tag{2.8}$$

This result is used in Chapter 9 to relate the measured χ_c and J/ψ cross sections to the direct and B-decay charmonia cross sections.

2.3 Inclusive Charmonia Production

An understanding of the total charmonia cross section can only come from understanding each mechanism for charmonia production. Measurements of the inclusive χ_c cross section, presented in this thesis, along with measurements of the inclusive J/ψ cross section, yield information on each of the major modes of charmonium production. This is done in detail in Section 9.2.

Chapter 3

The Experimental Environment

The Collider Detector at Fermilab (CDF) was a general purpose particle detector located at the B0 interaction region in the Tevatron, at Fermi National Accelerator Laboratory. During the time the data was taken for this analysis, the Tevatron was the highest energy accelerator in the world, providing proton-antiproton collisions at a center of mass energy of 1.8 TeV. Such high energy collisions have provided insight into many physical processes.

3.1 The Tevatron

The Tevatron was a superconducting synchotron built for the purpose of colliding protons against antiprotons at high energy to probe subatomic behavior. Superconducting magnets produced magnetic fields which curved the charged particles in a four mile circle through a vacuum tube in an underground tunnel at Fermilab. The Tevatron layout is shown in Figure 3.1, including the supporting lines. Fixed target lines are not shown.

The process of colliding protons and antiprotons starts with hydrogen gas, which is molecules of H_2, or two H atoms, each with a proton and electron. The gas was ionized to H^- to allow acceleration by electromagnetic fields. The H^- ions were accelerated in a Cockroft-Walton accelerator to an energy of 750 keV. They were then injected into a linear accelerator (linac), which was 150 meters long, and accelerated to 200 MeV. At this point the H^- ions were focused onto a carbon foil, which stripped off the two electrons, leaving only the proton. The protons next entered the Booster ring and were accelerated to 8 GeV. Two procedures utilized 8 GeV protons in the Booster: antiproton production and proton injection into the main ring for collisions. These are discussed below.

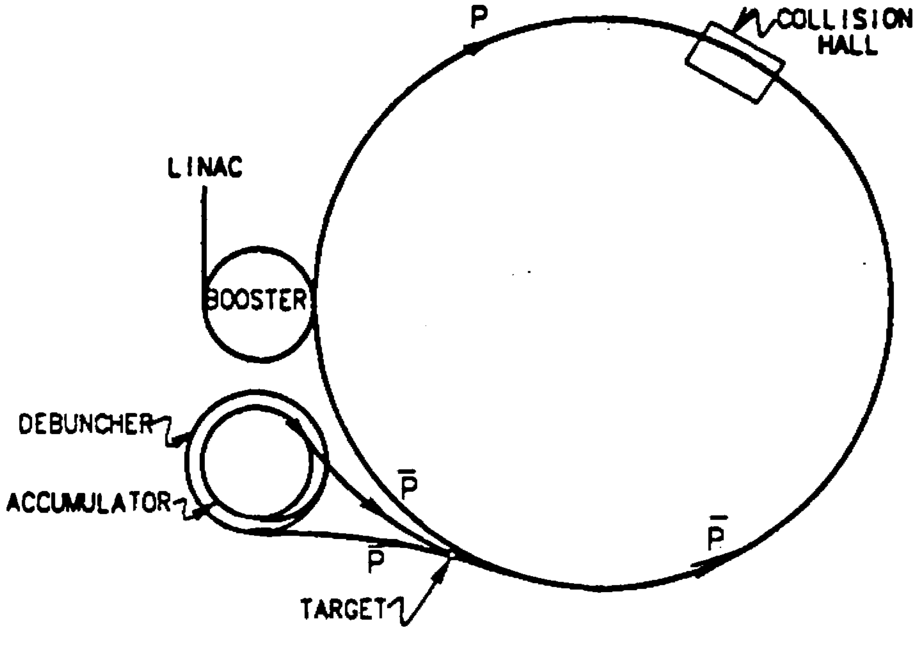

Figure 3.1: Plan of the Tevatron and support lines

The procedure for making antiprotons continued by taking the 8 GeV protons in the Booster and injecting them into the Main Ring, where they were accelerated to an energy of 120 GeV. The Main Ring had the same circumference as the Tevatron, and was positioned above it in the tunnel. The protons were then steered onto a copper target. A large number of different particles were produced in the resulting collision, some of which were antiprotons. Those antiprotons with an energy near 8 GeV were collected, sent to the Debuncher, and cooled. The antiprotons were then stacked in the antiproton Accumulator ring, until about 27×10^{10} were stored.

To prepare for colliding operation, the cycle was as follows. Protons were injected from the Booster into the Main Ring, and accelerated to the energy of 150 GeV. In the main ring, the protons were forced into one bunch consisting of about 7×10^{10} protons. This proton bunch was injected into the Tevatron, circulating clockwise and waiting for the antiprotons. During the 1988-89 run, the Tevatron ran in six bunch mode, so this injection procedure was repeated six times, resulting in six bunches around the ring.

Antiprotons from the Accumulator were than directed to the Main Ring, and, like the protons, were accelerated to an energy of 150 GeV. Since opposite charges curve in opposite directions in a magnetic field, the antiprotons were circulated counterclockwise, the opposite direction to that of the protons. At last the antiprotons were injected into the Tevatron to join the protons. Six bunches of antiprotons were injected, spaced about the ring.

At this point, diffuse bunches of protons and antiprotons were counter-rotating in the Tevatron at 150 GeV. The magnetic fields of the Tevatron magnets were increased as the particles were accelerated to the final beam energy of 900 GeV. The density of the beams was increased by a series of quadrupole focusing magnets, squeezing the particles together. This focusing constricted the beam spot size to less than 100 μm in diameter, ensuring an almost 100 % probability of interaction for each bunch crossing.

Bunches crossed at the B0 interaction point once every 3.5 μs. The counter-rotating beams could be sustained for over 20 hours until the luminosity would drop off, and a new store was prepared with the same cycle of events.

3.2 CDF

The Collider Detector at Fermilab (CDF) has been described elsewhere in great detail [28]. It was designed to measure the energy, momenta, and, where possible, the identity of particles produced in the $\bar{p}p$ collisions in the Tevatron. Its basic components included a magnetic spectrometer surrounded with electromagnetic and hadronic calorimeters. Schematics of the CDF experiment are shown in Figure 3.2 and Figure 3.3, and a photograph is shown in Figure 3.4.

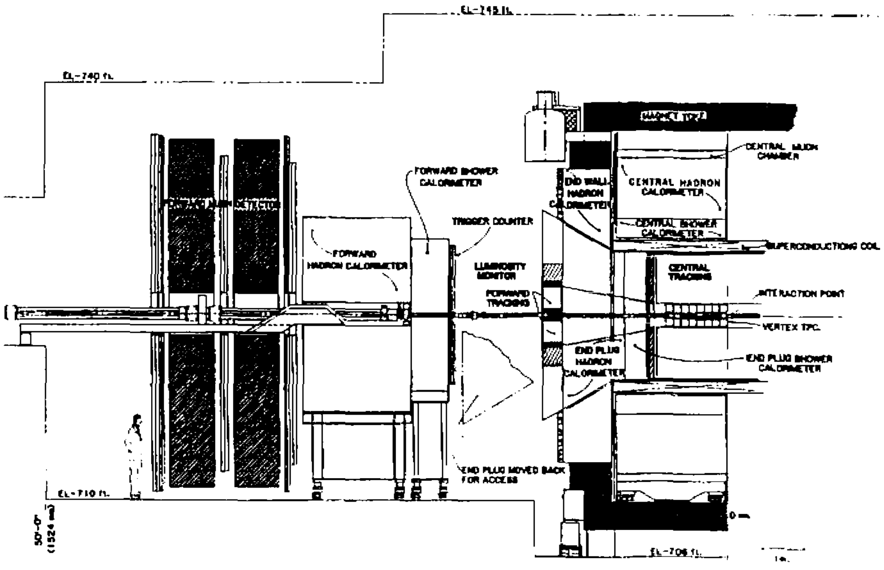

Figure 3.2: A schematic of the CDF layout

The CDF detector was roughly cylindrically symmetric. This utilized the natural symmetry of the beam line, where the protons and antiprotons came together and collided. The center of the detector was the origin of the CDF coordinate system and was positioned at the nominal collision point of the Tevatron, named B0. The z axis was defined as the proton direction, which is clockwise around the ring, or from the center of the detector pointing

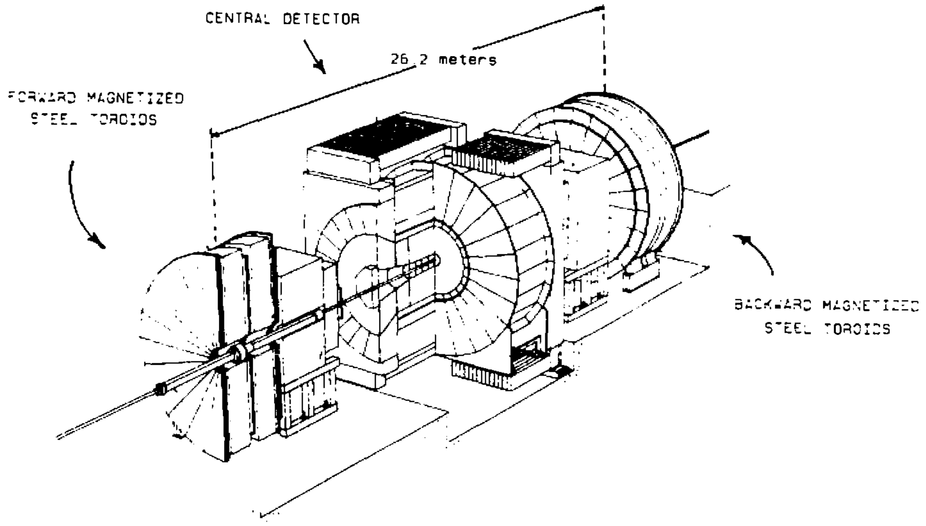

Figure 3.3: An isometric schematic of the CDF layout

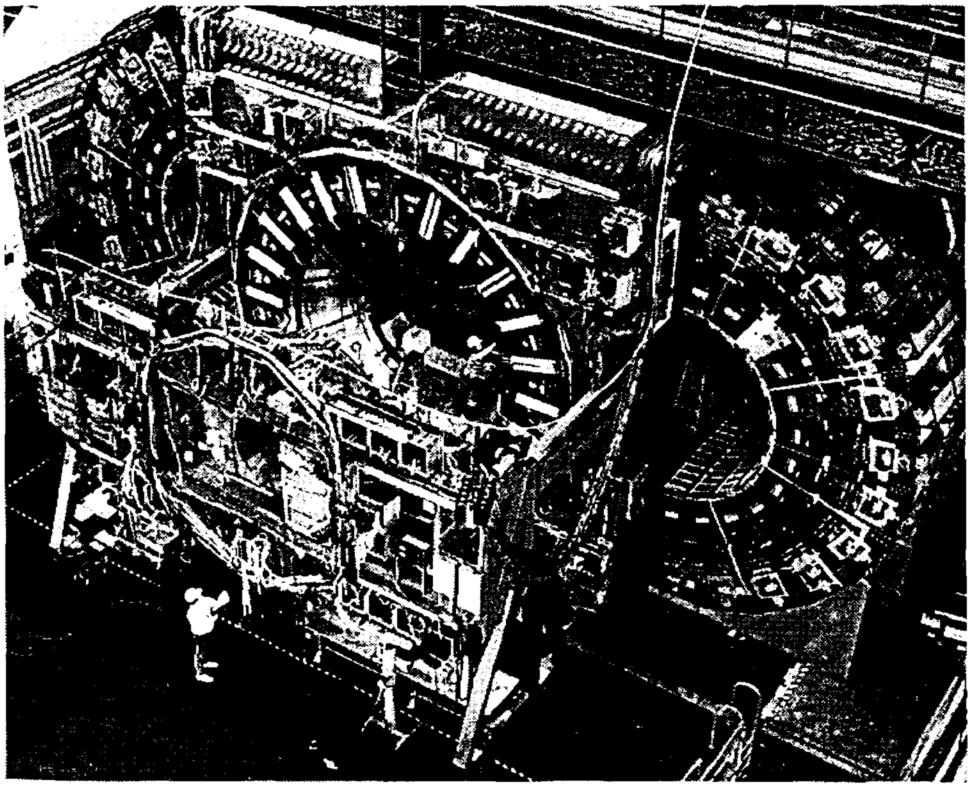

Figure 3.4: A picture of the detector

east. The x axis lay on the ring plane, and pointed out. The y axis pointed up, perpendicular to the ring plane. The angle about the z axis, ϕ, was 0 on the positive x axis. The polar angle, θ, was 0 on the positive z axis. The pseudorapidity, η, was defined by $\eta = -\ln \tan \frac{\theta}{2}$. The 'central region' was the term given to the region $-1 < \eta < 1$ or about $40° < \theta < 140°$. The detector in the central region included tracking, calorimeters, and muon identification. The forward region included calorimeters and muon toroids.

The beampipe was a low mass vacuum chamber of 500 micron thick beryllium with an outer radius of 5.08 cm. It is part of the vacuum system of the Tevatron, and is along the beam axis through the center of the detector. The pressure maintained in the beampipe was less than $\simeq 10^{-8}$ torr absolute, so the beam-gas interaction rate was very low at reasonable luminosities. The low mass requirement was to minimize multiple Coulomb scattering before particles entered the detector and to reduce charged particles which resulted from photons converting to e^+e^- pairs.

3.3 VTPC

Directly outside the beampipe, a system of eight Vertex Time Projection Chambers (VTPC) provided a measurement of θ of charged tracks to better than 1° for angles greater than 3.5° from the beamline. These eight chambers were end to end surrounding the beampipe. The active region of the VTPC extended from 6.8 to 21 cm from the beamline, and extended 1.4 m on either side of $z = 0$ (see Figure 3.5).

The segmentation of the VTPC balanced the need to cover the long interaction region with the need to have the maximum drift time less than the 3.5 μs beam crossing time. Each of the 8 chambers had a central high voltage grid separating it into two 15.25 cm long drift regions. Thus when the drift velocity in the gas was 46 μm/ns (the value of drift

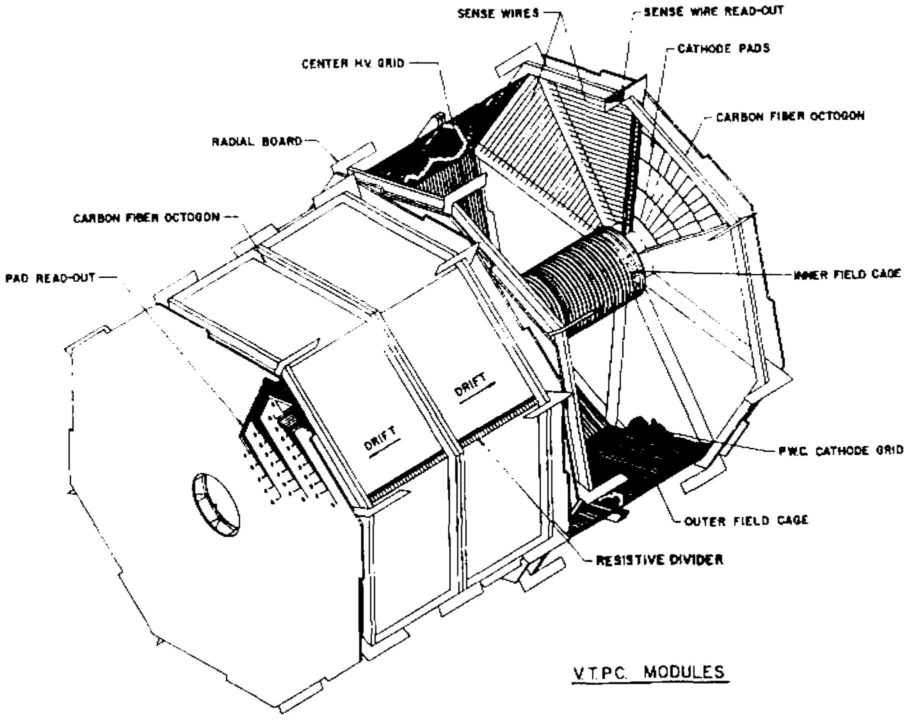

Figure 3.5: A schematic of the vertex time projection chamber

velocity in argon(50%)-ethane(50%) at atmospheric pressure and electric field strength of 320 V/cm) the maximum drift time was 95% of the available time between beam crossings. The chambers were placed end to end along the beamline, each 35.3 cm farther in z, resulting in 4.9 cm between the chambers which was not active space.

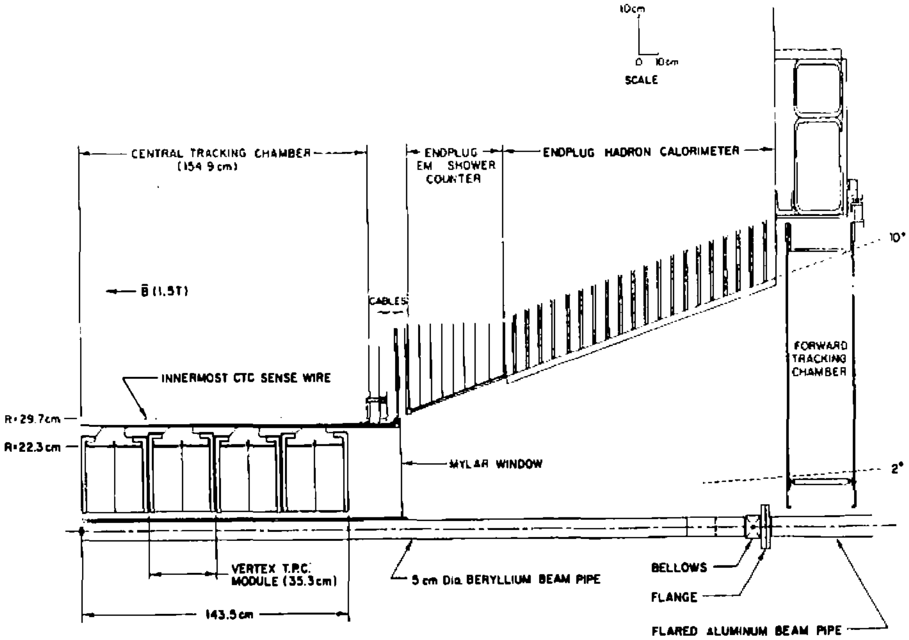

Figure 3.6: A schematic of the vertex time projection chamber

Each chamber was constructed in an octagon around the beamline (See Figure 3.6). Charged particles ionized the argon-ethane, and the charge was swept toward the sense wires. Timing information from each wire allowed reconstruction of the distance from the wire to the particle's ionization track. For 90° tracks, the resolution per wire was 420 μm, rising to 1100 μm at 11°. Since the drift direction was parallel to the magnetic field, Lorentz forces kept the drifting electrons moving along the magnetic field lines, reducing diffusion and thus improving the resolution.

The interaction vertex of the $p\bar{p}$ collisions was reconstructed with an rms resolution of 1

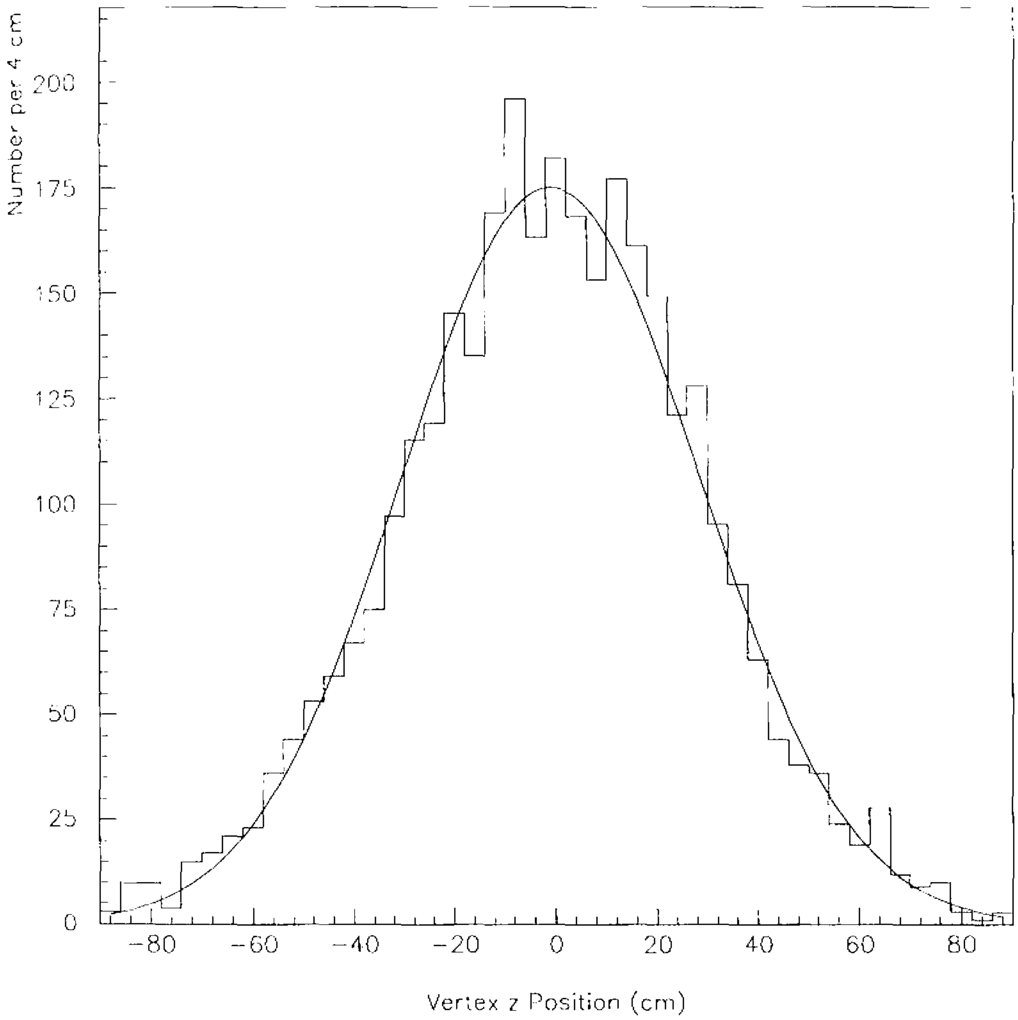

Figure 3.7: The z vertex distribution for J/ψ candidate events

mm in the z direction. This vertex was used as the origin in computing the transverse energy ($E_T = E\sin\theta$) deposited in each calorimeter cell. The distribution in z of reconstructed vertices in events with two muons is shown in Figure 3.7 and is well described as a Gaussian of mean -1 cm and width 30 cm. This spread of vertices reflects the convolution of the proton and antiproton bunches in the collider. Thus the vertices were within the 2.8 m long active region of the VTPC.

3.4 CTC

The Central Tracking Chamber (CTC) measured the trajectories of charged particles that traversed the active CTC volume. These trajectories were important for three reasons. The first was the precise determination of particle momentum. The second was the identification of leptons. The third was identification of secondary vertices from long lived particle decays.

Momentum determination required knowledge of the track parameters and the magnetic field. In the presence of the magnetic field, charged particles travelled a helical path. The radius, R, of the helix is related to the momentum of the particle, p, by the relation

$$|p|\cos\lambda = cq|B|R \tag{3.1}$$

where λ is the pitch angle of the helix, q the charge of the particle, B is the magnetic field, and c is the speed of light. Since the magnetic field was aligned with the beamline, $|p|\cos\lambda$ was just p_T, the transverse momentum of the particle.

Lepton identification relied on matching the CTC track with tracks or clusters in other parts of the detector. Electrons were identified by matching tracks to energy deposition in the electromagnetic calorimeters. Muons were identified by matching CTC tracks to tracks in the muon chambers. These detectors will be discussed in detail in a later section.

mm in the z direction. This vertex was used as the origin in computing the transverse energy ($E_T = E\sin\theta$) deposited in each calorimeter cell. The distribution in z of reconstructed vertices in events with two muons is shown in Figure 3.7 and is well described as a Gaussian of mean -1 cm and width 30 cm. This spread of vertices reflects the convolution of the proton and antiproton bunches in the collider. Thus the vertices were within the 2.8 m long active region of the VTPC.

3.4 CTC

The Central Tracking Chamber (CTC) measured the trajectories of charged particles that traversed the active CTC volume. These trajectories were important for three reasons. The first was the precise determination of particle momentum. The second was the identification of leptons. The third was identification of secondary vertices from long lived particle decays.

Momentum determination required knowledge of the track parameters and the magnetic field. In the presence of the magnetic field, charged particles travelled a helical path. The radius, R, of the helix is related to the momentum of the particle, p, by the relation

$$|p|\cos\lambda = cq|B|R \tag{3.1}$$

where λ is the pitch angle of the helix, q the charge of the particle, B is the magnetic field, and c is the speed of light. Since the magnetic field was aligned with the beamline, $|p|\cos\lambda$ was just p_T, the transverse momentum of the particle.

Lepton identification relied on matching the CTC track with tracks or clusters in other parts of the detector. Electrons were identified by matching tracks to energy deposition in the electromagnetic calorimeters. Muons were identified by matching CTC tracks to tracks in the muon chambers. These detectors will be discussed in detail in a later section.

The CTC was a cylindrical drift chamber, with the cylindrical axis along the beamline (Figure 3.8). It was located outside the VTPC, with an active region beginning 30 cm from the beamline and extending to 130 cm from the beamline. The chamber consisted of 84 layers of sense wires, arranged in 9 superlayers (see Figure 3.9). The sense wires were instrumented to measure the time of a wire hit in relation to a global event time zero. Stereo information was obtained by interleaving superlayers with sense wires parallel to the beam axis (axial superlayers) and superlayers with sense wires canted at $\pm 3^\circ$ with respect to the beam axis (stereo superlayers). Thus three dimensional tracking was achieved.

Superlayers were arranged in drift cells containing potential wires and field shaping wires to maintain the electric field needed for drift chamber operation as well as sense wires to collect the data (see Figure 3.10). Charges from ionization tracks travelled paths determined by the electric and magnetic fields. The field wires provided a drift field of approximately 1350 V/cm. Since the magnetic field (of magnitude 1.4 T) was parallel to the beamline, the drift velocity had a component in the direction of $\mathbf{E} \times \mathbf{B}$ in addition to a component parallel to $\mathbf{E}$. The net drift velocity formed an angle relative to the $\mathbf{E}$ field given by

$$\tan\beta = \frac{v|\mathbf{E}|}{k|\mathbf{B}|} \tag{3.2}$$

where v was the drift velocity with no magnetic field and k was a gas-dependent parameter (about 0.7 for argon-ethane). The angle β was about 45° during operation. The drift trajectories in a drift cell are shown in Figure 3.11.

Timing of the charge reaching the sense wires gave the track coordinates. Each sense wire was connected to a multiple hit TDC. Timing information combined with drift velocity gave distance along the drift trajectory to the ionization track. Figure 3.12 shows the residual distribution (measured ionization track point - fitted track position) for 3 dimensional fitted tracks with momentum > 800 MeV/c. This plot shows the hit resolution was 220 μm. The

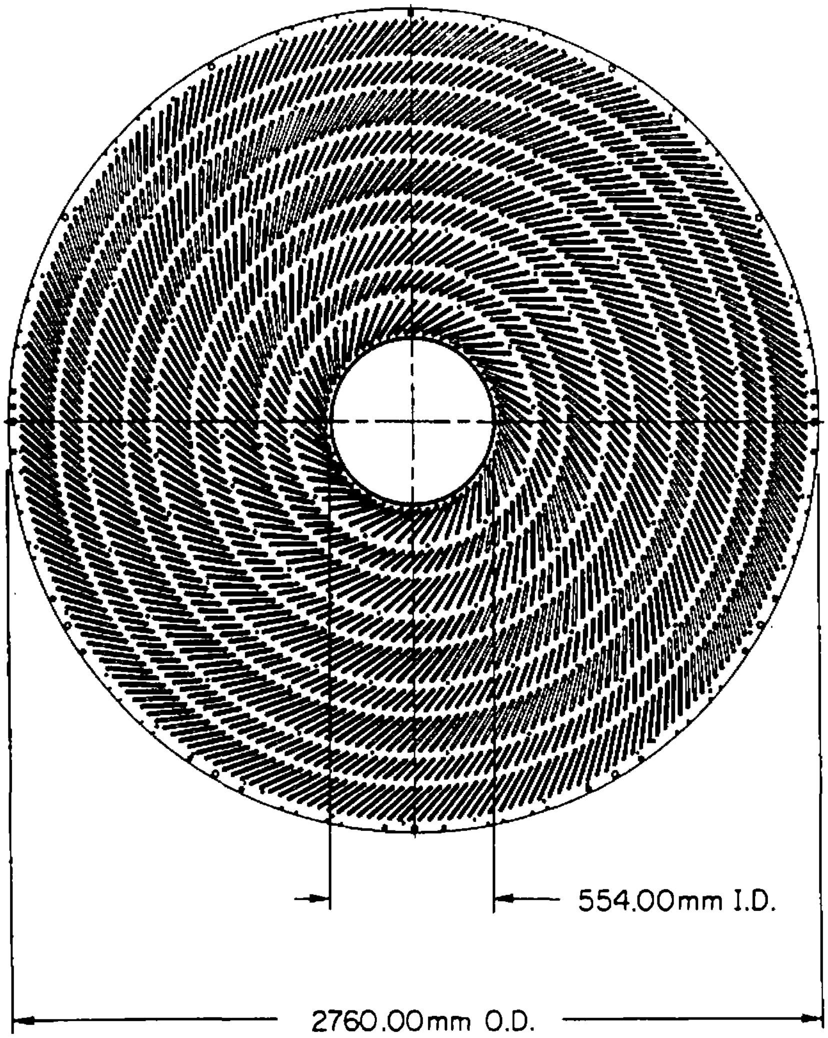

Figure 3.8: A schematic of the Central Tracking Chamber

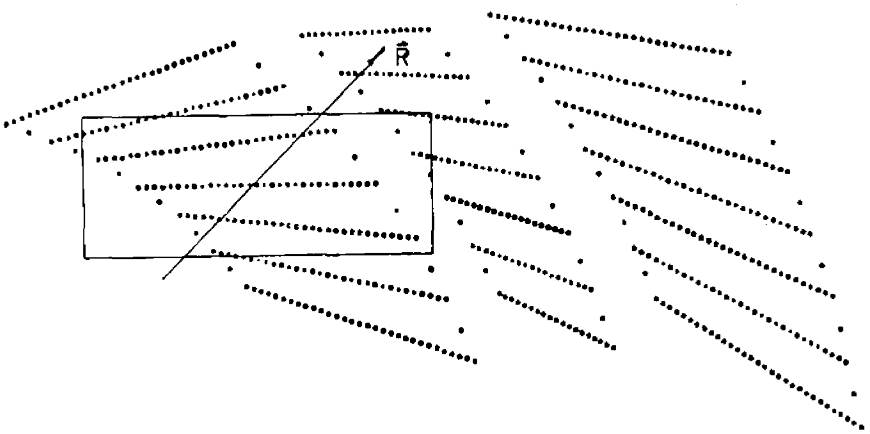

Figure 3.9: A schematic of the CTC wires

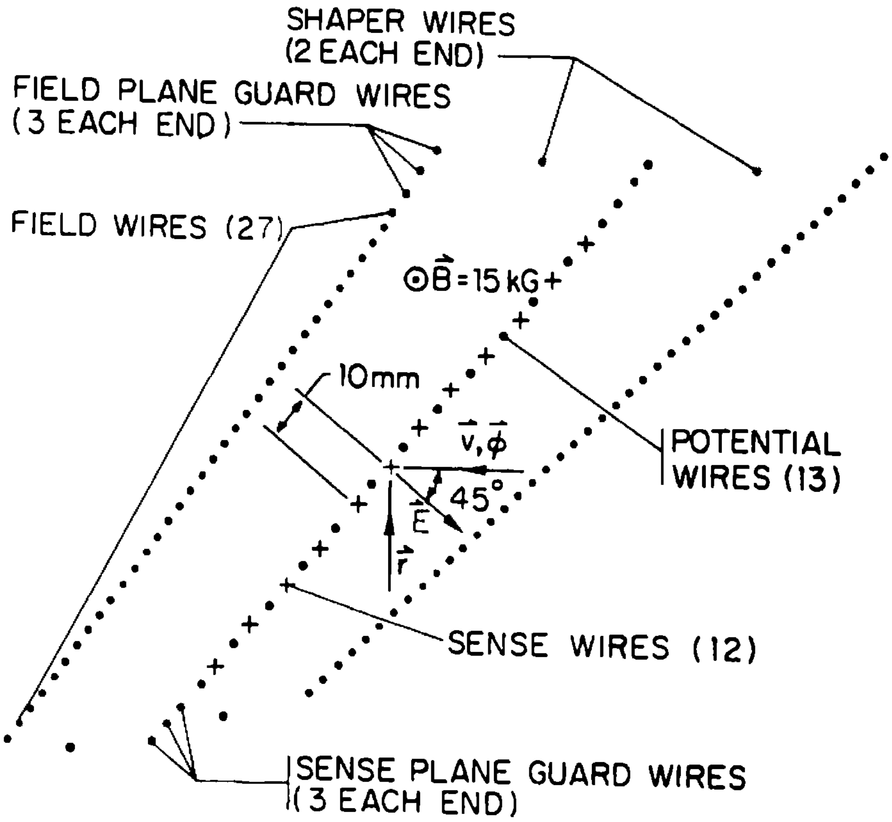

Figure 3.10: A CTC drift cell

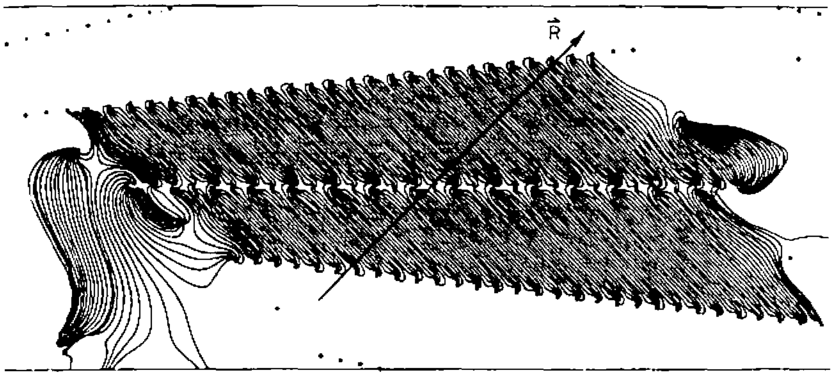

Figure 3.11: The CTC wires in a drift cell and the drift trajectories

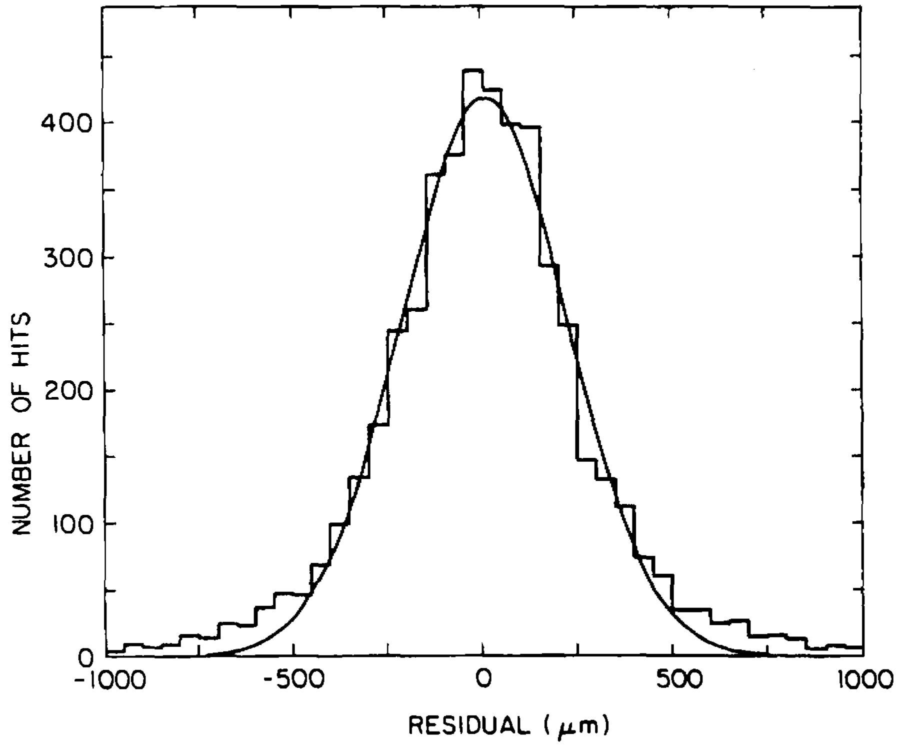

Figure 3.12: Wire to track residual distribution

resolution of a stereo wire in the longitudinal (z) coordinate would be $(220\ \mu\text{m})/(\sin 3^\circ) =$ 4.2 mm.

Since multiple coulomb scattering and energy loss in matter before the particles have been measured can affect the resolution, it was important to minimize the amount of material in front of the tracking chambers. In addition, the great number of photons produced per event would interact with matter and pair produce e^+e^-, adding tracks not produced in the initial event. For these reasons, the detector was constructed with low mass materials, to minimize the number of radiation lengths traversed by particles before they encountered the CTC active volume. About 3% of a radiation length was traversed by tracks perpendicular to the beam line before reaching the CTC active volume. About 0.5% of a radiation length was from the beampipe, while the VTPC contributed 1.5% of a radiation length. The remainder was due to the CTC inner wall. At angles closer to the beam pipe, more material was traversed, scaling as $1/\sin(\theta)$ in the central region until the end of the CTC was reached.

3.5 Solenoid

The magnetic field was produced by a 3 m diameter 5 m long superconducting solenoid coil [29] (visible in Figure 3.2). The coil consisted of 1164 turns of NbTi/Cu superconducting metal alloy, stabilized with aluminum. The overall thickness of the solenoid, support and cooling material was 0.85 radiation lengths.

The solenoid provided a uniform 1.46 T magnetic field oriented along the beam direction. The field was produced by a current of 4659 A flowing in the superconducting material. A steel flux return yoke encased the entire detector, forming a large box 9.4 m high by 7.6 m wide by 7.3 m long. This yoke, in addition to its function as a magnetic flux return path, supported the solenoid and end plug calorimeters.

3.6 Calorimeters

In addition to the magnetic spectrometry provided by the tracking systems, CDF included electromagnetic and hadronic calorimeters. The goals of the CDF calorimeters were complementary to the tracking. The calorimeters, constructed in a projective tower geometry, measured the energy of both charged and neutral particles in a tower, whereas the tracking measured momenta of individual charged particles. Projective tower geometry means that the calorimeter was separated into $\eta - \phi$ sections or "towers" which pointed back radially to the interaction region at $z = 0$. The calorimeters were helpful in particle identification, most especially electrons and photons, and gave information to help identify muons and select hadronic jets. The calorimeters were segmented longitudinally into electromagnetic and hadronic sections.

3.6.1 Electromagnetic Calorimeters

The electromagnetic calorimeters measured the energy of incident electrons, positrons, and photons by sampling the energy deposited in an electromagnetic cascade. They also aided in the identification of $e^{\pm}$ and γ by matching clusters of energy with tracks from the CTC.

The Central Electromagnetic Calorimeter (CEM) surrounded the solenoid, covering the region $|\eta| < 1$. The CEM consisted of sheets of lead radiator interleaved with sheets of scintillating polystyrene (Figure 3.13). Particles interacted with the lead by bremsstrahlung and pair production to produce an $e^{\pm}$ and γ cascade. The charged particles then passed through the scintillator, which produced light when traversed by charged particles. This light was transmitted by waveshifting plastic to light guides leading to phototubes which measured the intensity.

Since most particles of interest would originate near the center of the detector, the

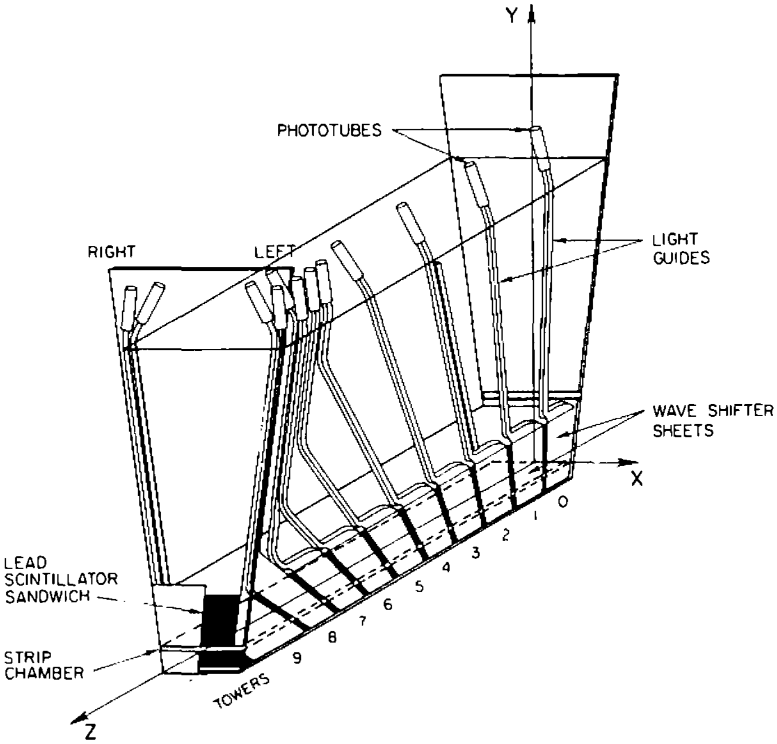

Figure 3.13: A schematic of the CEM

calorimeters were arranged in a projective tower geometry. These towers surrounded the solenoid, and were ganged into wedges. Figure 3.13 shows one wedge. There were a total of 48 wedges, arrayed in two concentric cylinders of 24 wedges each. These cylinders were end to end on the z axis, and centered at the CDF origin. Each wedge was comprised of 10 projective towers pointing to the collision point. The segmentation of each tower was $\Delta\eta \times \Delta\phi = .09 \times 15^\circ$. The towers covered from η=0 to $\eta = \pm\ 1.1$, the sign being determined by which cylinder the wedge was in.

The construction of the CEM is shown in Figure 3.14. There were 31 lead layers, each 0.32 cm thick. After each lead layer, there was 0.5 cm of SCSN-38 polystyrene scintillator [30]. All layers of Pb and scintillator added up to the 18 radiation length thickness of the CEM.

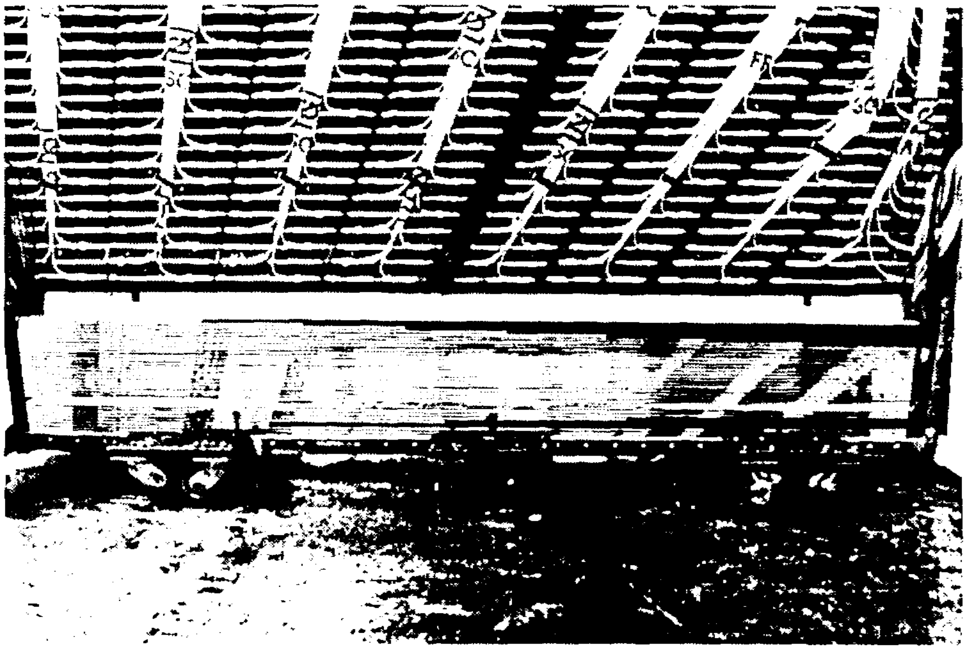

Figure 3.14: The construction of the lead scintillator sandwich is shown

Since the CEM was a sampling electromagnetic calorimeter, the energy resolution was dominated by the statistical uncertainty in the number of cascade particles passing through the scintillator. The number of cascade particles was proportional to the total energy, so the energy resolution should scale as $\sqrt{E}$. For the CEM,

$$\frac{\sigma_E}{E} = \frac{13.5\%}{\sqrt{E}} \oplus 1.7\% \tag{3.3}$$

where E is the energy in GeV, and the second term is due to cell to cell variations in the energy calibration and is added in quadrature to the first term.

The Central Electromagnetic Calorimeter was a hybrid calorimeter in that it combined the excellent energy resolution of the sampling scintillator sandwich with the fine segmentation of a gas proportional chamber layer. This gas proportional chamber was designed to measure the lateral shower profile and give a precision determination of the shower position. An example of the use of the lateral shower profile was in separation of γ showers from those arising from high energy $\pi^0 \rightarrow \gamma\gamma$, in which the two photons fell in the same tower but gave an extended lateral profile as will be discussed in chapter 5. The position information was useful for tower geometry energy corrections, and for making mass combinations with photons as was done in the χ_c analysis.

The gas chamber was a proportional strip chamber. Called the Central Electromagnetic Strip chamber (CES), it was located six radiation lengths into the CEM, near shower maximum for energetic electrons expected from $W^{\pm}$ or Z^0 decay. The CES was 0.75 inches thick, and used strips and wires to resolve position in the z and r-ϕ directions respectively. The anode wires and the cathode pads were arranged orthogonally, with the wires parallel to the z axis. Thus the wires delivered $r-\phi$ information, and the pads z information. The position resolution for W electrons was $\sigma = 2$ mm in the $r-\phi$ direction, and $\sigma = 5$ mm in the z direction.

Due to the demands of the wedge construction, the active area of the CEM and CES did not extend over the whole central region. A narrow dead space between wedges was used for wave shifters and light guides as well as support structures. In addition, energy response near the detector edges was non-uniform and much smaller, mainly due to shower leakage into dead regions [31, 32]. The edges of the detectors were not used in this analysis as outlined in chapter 8.

3.6.2 Hadronic Calorimeters

The Central Hadronic Calorimeter (CHA) was also a sampling calorimeter. It operated much like the electromagnetic calorimeter, except the incident hadron lost energy by a nuclear cascade. This resulted in showers extending through more material than electromagnetic cascades, and allowed the hadronic calorimeters to be placed behind the CEM. The hadronic calorimeter consisted of steel radiator sheets and acrylic scintillator with photomultiplier readout.

The difference in absorber materials in the CEM and CHA followed from the purpose of each calorimeter. For electromagnetic/hadronic separation, an electromagnetic absorber needed to have a large cross section for electromagnetic interactions, with as small as possible cross section for hadronic interactions. Table 3.1 shows the electromagnetic radiation length and the nuclear interaction length for a few commonly used absorber materials [4]. It is clear that many radiation lengths of lead is thin, while having relatively few interaction lengths. Lead is also cheaper and easier to use than uranium. In hadronic calorimeters, most of the electrons or photons would already have cascaded, so only the nuclear interaction length was important. Many nuclear interaction lengths of iron is cheaper and not as heavy as some of the other materials, so is useful for hadronic calorimeters. For these reasons, lead was used in the CEM while steel was used in the CHA.

Since the CHA was positioned just outside the CEM, the wedge structure was built

	X_0	λ_I
Pb	0.56 cm	17.09 cm
Fe	1.76 cm	16.76 cm
U	0.32 cm	10.50 cm
Cu	1.43 cm	15.06 cm
Si	9.36 cm	45.49 cm

Table 3.1: Electromagnetic radiation lengths (X_0) and nuclear interaction lengths (λ_I) for various materials.

together with both calorimeters (see Figure 3.15). The CHA was designed with the same wedge and projective tower geometry as the CEM, with $\Delta\eta \times \Delta\phi = .09 \times 15^\circ$. There were 32 iron steel layers each 2.5 cm thick, each followed by 1 cm of acrylic scintillator to comprise the entire CHA which was 5 interaction lengths thick. Fewer particles were produced in the CHA from nuclear cascades than produced in the CEM in electromagnetic cascades, so the energy resolution due to statistical fluctuations was larger. The energy resolution for incident pions was measured in a test beam to be

$$\frac{\sigma_E}{E} = \frac{70\%}{\sqrt{E}} \oplus 3\%. \tag{3.4}$$

3.7 Muon Chambers

The two purposes of the CDF muon systems were to identify muons and trigger on them. The muon chambers took advantage of the fact that muons do not produce cascades, and thus were the only charged particles likely to penetrate the dense material of the calorime-

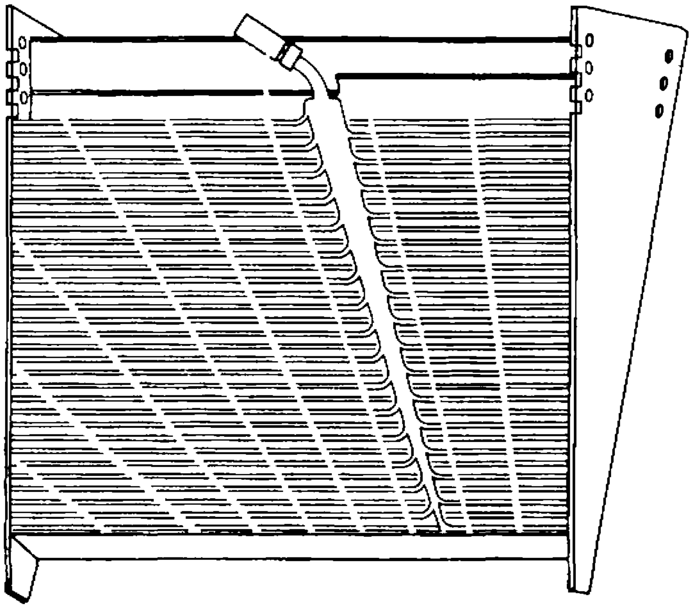

Figure 3.15: A schematic of the CHA

ters. The development of an electromagnetic cascade follows the emission of an energetic photon due to the rapid acceleration of an incident charged particle under the influence of the nuclear Coulomb field. The large mass of the muon compared to that of the electron greatly reduces the probability of such accelerations. Hence, muons do not produce electromagnetic cascades. Hadronic cascades, on the other hand, result from hadronic interactions between the incident particle and the nuclei of the material. Since leptons do not interact hadronically, they do not produce hadronic cascades. Muons then pass through the calorimeters only mitigated by normal charged particle energy loss and multiple coulomb scattering.

In the central region the muon detection was performed with the Central Muon Detectors (CMU). The CMU detectors were drift chambers for the detection of charged tracks. There were 48 sets of chambers, one located behind each CHA wedge. The set of chambers, or CMU wedge, subtended 12.6° in ϕ. This left a gap of 2.4° between each wedge.

Each CMU wedge consisted of three modules in ϕ (See Figure 3.16). Each module contained 16 cells arrayed in four layers (see Figure 3.17). A CMU cell contained one sense wire in a drift chamber operated in limited streamer mode. Four sense wires, one for each layer, made up a muon tower (See Figure 3.18). Two of the four sense wires, from alternating layers, lay on a radial line which passed through the nominal interaction point. The remaining two wires lay on a radial line which was offset from the first by 2 mm at the midpoint of the chamber. Differences in timing resolved which side in ϕ a track passed.

Charge division was used to obtain the position of a track along the sense wire. Each sense wire was connected at the end nearest $z = 0$ to a sense wire in the same layer which was separated from the first by an intervening drift cell. At the end farthest from $z = 0$, each wire was attached to a blocking capacitor which was in turn connected to digitizer cards. The cards digitized both timing information for $r - \phi$ determination, and the magnitude of the pulse for z determination.

3.8 Luminosity Monitor

CDF was equipped with a series of low angle scintillators, called the Beam-Beam Counters (BBC's), which were used as a luminosity monitor. They provided a beam luminosity measurement independent of that obtained strictly from measurements of beam profile parameters. These planes of scintillator, with the geometry outlined in Figure 3.19, surrounded the beampipe on both sides of the detector. The BBC active region was $0.32^\circ < \theta < 4.47^\circ$. The time information from the BBC's had a resolution of less than 200 ps, and thus gave a measurement of the time of the interaction.

3.9 Data Collection

The data used in this analysis were collected over a 12-month period in 1988 and 1989. The peak machine luminosity grew to over 2×10^{30} cm^{-2} s^{-1} by the end of the run. Although 4.7 pb^{-1} were taken for the run, only 2.6 pb^{-1} were taken utilizing the dimuon trigger described in the next chapter.

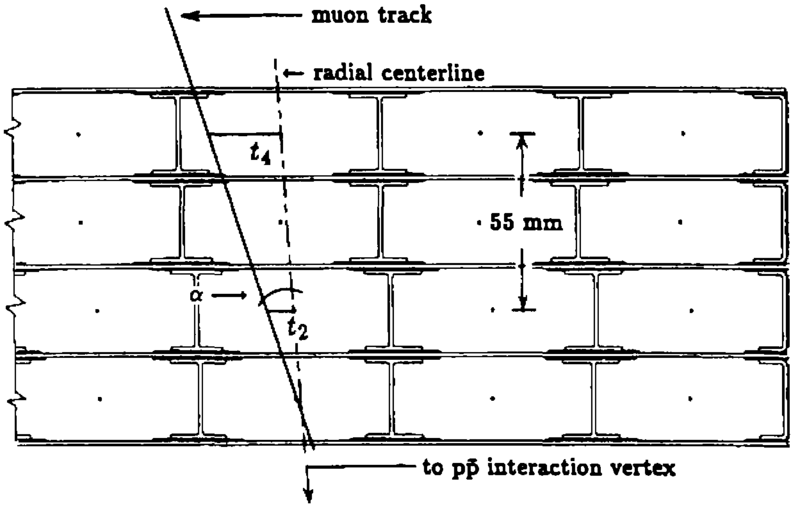

Figure 3.16: A schematic of a CMU wedge

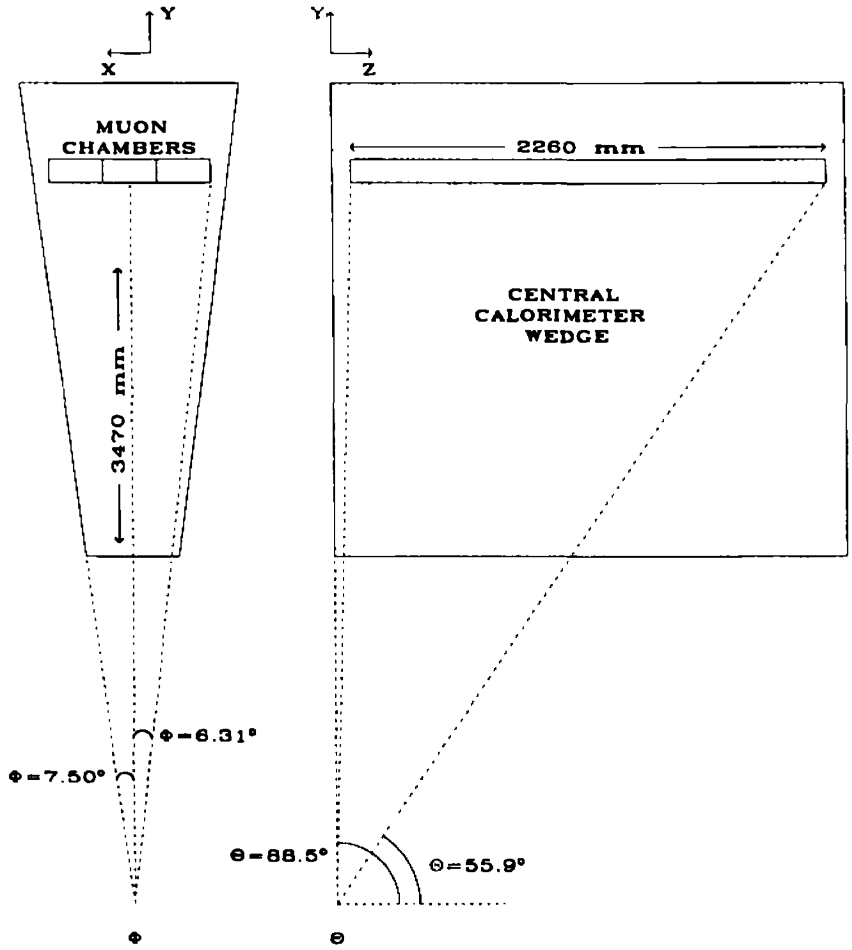

Figure 3.17: A schematic of a CMU wedge

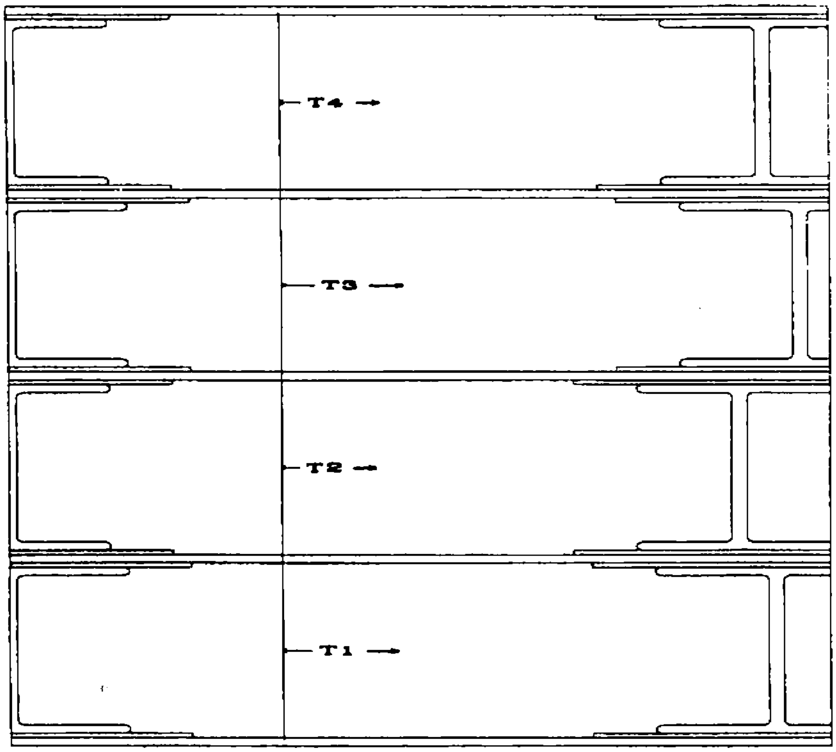

Figure 3.18: A schematic of a CMU tower

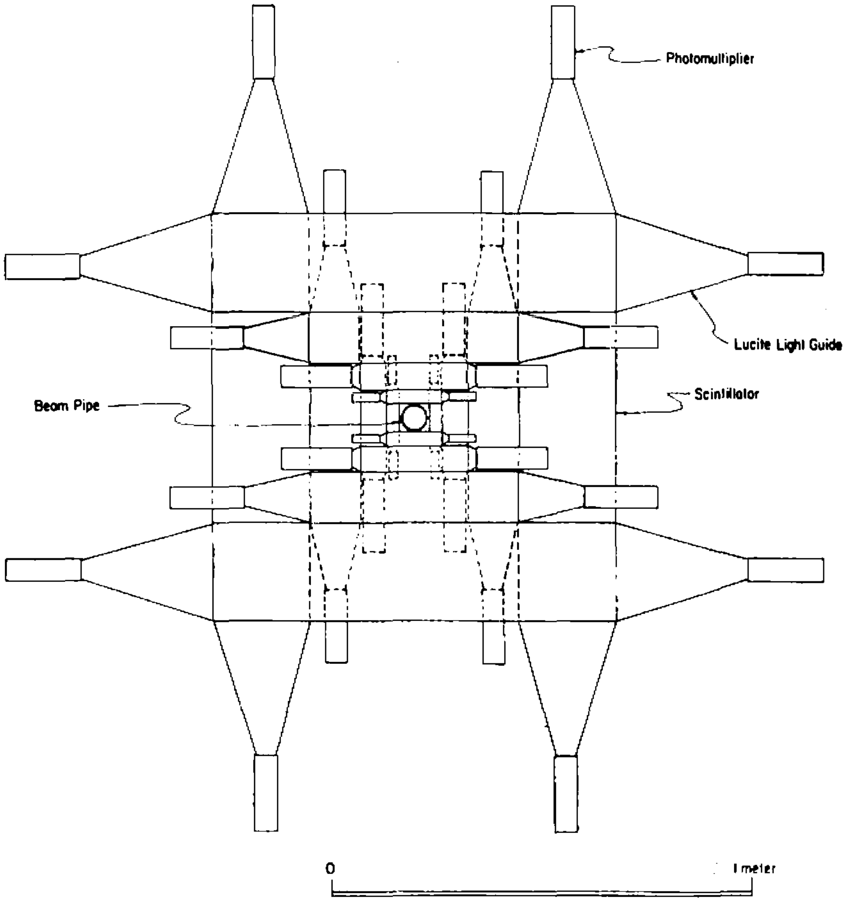

Figure 3.19: A schematic of the beam beam counters

Chapter 4

Triggering

In the hadron collider environment at the Tevatron, the collision rate was 10^5 times higher than the rate at which the detector could be read out. Because of this, a way of selecting the interesting events was required. To quantify more precisely the reduction needed, it should be noted that the inelastic cross section in $\bar{p}p$ collisions at Tevatron energies is about 40 millibarns, whereas the charmonium cross section for the region addressed in this analysis is measured in nanobarns. Since the instantaneous luminosity at CDF averaged about 1.6 $\mu b^{-1} s^{-1}$, the inelastic collision rate was about 70 kHz. The maximum rate for reading events out of the detector and writing them to tape was a few Hertz. Therefore, there was a great need to select or reject events in an intelligent manner. The method of making a quick decision on whether a given event is interesting is called triggering. The selection criteria for making this decision is called a trigger. A trigger is needed to do most kinds of physics at a hadron collider.

To accumulate a well defined sample of interesting physics events while rejecting other kinds of events, CDF employed a four level trigger system [33] to reduce the interaction rate to a rate that could be written to tape. Many sets of triggers with different selection criteria for many different topics were used. These topics ranged from top quark tagging and vector boson selection to jet analyses and charmonia production. The trigger specifically described here for the χ_c analysis was aimed at selecting the dimuon decay of the J/ψ. It should be kept in mind that the total trigger system at CDF had a much more general nature. Bearing that in mind, the trigger system and the dimuon trigger are described below.

The purpose of the multi-level structure of the trigger was to make trigger decisions while introducing as little unwanted bias as possible at the lower levels. Each level of the trigger needed to reduce the rate to a point where the next level could do a more complex analysis without incurring significant deadtime. Each successive level of the trigger used more information and took more time making the decision. The first three levels, denoted level 0, level 1, and level 2, were hardware triggers. They used analog signals representing a subset of the information available from a full detector readout. The highest level trigger, level 3, was performed on an ACP farm (a farm of 60 Motorola 68020 computer nodes, named for Advanced Computer Program [34]). The computers ran with Fortran algorithms, with the full detector data available. Due to the cleanliness of the dimuon signal, the level 3 trigger was not needed to select the data sample for this analysis.

The dimuon selection criteria for this analysis, for reasons which will become apparent shortly, was labelled the dimuon_central_3 trigger. This trigger was implemented during only a portion of the 1988-89 run, so it gathered data from an integrated luminosity of only 2.6 pb^{-1} and not the 4.7 pb^{-1} of the entire run.

The first level of trigger selection, the level 0 trigger, was designed to select inelastic events. It did this by requiring at least one beam-beam counter (BBC) hit in both the forward and backward counter arrays coincident within a 15 ns window centered on the beam crossing time. A crude ($\pm$ 4 cm) measurement of the vertex position was also obtained from the timing. Level 0 had 3.5 microseconds to decide whether to pass the event to the next trigger level before the next crossing. The small time the decision actually took ($\simeq$ 500 ns) resulted in no dead time. That is to say that no beam crossing was wasted while the level 0 trigger "made up its mind". The trigger decision was available in time to inhibit data taking during the next beam crossing, 3.5 μs later.

The level 1 decision was made within the 7 μs allowed by level 0, including the 3.5 μs level 0 decision time. If the event failed in level 1, the front end electronics were reset in time for the second crossing after the initial level 0 decision. The level 1 dimuon trigger made decisions based upon information from the muon trigger towers indicating that there was at least one central muon candidate in the event.

The level 1 muon trigger used hits from the muon TDC's to identify high p_T track "stubs" in the muon chambers. The trigger imposed a cut on the time difference $|t_4 - t_2|$ or $|t_3 - t_1|$ (See Figure 3.18) between two radially aligned wires in a muon tower, where t_i was the drift time to the ith wire in the muon tower [35]. This restricted the maximum allowed angle of a track with respect to an infinite-momentum track (straight in the magnetic field) emanating from the $p\bar{p}$ vertex and thus applied a cut on the p_T of the muon candidate.

Multiple scattering softens the trigger threshold in muon candidate p_T. This is due to the smearing of the angle with which the track passes through the muon chamber. The nominal angle for a muon travelling from the origin to the CMU is $\alpha_0 \simeq \frac{C_{\alpha_0}}{p_T}$, where C_{α_0} is a constant arising from the geometry and magnetic field. The angle, α_0, is smeared in a way which can be approximated by a Gaussian with a width as described in Chapter 8. If Δt is defined as the minimum of $|t_4 - t_2|$ or $|t_3 - t_1|$, for a muon it would nominally be related to the transverse momentum by $\Delta t_0 \simeq \frac{C_{\Delta t_0}}{p_T}$. Since the level 1 trigger imposed a maximum of 70 ns on Δt, the angle used in this trigger corresponded to a p_T threshold of 3 GeV/c. The sharpness of this cut is lost, however, due to the spread in Δt from multiple scattering.

The efficiency of the level 1 dimuon trigger was studied using a sample of cosmic ray muons [36]. The cosmic ray trigger required a triple coincidence of CDT hits with hits in the first two axial superlayers of the CTC, as well as one CFT track (defined below). All reconstructed CTC tracks from this sample were cosmic rays, taken to be muons. This yielded a muon sample independent of the CMU chamber information and muon triggers. The number of muons which went through the CMU and triggered over the number which went through the CMU was the efficiency. Figure 4.1 shows the efficiency as a function of muon transverse momentum. The efficiency plateaus at a value of (91.8 ± 2.4) % for $p_T > 6$ GeV/c.

Since the cosmic ray study of the level 1 dimuon_central_3 trigger efficiency had low statistics below a transverse momentum of about 5 GeV/c, the efficiency was also studied using data obtained from non-muon triggers [37]. Any event which had a muon stub in the chambers matched with a CTC track was examined as a possible muon. These could have arisen from real muons, hadronic punchtrough or decays in flight. The real muons should be minimum ionizing in the calorimeters, while hadrons would deposit more energy. Energy deposition was examined to determine the number of each in every p_T region by fitting the energy deposition to the functional form expected from muons and hadrons. The number of real muons in both the entire sample and the events which also passed the trigger were found in this way. Figure 4.2 shows the efficiency as a function of μ p_T using both methods. This is parameterized by

$$\epsilon = \frac{A}{\sqrt{2\pi}\sigma_\alpha} \int_{-\alpha_c}^{\alpha_c} e^{\frac{-(\alpha-\alpha_0)^2}{2\sigma_\alpha^2}} d\alpha \tag{4.1}$$

where

$$\sigma_\alpha^2 = (\frac{0.131}{p_T})^2 \frac{0.27 + 0.73/\sin\theta}{1 - 1.43/p_T} + (0.0062)^2, \tag{4.2}$$

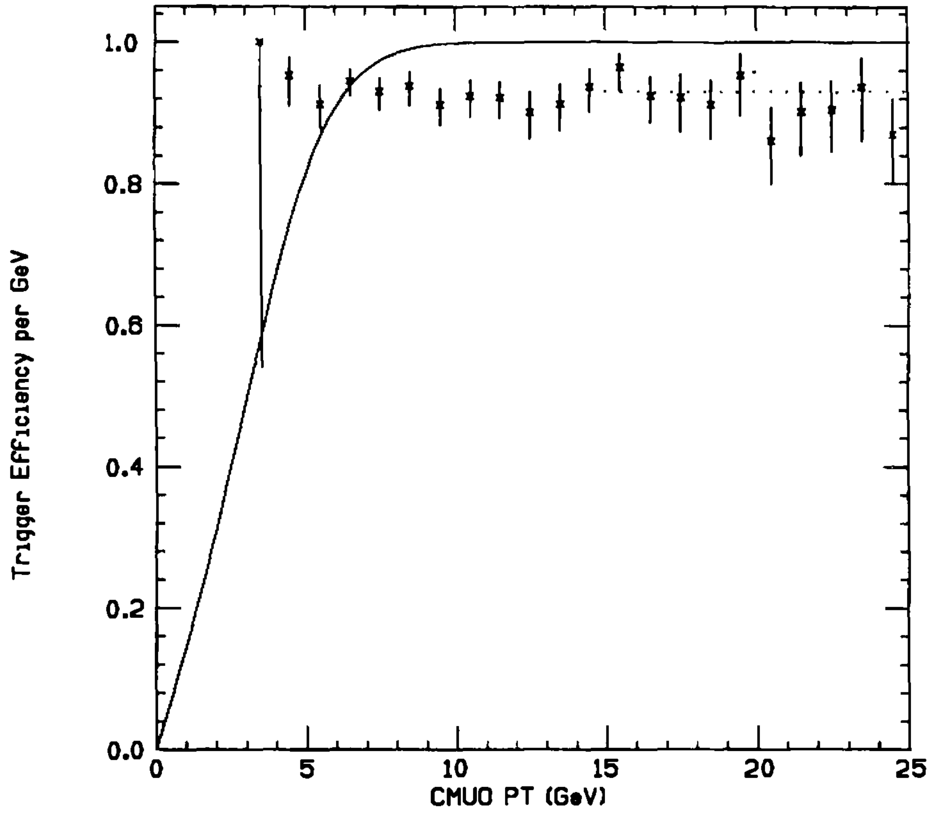

Figure 4.1: The level 1 trigger efficiency as measured with cosmic ray muons [36]. The solid line is a calculation of the expected shape of the trigger turn on due solely to multiple scattering in an otherwise perfect trigger. The dotted line shows the average efficiency measured from cosmic ray data for muon $p_T > 15$ GeV/c, where multiple scattering is of minimal effect to the trigger.

(Resulting from multiple scattering as outlined in Chapter 8)

$$\alpha_0 = \frac{0.126}{p_T}, \tag{4.3}$$

$A = 0.918 \pm 0.024$ and $\alpha_c = 0.086 \pm 0.005$.

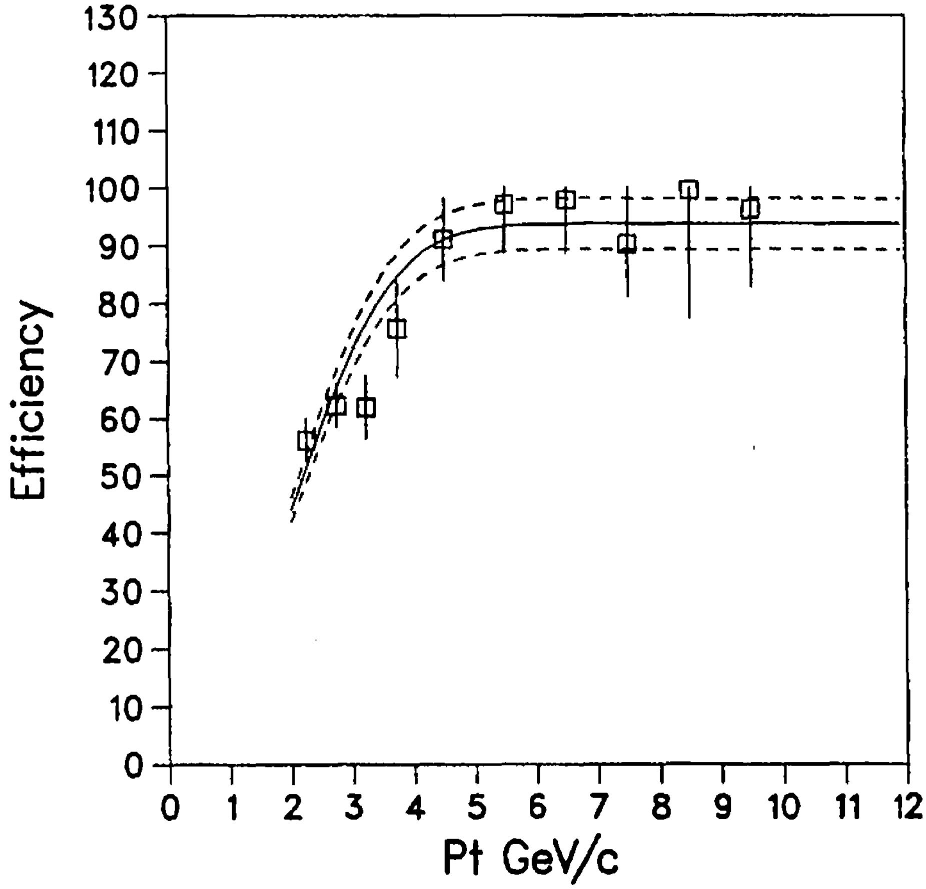

Figure 4.2: The level 1 trigger efficiency as measured with cosmic ray muons and lower momentum volunteer muons [37]. The solid curve is a fit to Equation 4.1, while the dashed curves are the same parameterization with A and α_c varied by $\pm$ 1 σ.

The next level of the trigger decided if the detector was to be read out to the event builder. The level 2 trigger decision was provided within about 20 to 30 μs, depending on the complexity of the event. Upon a level 2 accept decision, the detector was read out.

Readout took just over 1 ms and incurred less than 10 % deadtime. The level 2 dimuon trigger included muon stubs (the level 1 central muon candidates) and CTC tracks found by the Central Fast Tracker (CFT), a hardware track processor [38] which detected high transverse momentum tracks with fast timing information from the CTC.

The CFT identified tracks by analyzing prompt hits from the axial sense wires of the CTC. These hits were compared to predetermined hit patterns for the range of transverse momenta allowed by the CFT trigger threshold. The processor covered the p_T range above 2.5 GeV/c. For tracks 2.5 GeV/c $< p_T <$ 15 GeV/c, the CFT provided a momentum resolution of approximately 3.5% $\times(\frac{p_T}{1\,GeV/c})^2$. The CFT was designed to find tracks in p_T regions, the highest region for all tracks with $p_T >$ 15 GeV/c. Thus the CFT had no momentum resolution above $p_T >$ 15 GeV/c. The list of tracks found was available for use in level 2 triggers.

When the CFT finished the pattern recognition procedure, it sent a list of tracks to a hardware system called the muon match box. The muon match box contained lookup tables stored in read-only memory to match the CFT tracks to level 1 muon stubs. The lookup table was designed to take into account the magnitude of such effects as track curvature and multiple scattering of charged particles traversing the calorimeters on the way to the muon chambers. If a level 1 muon candidate stub matched a CFT track, a match defined as consistent with pointing to the same muon wedge, a bit was set in an $\eta\phi$ map which labelled the muon candidate as a "gold muon". This map was merely an array of bits corresponding to each muon wedge. There were 24 muon wedges around the detector in 2 separate η regions, so there were 48 bits available in the map.

This map of gold muons was then processed by a device called the gold muon cluster finder. This cluster finder's purpose was to merge gold muon candidates which were in adjacent muon wedges into a gold muon cluster. This had the effect of turning 2 real muons into one gold muon candidate if they were in adjacent wedges. Muon wedges were defined as adjacent in ϕ if on the same η side of the detector or adjacent in η if in the same ϕ region. This merging minimized the rate from jet events with more than one track from jet activity leaking into the muon chambers, while keeping most of the actual dimuon rate. The level 2 dimuon_central_3 trigger required two or more gold muon clusters.

The level 2 dimuon_central_3 trigger, in summary, consisted of the following requirements; 1) 2 level 1 muon trigger stubs in the event, 2) the CFT track associated with the muon stubs must have a transverse momentum greater or equal to 3 GeV/c, and 3) at least two gold muon clusters. This had the effect of excluding muons which were in adjacent wedges in $\eta\phi$ as described above.

The level 2 dimu_central_3 trigger efficiency was studied with data using non-muon and non-CFT triggers [37]. The efficiency for the CFT to tag muon candidates which had passed the level 1 muon trigger was measured beginning with a muon stub which triggered at level 1, and had an associated CTC track. Information from the muon matchbox tables was examined to see if CFT tracks had been associated with the candidate. The CFT efficiency for muons with $p_T > 3$ GeV/c was found to be $(99.5 \pm^{0.3}_{0.6})\%$. For events with two muon stubs with $p_T > 3$ GeV/c, both of which passed level 1 and which satisfied the non-adjacent geometry, the number of events which actually passed the level 2 dimu_central_3 trigger was examined. This resulted in a measured efficiency of $(98.5 \pm^{1.0}_{2.0})\%$, consistent with the CFT efficiency for both muon candidates.

Level 3 cuts were not needed for this trigger. The level 3 trigger was a software trigger, which ran from Fortran source code on nodes of a computer network. The algorithms selected on complicated quantities and filters, and reduced the trigger rate by keeping good trigger events. Since the dimuon rate was low, and the signal relatively clean, there was no need to include more complicated cuts for the dimuon_central_3 trigger.

Chapter 5

Offline Reconstruction

The offline reconstruction identified particles from tracks in the wire chambers and energy depositions in the calorimeters. The data from the detector was analyzed to find events with properties consistent with jets, electrons, high energy photons, muons, etc. Those features of an event consistent with objects of interest were called physics object candidates.

Physics object candidates were defined according to different criteria depending on the object desired. For instance, a central muon candidate object, or CMUO, was defined as a CMU stub matched with a CTC track. This matching was performed by extrapolating the CTC track to the muon chamber position. The extrapolation included the effects of the magnetic field inside the solenoid, the return yoke and the calorimeters. It took into account multiple scattering and energy loss in the material traversed. A central photon candidate was identified by the presence of energy in a central electromagnetic calorimeter tower, accompanied by clusters of energy in both views of the associated central strip chamber. Since the reconstruction of the reaction $\chi_c \to J/\psi\gamma$, $J/\psi \to \mu^+\mu^-$ is the subject of this analysis, μ and γ candidates will be emphasized.

The offline reconstruction included a complex series of algorithms to find these physics object candidates. The algorithms could find the interaction z vertex for the event (and/or the number and positions of such vertices if there were more than one), the charged tracks in the CTC, the energy deposition in the calorimeters, and the CMU stubs. They could also combine information from different parts of the detector, as in, for example, linking the CMU stubs with CTC tracks.

5.1 Event Vertex Determination

The offline analysis began by finding the z location of the event along the beam line. This was the first step because it was important for many other parts of the offline reconstruction. For example, the z vertex was needed for CTC track parameterization, beam vertex constraints, and ascertaining photon direction. The interactions had a large spread in z because the p and $\bar{p}$ beam bunches were long. The intersection of these bunches was such that the distribution of event vertices at the B0 interaction point in the Tevatron collider was well described by a Gaussian along the beam axis with a standard deviation in the z direction of 30 cm, as shown in Figure 3.7. The subdetector specifically designed for the purpose of event vertex determination was the VTPC (see section 3.3).

The process of z vertex determination started with finding VTPC track segments. The hit patterns of the wires in each VTPC octant of each segment were examined for consistency with coming from a charged particle track (or tracks). Since most tracks were straight in an octant, this was a relatively simple reconstruction. In addition, the number of hits in a given octant was small, resulting in a low number of possible combinations. A VTPC track segment was defined by the following requirements. First, the number of wires with hits in an octant was required to be greater than five. Second, the hit occupancy for the region containing the track was required to be greater than or equal to 70 percent. Third, the residuals of the hit positions, calculated as described in section 3.3, from the track path were used to calculate a χ^2. The uncertainties used in the χ^2 calculation were underestimated by a factor of 1.5 to 2.0 [39]. Since the average number of hits was 24 per track, the χ^2 for most tracks averaged around 100. This χ^2 was required to be less than or equal to 1000 for a good track, which rejected only extremely poorly measured tracks. The entire VTPC was searched until all VTPC track segments were found.

Once all of the VTPC tracks were identified they were grouped together to find the common vertex of the event, or events if two $p\bar{p}$ collisions had occurred. Each VTPC track segment necessarily had a z intercept, defined as the position of the point on the track closest to the z axis. These z intercepts from all of the tracks were clustered into sets to form z vertex candidates with no more than 2 cm separating nearest neighbors. Each cluster would become a vertex candidate. A new cluster was started if the z intercept of a VTPC track segment was greater than 1.5 cm from the center of the cluster. Once all z intercepts were assigned a cluster, a 1.5 cm window was found which maximized the number of intercepts in that window. The average z was calculated for each cluster window. Then all of the tracks were compared to these cluster centers and reassigned (to a new cluster) if they fell within the 1.5 cm window. This process was iterated until the mean of the z intercepts was within ± 1 cm of the previous mean. If a track fell within 1.5 cm of two separate clusters, it was assigned to the closest. The cluster with the largest number of segments used in the fit was chosen as the primary event vertex.

The efficiency of this algorithm was checked by scanning events. For the sample of minimum bias events which was examined, the efficiency for correctly locating the z vertex of the event was determined to be $(98\pm^{.7}_{1.3})$ %. Minimum bias events were all events resulting from a prescaled trigger consisting of only BBC hits in time with the beam collision time (a level 0 trigger alone). For a sample of physics specific triggers selecting high p_T, high energy, or high multiplicity events, the scan established that the efficiencies for correctly locating the z vertex was $(99 \pm^{.1}_{.4})$ %. The resolution of the z vertex as determined by the algorithm was determined to be about 2 mm by dividing the spread of the cluster by the square root of the number of tracks in the cluster.

A subtlety which was glossed over to this point in the reconstruction and deserves explanation is how the beam location itself was defined. The z vertex position found above gave only the z coordinate of the interaction vertex. However, the location of the beam varied in x and y from run to run. The exact path of the beam for each run was determined (by a method described below), and could be combined with the z vertex information to find the position of the event vertex.

5.2 Charged Track Finding

The trajectories of charged particles were found by examining CTC information. The list of hit wires and the associated drift times was the starting point of the track finding. For each hit sense wire, the drift time t, coupled with the drift velocity v_d, and the global event time t_0, defined two points in space, equidistant from the wire at $\pm d = v_d|t - t_0|$ along the drift trajectory for the wire.

The next step in tracking was pattern recognition. This grouped hits consistent with arising from a single particle's ionization track into a list of tracks. It was natural to begin the pattern recognition by finding track segments in each drift cell, since there were a limited number of hits per cell. Also, higher p_T tracks yielded relatively straight small segments. Since the time left an ambiguity as to which side of the sense wire the ionization occurred, a track would leave two segments with symmetry around the sense wire plane. This ambiguity was resolved when the segments were linked into tracks.

The pattern recognition algorithm then linked the segments together by starting at the outer axial superlayer and examining "roads", or bands of probable particle trajectories which could produce the drift cell track segment. The road was computed from the segment center going to the origin, and took into account the slope of the track segment. Axial superlayers along the $r - \phi$ plane road were examined for segments which were consistent with the trajectory hypothesis. The roads were re-calculated or dropped at each successively smaller layer. Finally, when the inner axial superlayer was reached, the stereo layers were examined, outer to inner, for segments resulting in a helical road.

At this point, there was a list of tracks which included the hits used in each track. The side of the drift wires of each hit should have been determined by which segment hypothesis remained in a track. Thus the list of hits was a list of points in space associated with each track. Hits were allowed to be associated with multiple tracks, up to the number of found tracks which passed through the drift cell.

The final step of tracking was a fit of the helix track parameters to the list of hits for each track. A charged track helix in the CTC must have been co-axial with the magnetic field, and thus it could be completely specified by the following variables:

- R, the signed radius of the helix ($R = \pm|R|$). The sign is the sign of the charge of the particle
- $\cot\theta$, where θ is the pitch angle of the helix
- z_0, the z position of the closest approach of the helix to the z axis, nearest the primary vertex
- d_0, the distance in the $x - y$ plane from the z axis to that same point of closest approach

- ϕ_0, the ϕ angle of the tangent to the helical track at that same point of closest approach.

The fit included all hits which were in the hit list for the track, provided they were acceptably close to the helix parameters, according to a complex heuristic algorithm [40].

The fit could also include the beam line position (as determined below). This was useful for tracks which came from the primary event vertex because the increased lever arm resulted in better determination of the curvature as well as $\cot\theta$. This beam-constrained fitting was used for the events including dimuons from the J/ψ sample. Even though some of the J/ψ came from long-lived b-flavored hadrons, the decay length would have been around 200 μm, while the resolution of the CTC track extrapolations to the beam vertex was similar. In the absence of a vertex detector, beam constrained tracking gave better resolution.

For tracks which were not expected to come from the primary vertex, such as conversion candidates or $K_s \to \pi^+\pi^-$ decays, the beam constraint was not used. The tracking using only CTC hits was called un-constrained tracking. However, due to the pattern recognition using the primary vertex to define roads, some bias in track parameters toward the primary vertex was retained, as will be briefly discussed in Chapter 6.

As mentioned previously, the radius of the helical track of a charged particle travelling in a magnetic field is related to the transverse momentum of the particle. This leads to the relation with the radius of the helix

$$p_T = c|qB||R| \tag{5.1}$$

where c is the speed of light, q is the charge of the particle, and B is the magnetic field strength. Other relevant quantities could also be derived from the track parameters, such as

$$p_z = p_T \cot\theta \tag{5.2}$$

and the momenta at the point of closest approach

$$p_x = p_T \cos\phi_0 \tag{5.3}$$

$$p_y = p_T \sin\phi_0. \tag{5.4}$$

The resolution due to the finite measurement resolution was $\frac{\delta p_T}{p_T} \simeq 0.0020 p_T$ for isolated tracks (p_T in GeV/c) if the track traversed all of the superlayers. With a beam constraint, which added length to the lever arm, this became $\frac{\delta p_T}{p_T} \simeq 0.0011 p_T$ [41]. There was also a term due to multiple scattering, which allowed the p_T resolution to be parameterized by [42]

$$(\frac{\delta p_T}{p_T})^2 \simeq (0.0011 p_T)^2 + (0.0066)^2. \tag{5.5}$$

The resolution for $\cot\theta$ was estimated to be $\delta\cot\theta \simeq 0.003$ for unconstrained tracks, and $\simeq 0.002$ for beam constrained tracks [43].

5.3 Determination of Beam Line Position

The beamline did not traverse the detector exactly through the origin or exactly parallel to the z axis. There were actually an offset and slope, which were run-dependent. Although the beam profile was smaller than the single event primary vertex resolution, the tens of thousands of events in a run could be used to fit the beam line parameters for the run. These beam line parameters could be used, in conjunction with the z position of the event vertex, to provide the $x - y$ position of an interaction with a much better resolution than possible with only information from the tracks from that single interaction.

All CTC tracks consistent with coming from the primary vertex of any event were used to determine the run by run beam offsets and slopes. These could be used to determine the x and y position of the primary vertex from the z position of the vertex as determined from the VTPC information. This was done to find the point of origin for photons from the decay $\chi_c \rightarrow J/\psi\gamma$, which was useful in determining the photon direction vector as described in Chapter 8.

5.4 Central Muon Object Reconstruction

The central muon object (CMUO) reconstruction was performed to find muon candidates in the CMU detectors. The CMUO identification began with finding track segments in the CMU, as described below. Once good track segments were found, these were associated with CTC tracks.

5.4.1 Central Muon Track Stubs

The CMU track segment (CMUS) finding algorithm reconstructed the position and direction of charged particle tracks in the central muon detectors. Tracks were first found in the $r-\phi$ plane, as described below. Then, $r-z$ plane tracks were found. Finally, the two views were matched to form the track segments, also known as muon stubs.

Tracking in the $r-\phi$ plane began with the number of found TDC hits in each wedge (n_{TDC}) to define track candidates, then fit the hits to a track. If the number of hits was less than two, the wedge had no CMU track segments. If $n_{TDC} = 2$, there was a possibility that the hits were from an isolated muon. If the two hits were in different layers, and in cells that were separated by fewer than two cells in the $r-\phi$ direction, the hits were assigned to two track candidates. There were two track candidates because with only two hits the ambiguity of which side of the drift cell the track was on could not be resolved.

If $n_{TDC} > 2$, tracks were found via a more complicated method. If more than one layer had no TDC hits, no track was found, but if at least three layers had hits, the search continued. Every combination of two hits separated by two layers defined extrapolated lines for a possible track candidate. The other planes were checked for hits within a road of 0.25 cm in the $r-\phi$ coordinate, which was about 10 standard deviations on the hit position. If at least one hit from the other layers was within the road, the hits were assigned to a track candidate. If all the hits used in a track were in the same cells as those in another track candidate, the duplicate candidate (the second track found by the algorithm in these cells) was dropped. If $n_{TDC} < 6$, it was assumed only one track was present, otherwise the tracking process was iterated over all pairs of tracks separated by two layers, up to a maximum of 75 track candidates. The hits for each track were then fit to a line, which resolved the ambiguity of which side of the drift cell the track occurred.

The $r-z$ plane tracks were then found with a method similar to the above, but using the number of ADC hits (n_{ADC}). If n_{ADC} was less than two, no tracks were found in the wedge. If $n_{ADC} = 2$, and the cells were at least adjacent in the $r-\phi$ direction, $r-z$ tracks were fit. If $n_{ADC} > 2$, and the hits were in at least three different layers, roads of width 5.0 cm (about 10 standard deviations in the $r-z$ coordinate) were searched for any hits. If there were any, the hits for each track (up to 75 tracks) were fit to a line.

The last stage of muon stub reconstruction matched the tracks in the two views. If the tracks in the two views shared at least two cells, they were matched and provided a CMUS. For any leftover $r-\phi$ tracks which remained unmatched, hits in the $r-z$ plane were re-examined for the possibility of providing a lower quality $r-z$ track. If hits in the $r-z$ plane (which showed no track) fell in any two cells with $r-\phi$ hits from the leftover track, a new $r-z$ track was constructed and matched to the $r-\phi$ track.

5.4.2 Linking CTC Tracks to Muon Stubs

Once track segment stubs were found, the CMUS stubs were associated with CTC tracks, beginning with the tracks. Each CTC track with $p_T > 1$ GeV/c was extrapolated to the

CMU position. Tracks below a transverse momentum of about 1.4 GeV/c were expected to range out in the calorimeter and never reach the muon detectors. The position calculation included a nominal dE/dx for a minimum ionizing track traversing the coil and calorimeters. The effects of the return field through the CHA were also included in the extrapolation. In the dE/dx calculation, and the track extrapolation, multiple scattering was not modelled, but the calculation of the uncertainties in the extrapolated position did include the effects of multiple scattering.

Tracks from decays in flight prior to the CTC were expected to have large impact parameters relative to the $\bar{p}p$ beams. To exclude most of these from the matching procedure, an impact parameter requirement of 1.0 cm or less was imposed.

Each extrapolated track which had enough momentum to reach a CMU wedge was considered a candidate for matching to any stub in that wedge. The extrapolated position and slope in the CMU was calculated for track-stub linking. A χ^2 was determined from the residuals in position and slope weighted by the multiple scattering deviations expected for a 1 GeV/c particle. This was done, instead of a χ^2 based on the actual momentum of the track, in order to minimize bias against high momentum tracks. High momentum tracks would have had lower deviations from multiple scattering, thus a falsely high χ^2 if the muon chamber were slightly mis-aligned with the CTC. The track which matched the position and intercept in the CMU of the muon stub with the best χ^2 in the $r-\phi$ plane was retained as a muon candidate. However, if a track propagated near the ϕ crack between wedges (defined here as more than 35 cm from the center of the wedge), it was checked for a match with any stubs in both wedges.

The muon candidate, consisting of the CMUS and CTC track, was then required to have a transverse momentum greater than 2.0 GeV/c. Muons with a transverse momentum of less than 1.4 GeV/c would, on average, lose enough energy that they would stop before reaching the muon chambers. In addition, the CFT trigger was not fully efficient below $p_T = 2.0$ GeV/c as shown in Chapter 4. However, some real muons with $p_T < 2.0$ GeV/c would pass the muon triggers and make it to the muon chambers. To avoid matching muon stubs from these slow muons with other, higher momentum tracks in the event, the extrapolation process began with tracks with p_T more than 1.0 GeV/c as outlined above, while the 2.0 GeV/c cutoff was not imposed until after the track-stub matching was complete. Track-stub pairs passing all the above requirements were labeled as central muon objects, or CMUO's.

5.5 CES Clustering

The CES was sensitive to electromagnetic showers from electrons and photons. The purpose of the offline CES reconstruction was two-fold. The finer segmentation of the CES (as compared to the CEM towers) provided a better position measurement for finding where the energy was deposited in the tower. This gave direction information for the electron or photon, and was useful in position dependent energy corrections. Also, the number of single particle showers and the number of multiparticle showers in a sample could be determined by examination of the lateral shower profile. For instance, the decay $\pi^0 \to \gamma\gamma$ would be expected to produce a wider energy deposition by virtue of the distance between the photons when they reached the calorimeter. The CES reconstruction found the position of the shower, and provided a measure of the lateral shower profile.

Since the channel width of the strip chambers was so thin, CES energy deposition was grouped into clusters to find positions and shower profiles. This clustering proceeded separately in the strip and wire views. The CES reconstruction algorithm had three major facets:

- the selection of seed channels about which to define a cluster,
- the cluster definition, a decision on which channels belong to a given cluster, and
- the measurement of the cluster energy.

After CES channels were clustered, a fitting procedure to find the centroid of the cluster was performed. Each of these processes is described below.

The definition of seed channels was relatively straightforward. Any channel with an energy deposition corresponding to more than 0.5 GeV was defined as a seed. The list of seeds was ordered from highest to lowest in channel energy deposition. The seeds could then be used to define CES clusters.

The next step in the CES offline reconstruction was the actual cluster definition. The clustering began with the highest energy seed channel, then proceeded in a descending seed energy order. A cluster was defined as the 11 channels centered about the highest energy unclustered seed channel. The algorithm was then iterated for the next highest energy seed outside a previous cluster. Clusters were allowed to overlap, as long as the seed tower for the second cluster was outside the first, so a maximum of 5 channels could be shared between two clusters. The process continued until no unclustered seeds remained. This resulted in a list of clusters, each with 11 channels, and the seed channel responsible for each.

The cluster energy was found for each cluster. It was calculated as the sum of energy in each channel of that cluster. An effective threshold of 0.057 GeV deposited per channel set a limit on the smallest amount of energy which could be considered in the sum. The value for the threshold was roughly three sigma above the noise distribution for the CES. Channels below this threshold contributed zero energy to the sum. Furthermore, although the channel would still contribute to the profile fits described below, it would do so as an entry of zero energy. Channels in overlapping clusters shared the energy with each cluster in proportion to their seed energies. Because of this energy sharing when clusters overlapped, energies less than the effective threshold could be included in the energy sum and fits, so long as the entire channel energy was above the threshold.

The shower position was determined from a fit to the shower shape as measured in the CES. This cluster fitting relied on a standard profile, the shape to which the energy deposition per channel was fitted. The standard profile was measured from test beam electron data, at an electron energy of 50 GeV. The parameterization of the profile was a functional fit to the average energy deposition around the mean. The electromagnetic showers from these electrons were very collimated, since 91% of the energy of the standard profile was within the three central channels, while only 1.6% was outside seven channels. The shape of the standard electromagnetic wire profile is shown in Figure 5.1. When used

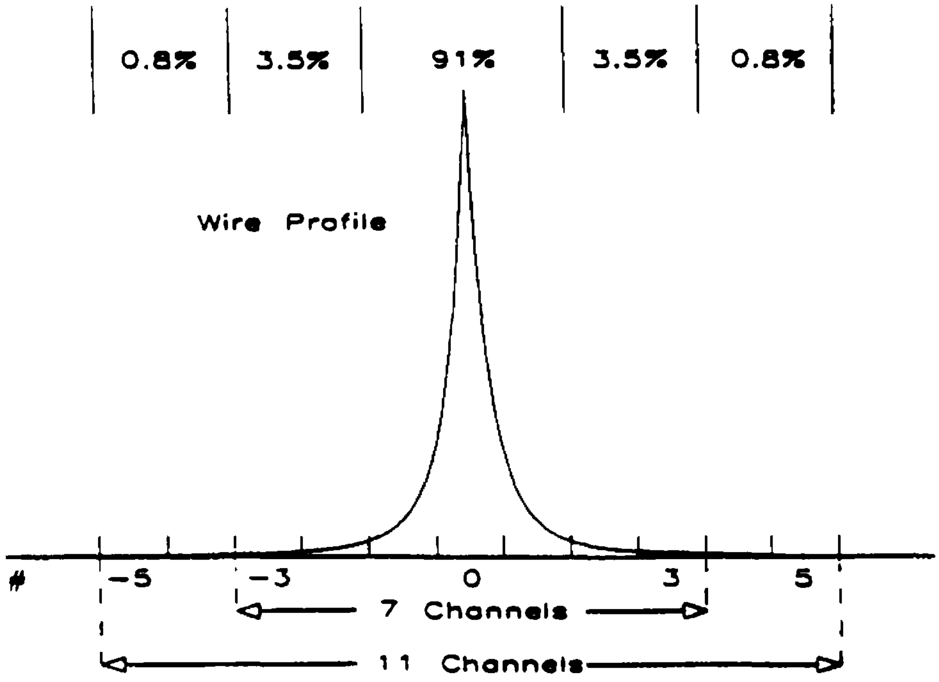

Figure 5.1: The Standard CES Wire Profile showing the channel cluster width

in the fit, the standard profile was scaled in height so that the area under the parameterized curve was equal to the cluster energy. The shape parameters other than the height were independent of cluster energy for test beam electrons with energies from 10 to 100 GeV.

The measured cluster profiles were then compared to the profile by a CES χ^2 variable, testing the quality of the fit. The standard profile, corrected for geometric effects, yielded a discrete channel by channel expectation $E(x_i)$ by integrating the value of the standard profile parameterization from one channel boundary to the other. The CES χ^2 was then calculated by taking the difference between the data and the channel expectation as follows:

$$\chi^2 = \frac{1}{4} \sum_{i=1}^{11} \frac{[E_i - E(x_i)]^2}{\sigma_i^2} \tag{5.6}$$

where i was the CES channel index, E_i was the measured channel energy, and σ_i^2 was the estimated variance of the profile. The variance σ_i^2 was also parameterized from test beam electron data [44]. The CES χ^2 was similar to a standard χ^2 per degree of freedom variable, with the exception of the arbitrary normalization of the constant factor of 4, instead of one less than the number of channels. The factor of 4 was historical, since originally 5 cluster channels had been planned. The number of channels per cluster was increased to 11 to include lower energy $\pi^0 \to \gamma\gamma$ in a single cluster, while the definition of CES χ^2 was unchanged. The CES χ^2 thus had a mean value of approximately 2.5 for electron showers.

The fit was performed by allowing the midpoint of the standard profile to float. The χ^2 was minimized, and the best center position of the standard profile was the CES cluster position. Since the standard profile was allowed to be at any position, the CES cluster position was not constrained to any channel center. This provided a resolution at high energies smaller than the individual channel size. Figure 5.2 contains the distribution of the position difference between cluster position and track extrapolated position for electrons, showing the resolution of the strip chambers was approximately 3 or 4 mm.

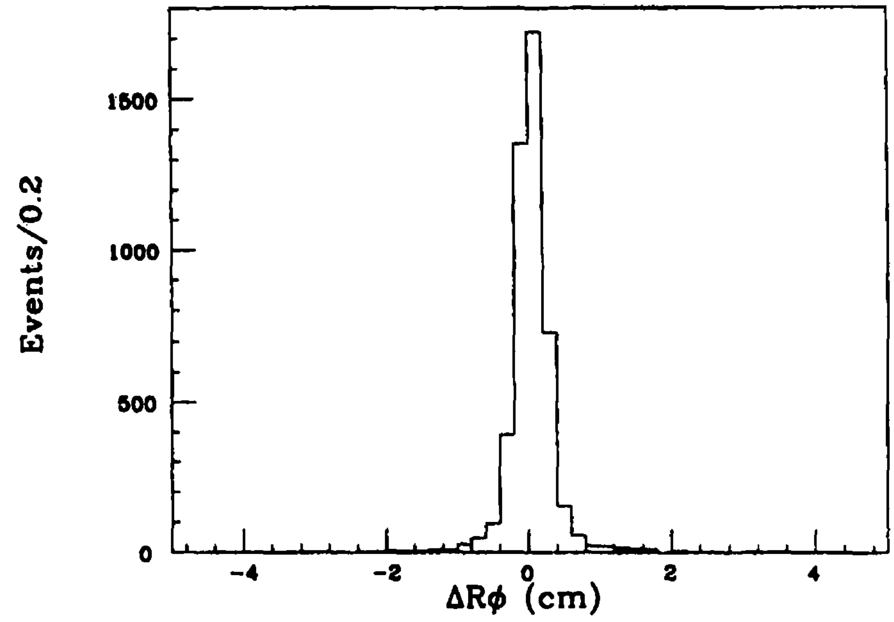

Figure 5.2: The position difference between cluster position and the extrapolated track position for electrons.

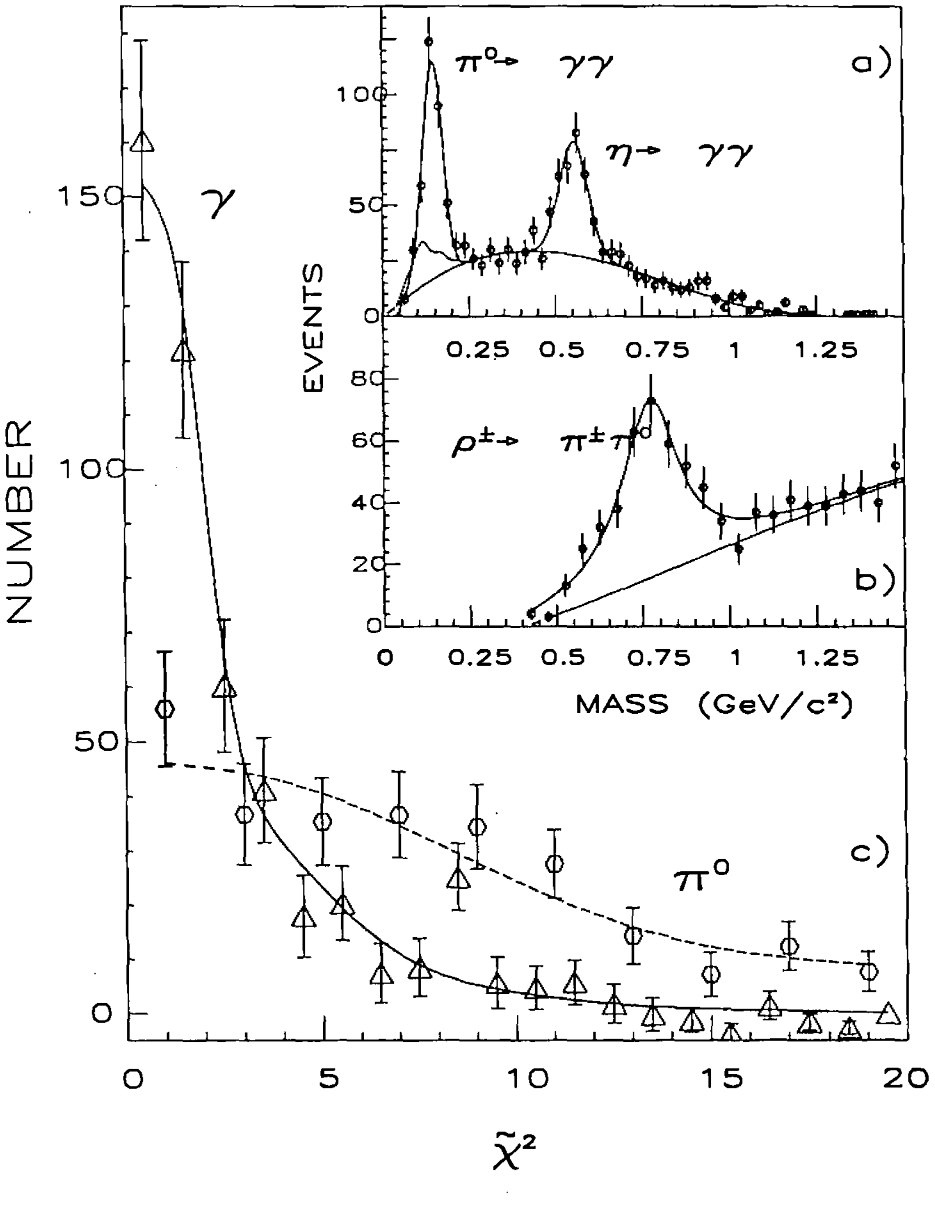

Figure 5.3: (a) The invariant mass of two photons from meson decays. (b) The invariant mass of a neutral cluster and a charged track. (c) The $\tilde{\chi}^2$ of photons from η decays in (a) and of π^0's from ρ decays in (b) compared to a detector simulation (curves).

The χ^2 resulting from the above was a measure of the quality of the fit. The average of χ^2 in both views, defined as $\tilde{\chi}^2 = [(\text{strip } \chi^2 + \text{ wire } \chi^2)/2]$, was the variable used to separate single photons from neutral mesons using the fit quality of the shower profile. Figure 5.3 shows that good agreement between the data and a detector simulation is obtained for the $\tilde{\chi}^2$ distribution of single photons from η-meson decays, and for single π^0's from ρ-meson decays [45]. For example, the efficiency for passing a $\tilde{\chi}^2 < 4$ requirement was $(79 \pm 5)\%$ for 10 GeV photon showers, while only $(43 \pm 5)\%$ for 10 GeV $\pi^0 \rightarrow \gamma\gamma$ showers.

5.6 CEM Energy Corrections

The energy response of the central electromagnetic calorimeter was position dependent, both within each tower and due to tower energy scale differences. The measured energy in the CEM was corrected for these effects.

The energy deposition was corrected for the response of a tower as a function of the azimuthal and z position of the electromagnetic cascade. The position of the shower was taken as the CES cluster position. The response correction was parameterized from test beam data [46, 47]. Figure 5.4 shows the relative response map as a function of shower position for a typical tower in the CEM.

A sample of about 17 thousand electrons with $E_T > 12$ GeV was used to normalize the calorimeter tower to tower response. The relative response peak for each calorimeter was determined from distributions of E/p. The standard deviation of this correction was three percent, while the largest single tower correction was 8%. The systematic uncertainty in E/p was estimated to be $\pm 0.4\%$ [48]. This correction established the overall energy scale.

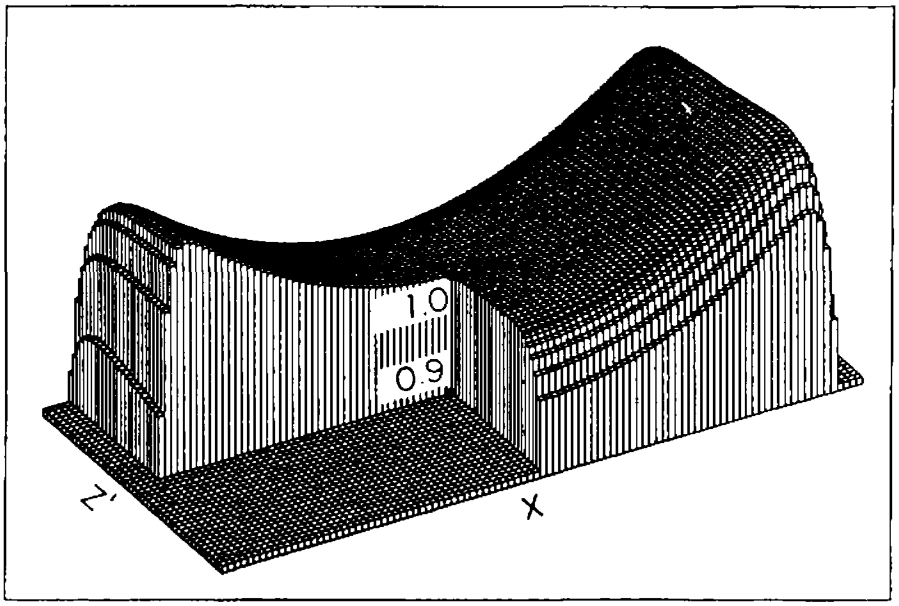

Figure 5.4: Relative response in a central calorimeter tower. The point labeled 1.0 is the point at which the tower is calibrated; the vertical scale gives the relative response.

5.7 Electron Candidates

Electron candidates were reconstructed beginning with a cluster of electromagnetic energy. The clustering process began by considering all CEM towers with at least 3 GeV of electromagnetic transverse energy to be seed towers. Transverse energy, or E_T, was defined by $E_T = E_{tower}\sin\theta$ where E_{tower} was the total electromagnetic tower energy, and θ was the angle of the line drawn from the tower center to the event vertex with the z axis. Adjacent towers were added to the cluster if their transverse energy was greater than 0.1 GeV. In the CEM, an electron shower was generally contained in one or two towers. Furthermore, the border between towers in the ϕ direction (which contained roughly 1 cm of inactive material as mentioned in Chapter 3) prevented energy from an electron crossing the ϕ boundary between towers. For these reasons, the size of a central EM cluster was restricted to three or fewer adjacent towers with a common ϕ. The cluster was required to have an E_T of 5 GeV or greater to be retained as an electron candidate.

A measure of the lateral shower profile for electron candidates is the variable $\mathcal{L}_{share}$. It was defined to be

$$\mathcal{L}_{share} = 0.14\sum_k \frac{M_k - P_k}{\sqrt{0.14^2E + (\Delta P_k)^2}} \tag{5.7}$$

where the sum is over the towers in the cluster adjacent to the seed tower, M_k is the measured energy in the adjacent tower, P_k is the expected energy in the adjacent tower, E is the cluster energy, and ΔP_k is an estimate of the error in P_k. The expected energy P_k was predicted using the EM cluster energy, the event vertex, the center of the shower as measured in the central strip chamber and a shower profile parameterization from test beam measurements. The uncertainty in the expected energy, ΔP_k, was taken to be the variation in P_k arising from a 1 cm shift in the center of the shower. The uncertainty in the cluster energy comes from the resolution of the CEM, $\sigma(E) \simeq 0.14\sqrt{E}$, thus the denominator normalized the energy difference $M_k - P_k$ relative to the statistical fluctuations inherent in the measurement of electromagnetic showers. For most events ΔP_k was small since the CEM had full containment (more than 99%) for showers more than 2 cm away from a boundary (the cell size was typically 24 cm long in z). The sum was arbitrarily normalized, and gave a measure of the isolation of the electron candidate. $\mathcal{L}_{share}$ was calculated for each central EM cluster, and was useful for providing a clean electron sample (see Chapter 6).

5.8 Luminosity Measurement

The Beam-Beam Counters provided a measurement of the luminosity delivered by the accelerator. This measurement scaled the BBC rate to a known cross section. The cross section was related to the BBC rate at a lower energy ($\sqrt{s} =$ 546 GeV) combined with accelerator parameters. The normalization was set by comparing to a UA4 measurement of the $\bar{p}p$ cross section at $\sqrt{s} =$ 546 GeV [49]. The cross section visible to the BBC was calculated to be σ_{BBC}(at $\sqrt{s}$ =1.8 TeV) $= 46.8 \pm 3.2$ mb [50]. The BBC rate was monitored, and provided the measurement of the total integrated luminosity gathered using the dimuon_central_3 trigger of 2.6 ± 0.2 pb^{-1}.

Chapter 6

Electromagnetic Efficiency

In the χ_c analysis, photons were found using the central electromagnetic calorimeter (CEM) energy and the central strip chamber (CES) cluster position. These photons would be combined with J/ψ candidates to find the $\chi_c \to J/\psi\gamma$ signal. The cross section was calculated using the various acceptances and efficiencies, including the photon efficiency. The photon efficiency determination is described in this section.

6.1 Overview of Method

The determination of the photon finding efficiency was done in two parts. First, since electrons interact electromagnetically in the CEM and CES much like photons, the electron finding efficiency was measured. This measurement was performed on an unbiased sample of electrons arising from $\gamma \to e^+e^-$ conversions. A check on the calibration of the CEM for electrons with energies in the range 1 to 5 GeV was also performed, since the calibration was designed for energies above 5 GeV. The photon finding efficiency was then found by correcting this electron finding efficiency for slight differences in the CEM and CES responses for photons versus electrons. The calculation of the response differences relied on detailed modelling of the behaviour of the CEM and CES.

6.2 Conversion Electron Selection

A sample of electrons unbiased with respect to calorimeter response was needed to measure the efficiency for finding low energy electrons. This sample was obtained from photon conversion electron pairs, identified by one electron candidate passing the electron calorimeter cuts and using only tracking information to identify the second electron. The "second" electron thus provided the required unbiased electron sample.

6.2.1 First Electron Selection

The first electron was chosen with the following selection criteria. First, all electron candidates (as described in Chapter 5) were examined from the inclusive election data sample. Electrons were expected to lose almost all their energy in the CEM while hadrons were expected to penetrate to the CHA. The ratio of hadronic energy over electromagnetic energy was therefore required to be less than 0.05 (this implicitly required the electron to be isolated from other activity in the event). $\mathcal{L}_{share}$ (as defined in section 5.7) was required to be less than 0.2 to provide a further isolation cut. The $\mathcal{L}_{share}$ distribution is shown in Figure 6.1, with the peak near zero containing the most isolated electron candidates. The cut at $\mathcal{L}_{share} = 0.2$ was on the plateau region.

The electron cluster was required to have at least one 3-D track aimed at it; for more than one such track, both the highest momentum track and the track passing nearest to the centroid of the CES cluster were used as electron candidates. The ratio of CEM energy to CTC momentum was required to be between 0.6 and 1.5 to make sure that the CTC track

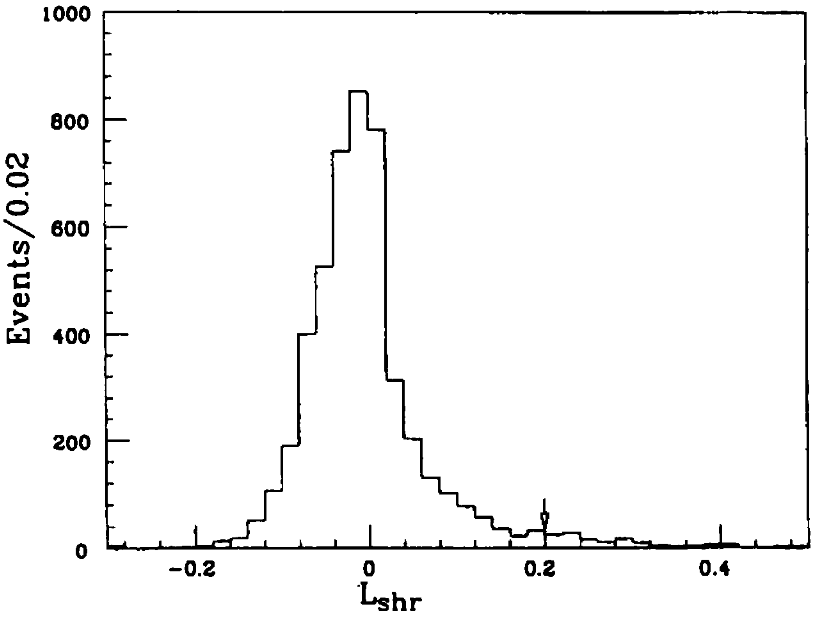

Figure 6.1: The $\mathcal{L}_{share}$ distribution for electrons.

was consistent with the deposited energy.

6.2.2 Initial Track Selection of Conversion Candidates

Once an electron candidate was chosen, all other tracks were examined for possible use in the conversion sample. The conversion pair candidates were required to have opposite charges. Pairs of electrons from a photon converting in the material of the detector would initially be travelling in the same direction. This fact was used to determine the constraints necessary to select conversions.

The most readily available check on whether two particles were initially travelling in the same direction was the difference between the measured value of $\cot\theta$ for each track. The value of $\cot\theta$ did not change as a track spiraled in the magnetic field, so no assumption on where the tracks originated was needed to make this a useful comparison. In addition, $\cot\theta$ was given directly from the fit helix parameters. Thus few calculations (and little valuable CPU time) were needed to make the comparison. Finally, the resolution on $\cot\theta$ was expected to be roughly Gaussian for isolated high quality tracks passing through all superlayers of the CTC. The resolution for such tracks was estimated to be $\sigma(\cot\theta) \simeq 3 \times 10^{-3}$ [43]. The difference in $\cot\theta$ for two tracks, $\Delta\cot\theta$, would have a resolution $\sqrt{2}$ larger, or about 4.2×10^{-3}. A large window, about 10 times the resolution on each side of zero, would guarantee a large fraction of conversion events would be selected, so a cut of $|\Delta\cot\theta| < 0.04$ was chosen. Any track pairs falling outside this window were dropped from consideration as conversion candidates.

Conversion electron-positron pairs, having opposite charges and starting off in the same direction, would curve away from each other in opposite directions due to the magnetic field. Since conversions originate from the same point, this would imply the $x - y$ view of the tracks would be circles tangent at that point. The distance which the circles approached at the line joining their centers would be zero for perfectly measured conversion pairs. For this reason, the distance of perpendicular approach, s, was calculated using the helix radii and helix centers of the tracks. The distance s was defined as the value of the $x-y$ distance between the helix centers minus the value of both helix radii. If the circles overlapped, s was negative, if tangent at one point, s was zero, and if the circles did not touch, s was positive. The requirement for the value of s was chosen assuming the resolution would be similar to the resolution for the impact parameter of a track, $\sigma(d_0) \simeq 0.2$ cm [43]. The difference between two tracks could be expected to be $\sqrt{2}$ larger, and a roughly 10 σ cut was chosen. Pairs were required to have $|s| < 0.3$ cm.

The probable conversion point in the $x-y$ plane for each track was defined as the point of intersection of the helix for that track and the line defined by the two helix centers. The overall conversion point was defined as halfway between these two probable conversion points. This gave a conversion x and y, or equivalently a conversion r and ϕ.

If the two tracks came from a conversion, they should have the same z coordinate at the conversion point. The z coordinate was calculated for the point on each helix at the conversion radius. The conversion z was defined as halfway between the z coordinates found for each track. The difference in z between the tracks at these points, Δz, further restricted the events used as conversion candidates. If the resolution for these z positions was similar to the z_0 resolution ($\sigma(z_0) \simeq 0.3$ cm [43]), a $\simeq \pm 10\sigma$ window on the z difference would be $|\Delta z| < 4$ cm. Events failing this requirement were dropped from the conversion candidate sample.

Photons arising from the primary interaction and converting in the detector would produce e^+e^- pairs which continued to move away from the beamline. The conversion radius, r, was given a sign, which was the sign of the vector scalar product of the conversion point (x,y) and the conversion pair momentum. The pair momentum was simply the vector sum of the two momenta calculated at the conversion point. Pairs moving away from the primary vertex would have a positive radius, so, to minimize the background to the conversion sample, the requirement $r > 0$ was applied.

At this point in the selection, cosmic rays or looping particles which were reconstructed as two separate tracks might have passed all the tracking requirements. Real conversions would have the e^+ and e^- travelling in the same direction. To cut out pairs of tracks not initially going the same direction, the scalar product of the two track momenta (as calculated at the conversion point) was also required to be positive.

Finally, the second track was extrapolated to the CEM, and was required to point to a different tower than the track associated with the first electron candidate. This was done to provide an unbiased sample when the calorimeter response was examined, so the energy deposition of the first electron would not interfere with the response measurements.

6.2.3 Final Conversion Sample Criteria

Since a high purity electron sample was desired, the distributions of the above defined variables could be examined to define tighter selection cuts on the conversion candidates. These cuts were tailored to the resolutions found for the (non-ideal) tracks in the sample. Other quantities such as the pair mass and radius of origin for each pair provided the final conversion sample.

Tracking Cuts

This section outlines the tight tracking cuts defining conversion pair candidates. The requirements were chosen by an examination of the various distributions mentioned above to find the actual resolutions. The figures in this section include all tight tracking requirements except on the quantity plotted.

Figure 6.2 shows the $\Delta \cot\theta$ distribution using the above cuts. The σ of the distribution was about 0.008, double that expected for ideal high-p_T tracks. An approximately $\pm 2\sigma$ cut was chosen, where conversion pair candidates were required to have $|\Delta \cot\theta| < 0.015$.

Figure 6.3 shows the distance of closest approach s. The circles were biased toward overlapping, since the pattern recognition pulled the tracks toward the beamline as mentioned in Chapter 5. This is shown by the peak being pulled to the negative values of s. The σ here was about 0.1 cm, (three times that expected for ideal high-p_T tracks), and the offset was about -0.05 cm. The cut $|s| < 0.16$ cm was chosen to select conversion pairs.

Figure 6.4 shows the difference in z at the conversion point, Δz. The σ was about 0.5 cm as expected, so an approximately $\pm 2\sigma$ cut was chosen, $|\Delta z| < 1.1$ cm.

Now it should be noted that the above cuts are tantamount to a conversion pair mass cut, so a mass distribution would not necessarily reflect any mass resolution, but since the object here is to define a relatively pure sample of conversions, there is no harm in cutting on the pair mass (calculated at the conversion point). To find the pair mass, only the track momenta and an assumption that both tracks were electrons provided the electron energy, $E_i = \sqrt{\mathbf{p}_i^2 + m_e^2}$. The energy sum $E = E_1 + E_2$ and the vector sum of the momenta $\mathbf{p} = \mathbf{p}_1 + \mathbf{p}_2$ provided the mass by the formula $m_{pair} = \sqrt{E^2 - \mathbf{p}^2}$. Figure 6.5 shows this pair mass, and a cut $m_{pair} < 0.2$ GeV/c^2 was chosen, well above that for most pairs passing the other selection requirements.

Geometric Cuts

These tight cuts were used to define the conversion candidates. Since conversion pairs should come from regions of more mass in the detector, it is fruitful to check the sample against detector geometry. Figure 6.6 shows the radius of conversion, and tracking detector radii are marked for comparison. The outer wall of the VTPC and the inner wall of the

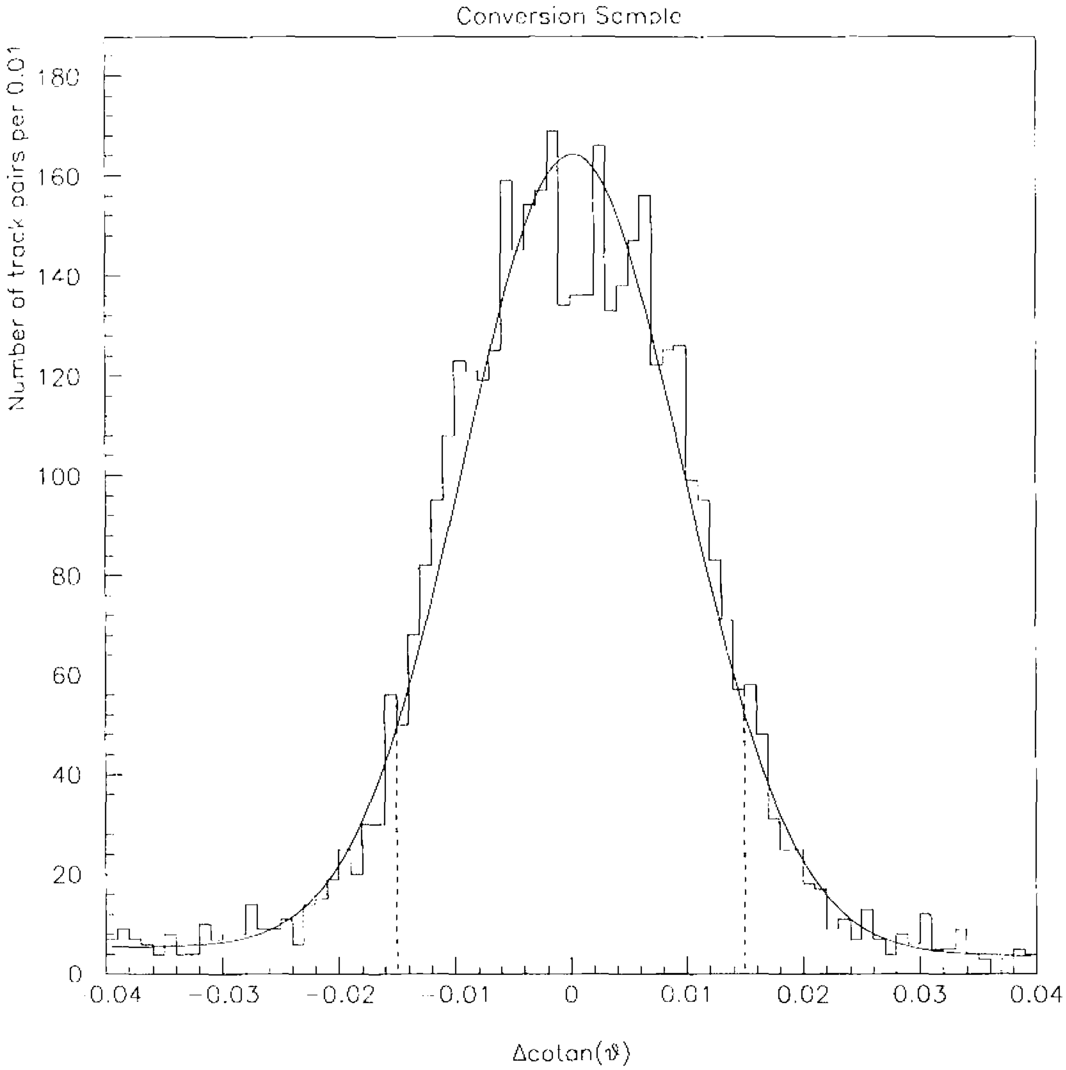

Figure 6.2: The difference in cotangent θ between pair candidates

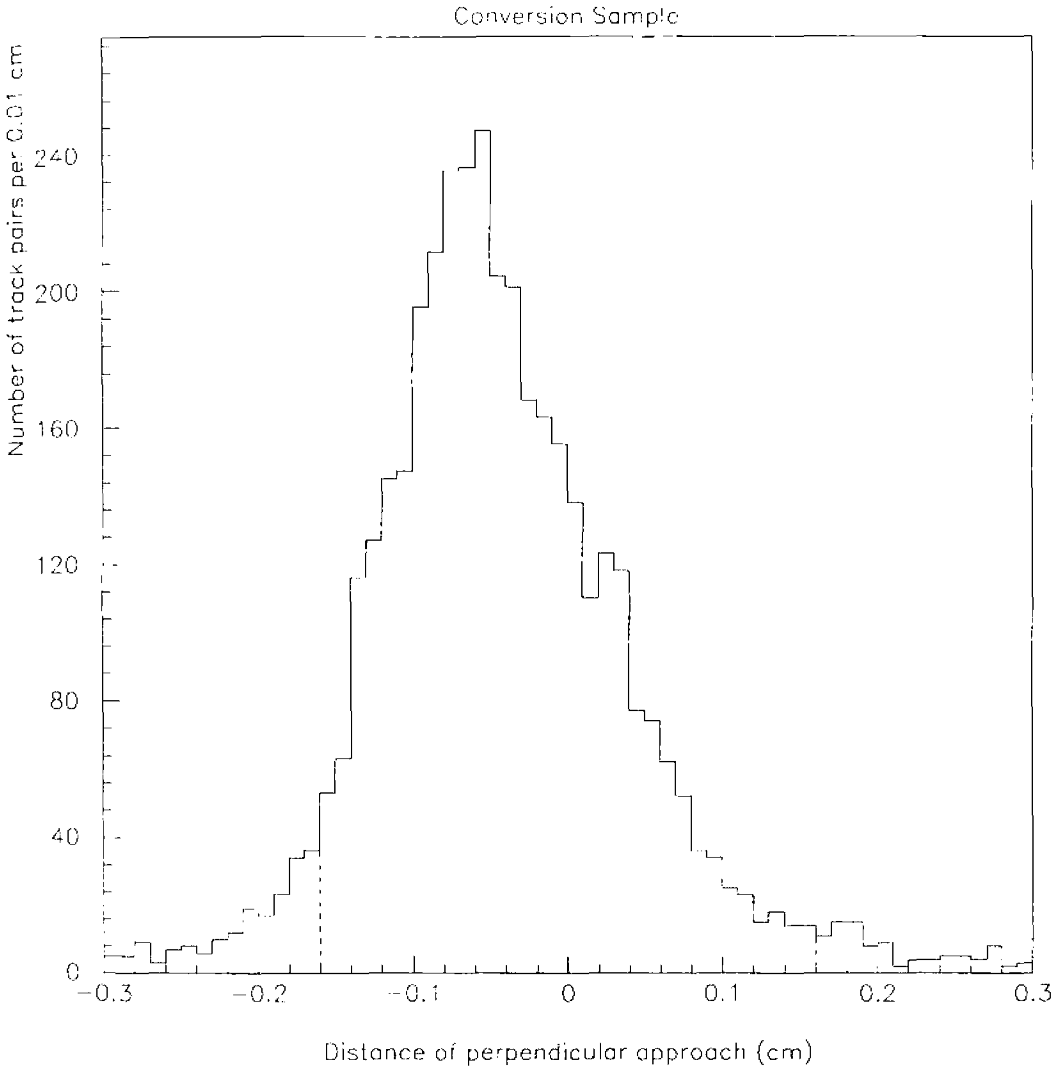

Figure 6.3: The distance of closest approach of conversion pair candidates

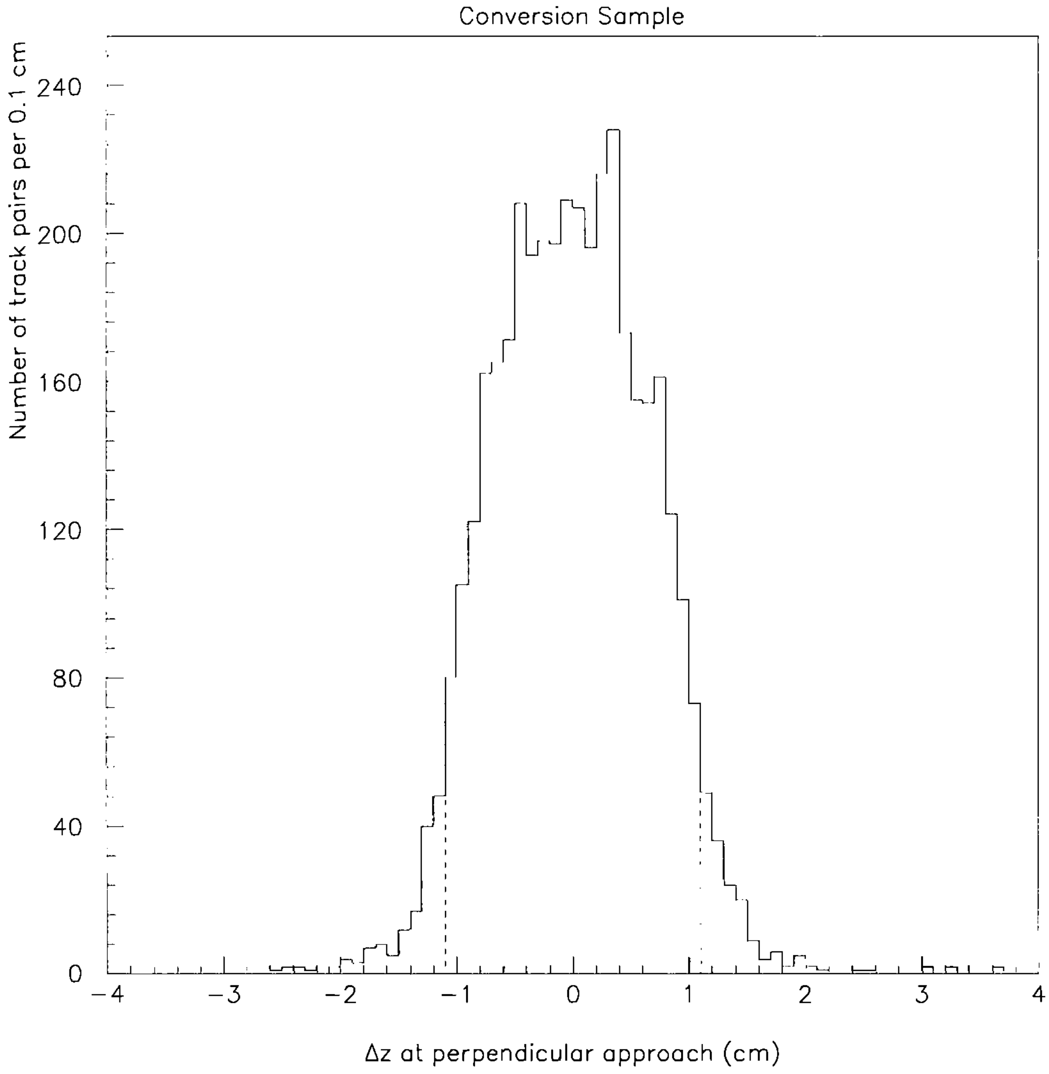

Figure 6.4: The z difference between conversion pair candidate tracks

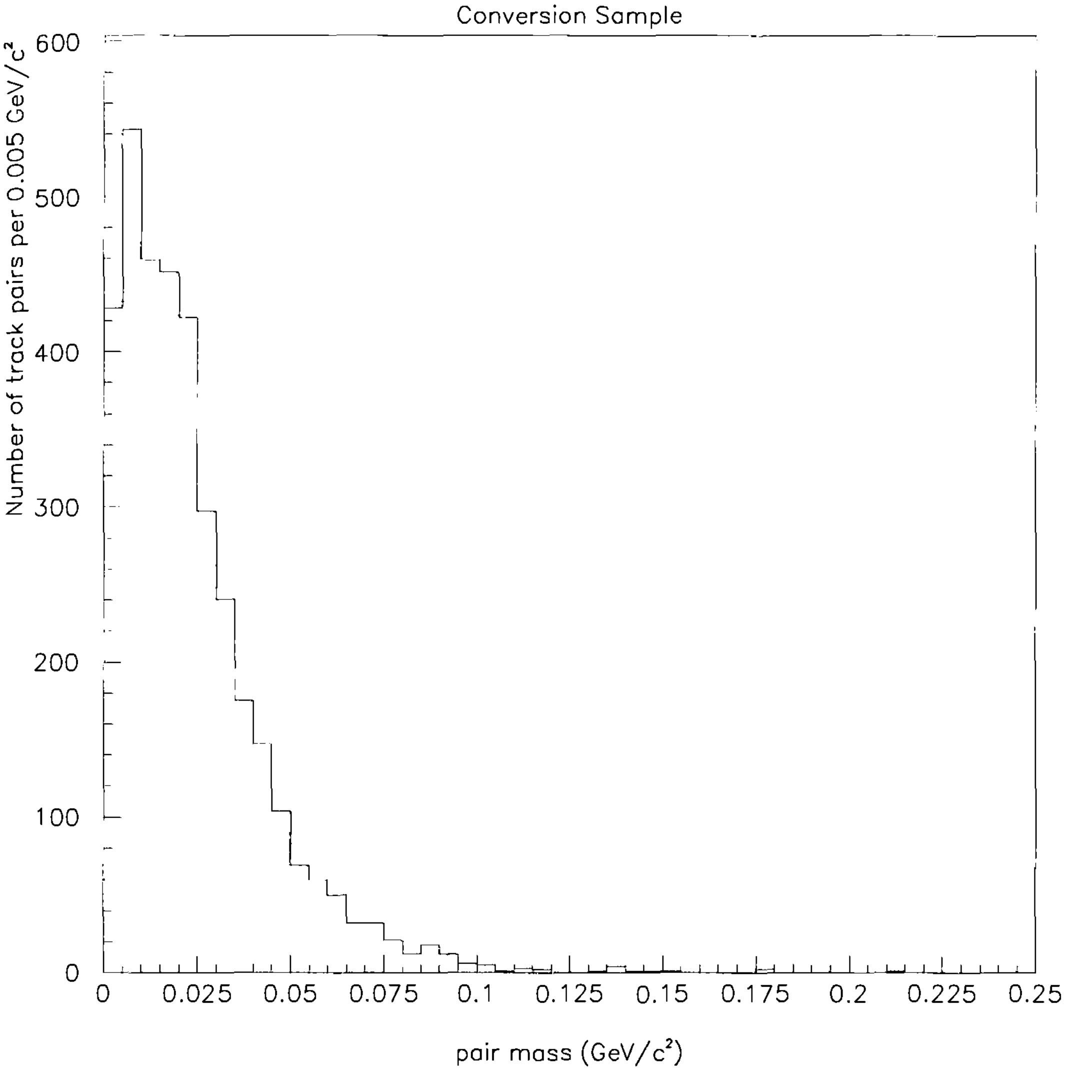

Figure 6.5: The mass for conversion pair candidates, calculated from momenta of the tracks and assuming the electron mass to determine the energies.

CTC contained the majority of the pair candidates. Figure 6.7 shows the z position of the conversion for the VTPC region $12 < r < 18$, and z positions of VTPC planes are clearly visible. The correlation of conversion candidates with the mass distribution in the detector indicate that the pairs were produced in a region where a photon-nucleon interaction could cause a conversion.

Now, the two dimensional views of the conversion point, analogous to "x-rays" are shown. Figure 6.8 shows the conversion radius vs. conversion z position. The VTPC structure is clearly visible. Figure 6.9 shows the conversion y position vs. conversion x position. Again, it was evident the pairs arose from regions where the VTPC outer structure and CTC inner cylinder provided mass, making conversions possible. Thus, these pair candidates were consistent with the expectations for a high purity sample of conversions.

In order to weed out the Dalitz pairs (e^+e^- pairs arising from the decay $\pi^0 \rightarrow e^+e^-\gamma$), and to improve the purity of the sample of conversions, the radius of conversion was required to be greater than 20 cm and less than 28 cm. This corresponded to the higher mass regions of the VTPC outer wall and the CTC inner wall. Since none of the cuts used to define a conversion sample relied on the calorimeter response of the second electron candidate, and the conversion sample was relatively pure, a sample of electrons unbiased by calorimeter information now existed.

6.2.4 Propagation to Calorimeter

The unbiased electron candidate tracks were extrapolated to the CEM, and the energy in the tower the track points to was examined. Figure 6.10 shows the deposited energy divided by the momentum of the track. The E/p distribution peaks around 1.0, as expected if both E and p are well measured. It should be noted that these distributions include those tracks which enter near inactive regions of the calorimeter. To address this, geometric cuts were

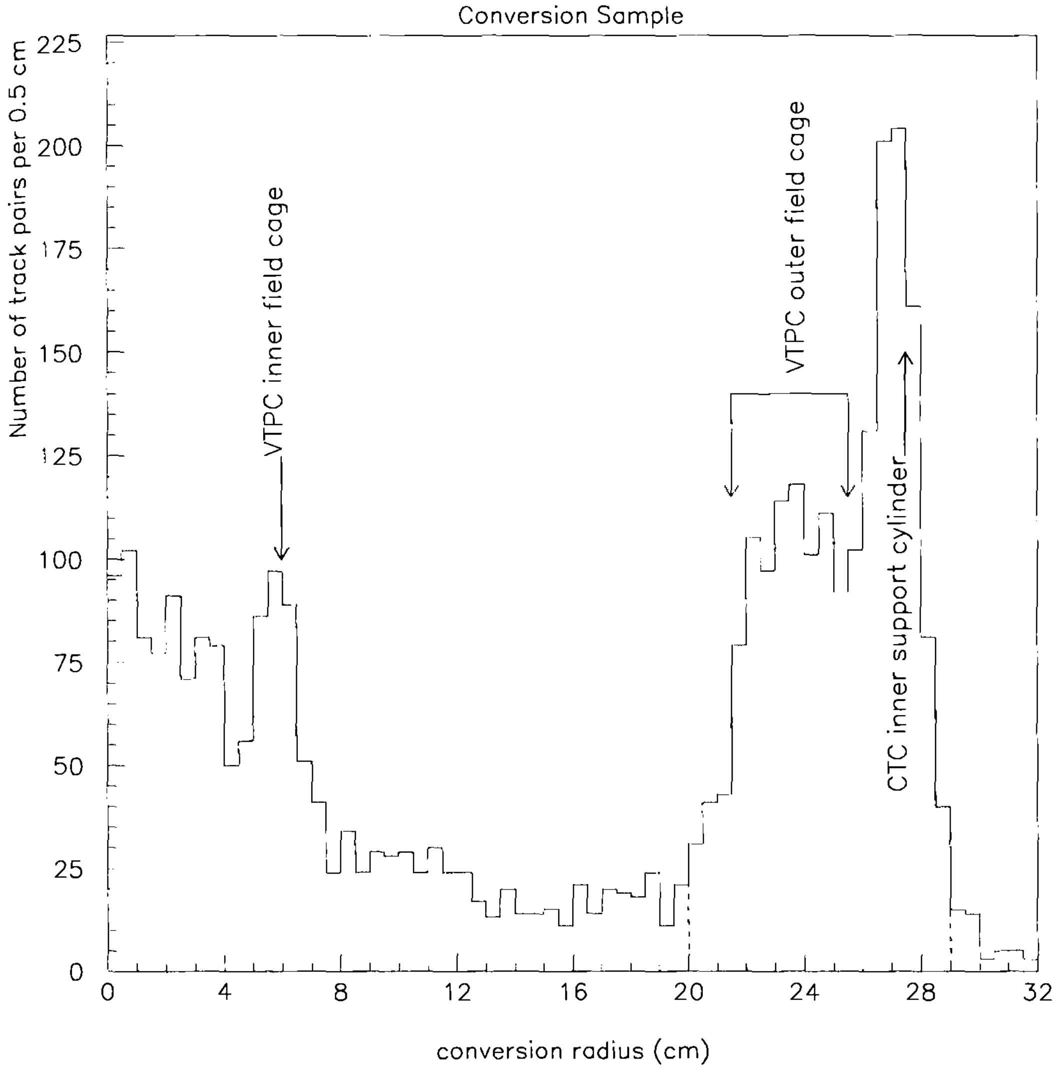

Figure 6.6: The radius of conversion for conversion pair candidates

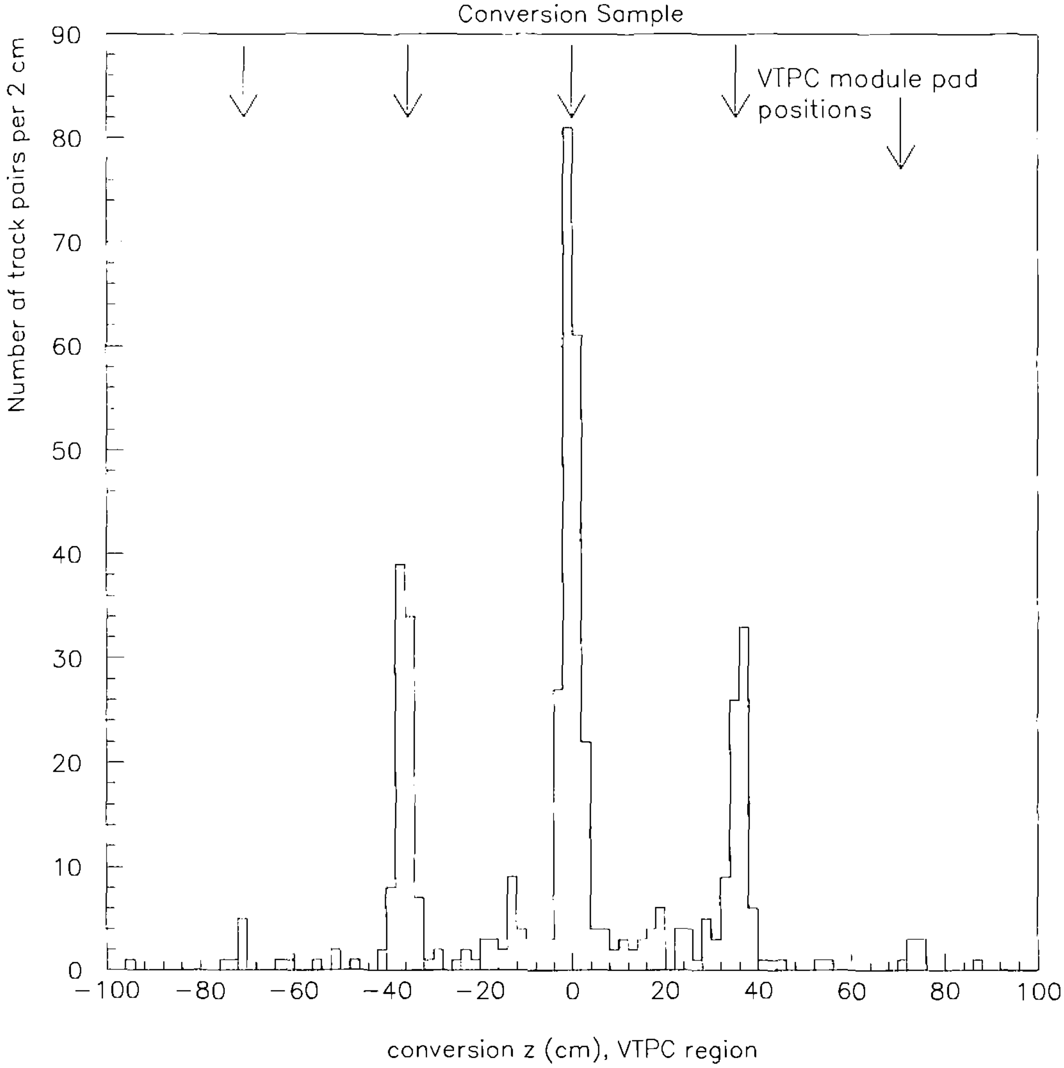

Figure 6.7: The conversion z coordinate for conversion pair candidates

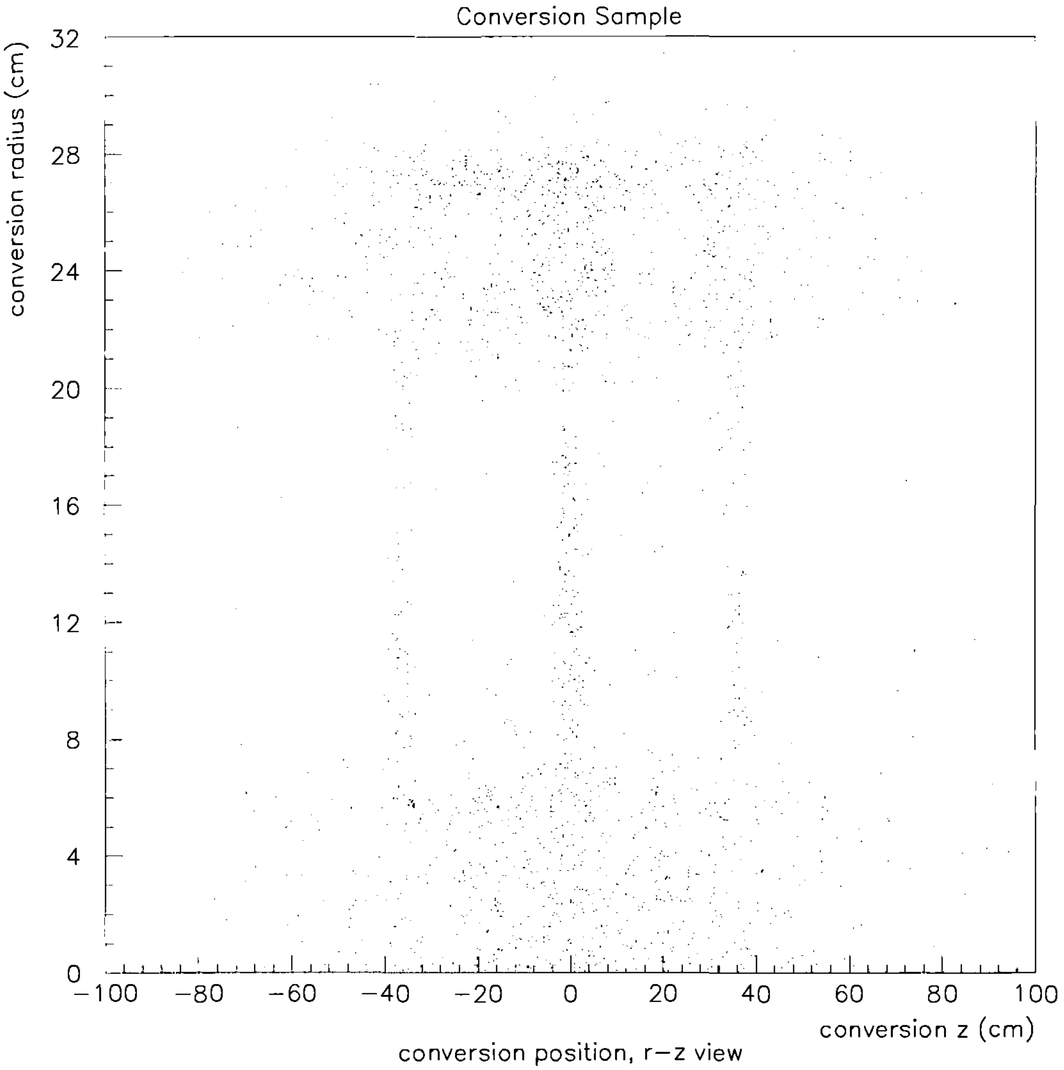

Figure 6.8: The rz view of the conversion point

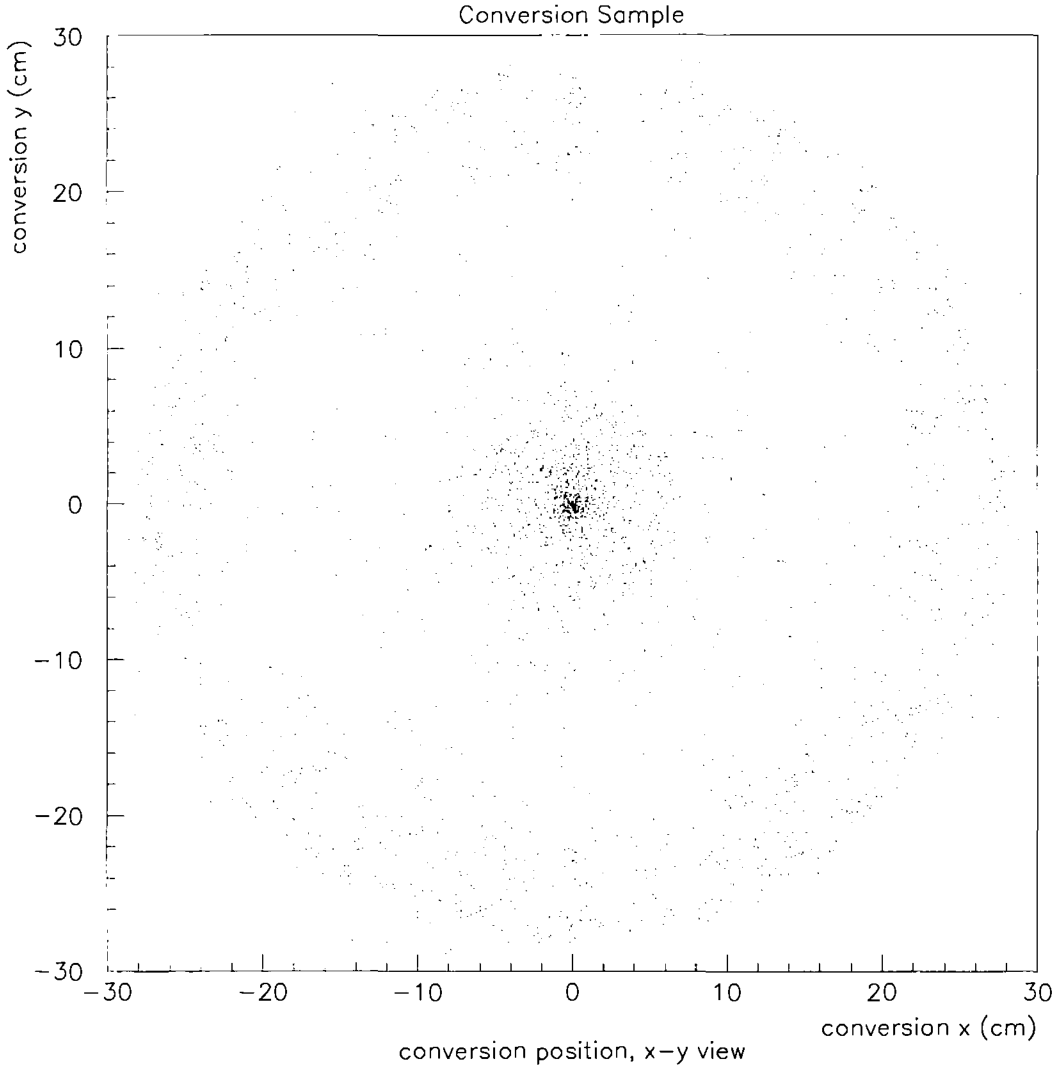

Figure 6.9: The xy view of the conversion point

made on the extrapolated track positions.

Geometric cuts were made to exclude cracks in the detector. The extrapolated $r-\phi$ coordinate of the track at the CES was required to be < 21 cm from tower center to avoid the ϕ cracks of the CEM. The cutoff of 21 cm was chosen since the scintillator active area extended to 23.1 cm from the center of the tower [46] and the standard lateral profile (see Section 5.5) contained over 95% of the energy within a ±2 cm window. Because the active area of the scintillator began at $|z| = 4.2$ cm, and particles could originate from $z \geq 30$ cm, it was possible for a particle to exit the calorimeter if the CES position was within 3.0 cm of the active region and deposit the energy in the dead region of the calorimeter near $z = 0$. Allowing another 2.0 cm to contain the shower placed the z cutoff at 9 cm. The extrapolated z of the track at the CES was required to be $z > 9$ cm to avoid the 90 degree crack. Only towers 0 through 5 were used, or $|\eta| < 0.55$, since the photons in the χ_c analysis travelled close to the direction of the J/ψ mesons which were limited to $|\eta| <0.5$.

6.3 Energy Resolution

The energy found in the CEM fiducial region was well measured. Figure 6.11 shows the corrected E/p distribution for those electrons striking good parts of the detector, with the peak near 1.0 as expected and cleaner than that without fiducial cuts. Since the resolution was dominated by the statistics of the electromagnetic shower, the expression for the energy resolution had the form $\sigma(E)/E \simeq C_{res}/\sqrt{E_T}$ [51] where C_{res} is a constant. If we assume that the momentum of the electrons is measured with a small error ($\sigma(p)/p \simeq 0.003$), then a measure of this $\sigma(E)$ was the width of the distribution of $(E-p)$. Therefore, the constant $C_{res} \sim$ the width of $(E-p)\sqrt{p_t}/p$. Figure 6.12 show the spread $(E-p)\sqrt{p_t}/p$, resulting in a measured standard deviation of 17%. This corresponded to an energy resolution of

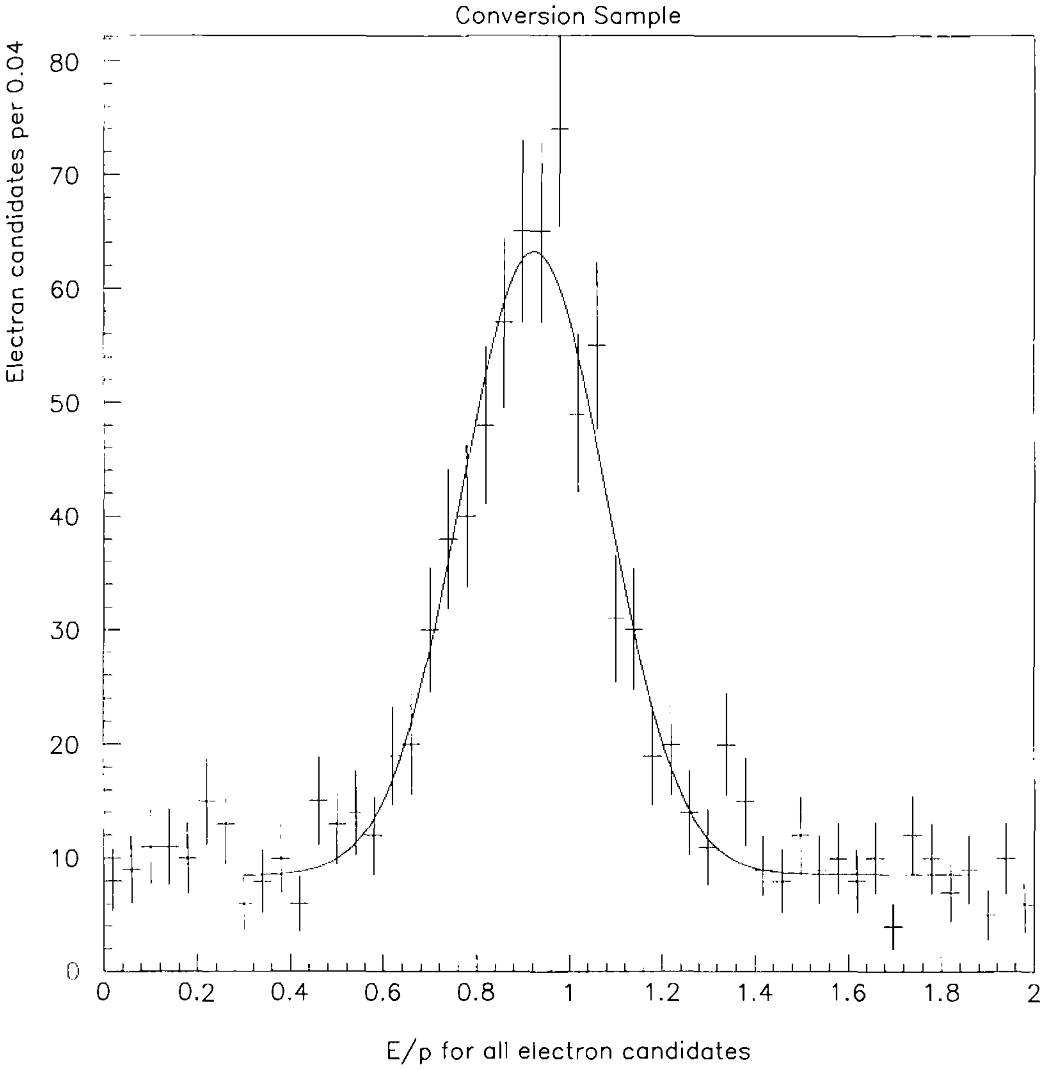

Figure 6.10: The electron energy over electron momentum

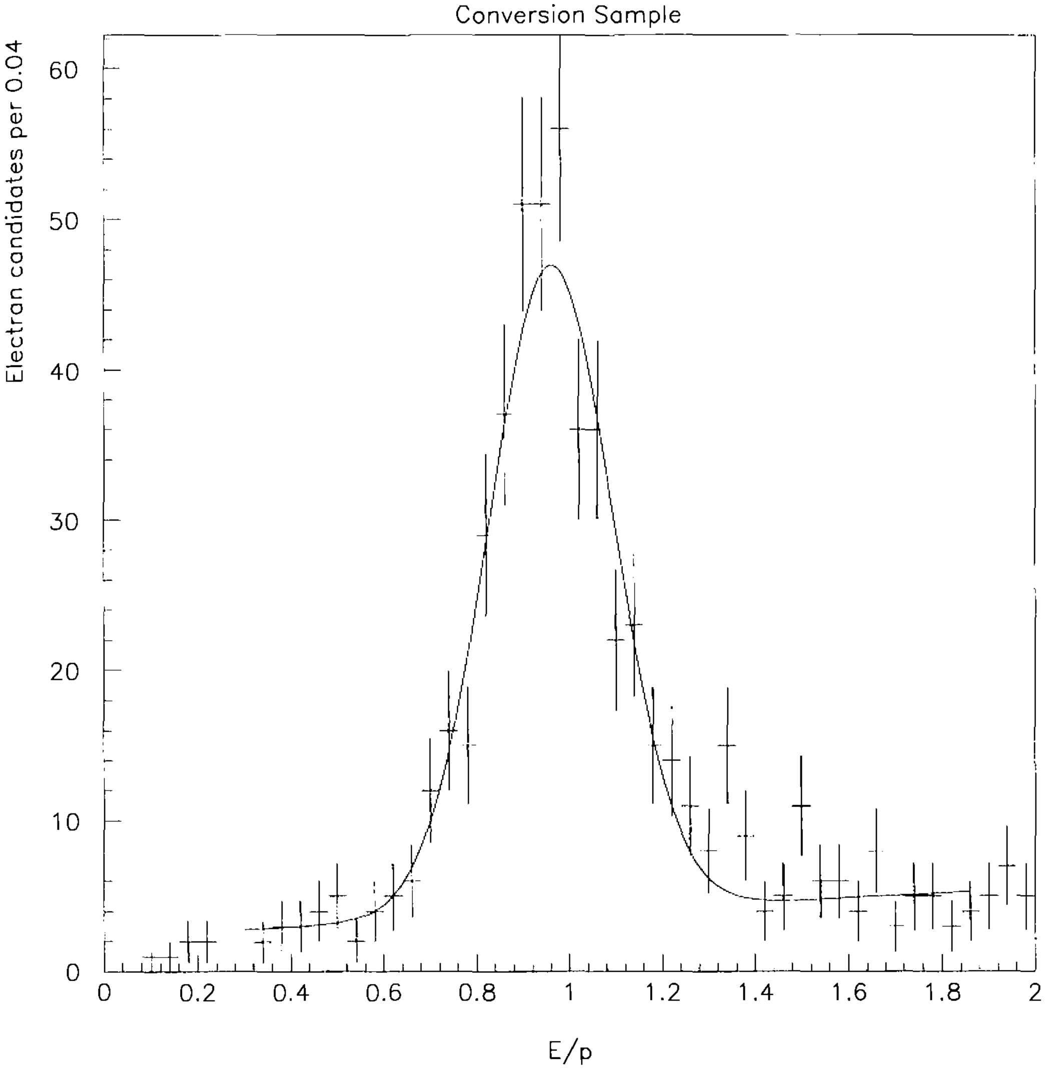

Figure 6.11: The energy over momentum for electrons

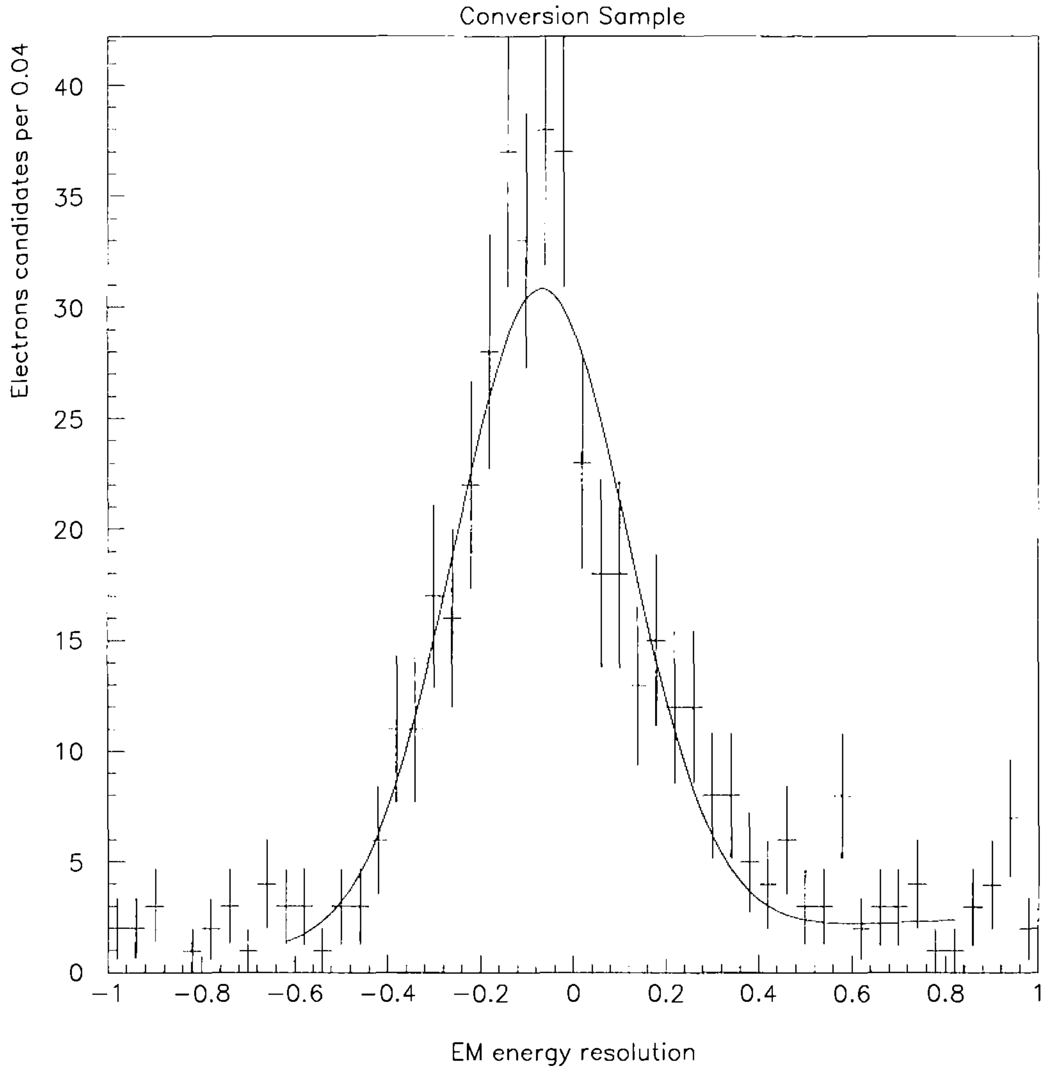

Figure 6.12: The resolution of the CEM

$\sigma(E)/E \simeq 17\%/\sqrt{E_T}$.

6.4 Position Resolution

The position resolution of the CES clustering was found by comparing the cluster position to where the electron track aimed. Figure 6.13 shows the track match to CES cluster positions in both the $r - \phi$ and z views. Fits to these distributions show that the position resolution for CES clusters arising from these electrons was around 0.8 cm in the $r - \phi$ direction, and 1.0 cm in the z direction.

6.5 Electron Efficiency

The electron efficiency was determined by the number of identified electrons which pass the electromagnetic cluster finding algorithm. The default clustering (outlined in Section 5.5) was used. Figure 6.14 shows the momentum of all tracks passing the cuts (including geometric), as well as the momentum distribution of those tracks which had a cluster with energy in both views. The electron efficiency was measured from the percentage of the electron candidates that produced CES clusters. Figure 6.15 shows the ratio of the two, which is the CES efficiency as a function of electron momentum.

The efficiency of the algorithm must also include the effects of energy cuts, since the energy resolution of the detector would affect the acceptance of energy requirements. Figure 6.16 shows the efficiency if, in addition to energy in both views of the cluster, an EM energy of 1 GeV was required. This was the efficiency (as a function of electron momentum) of the actual electromagnetic shower selection for this analysis.

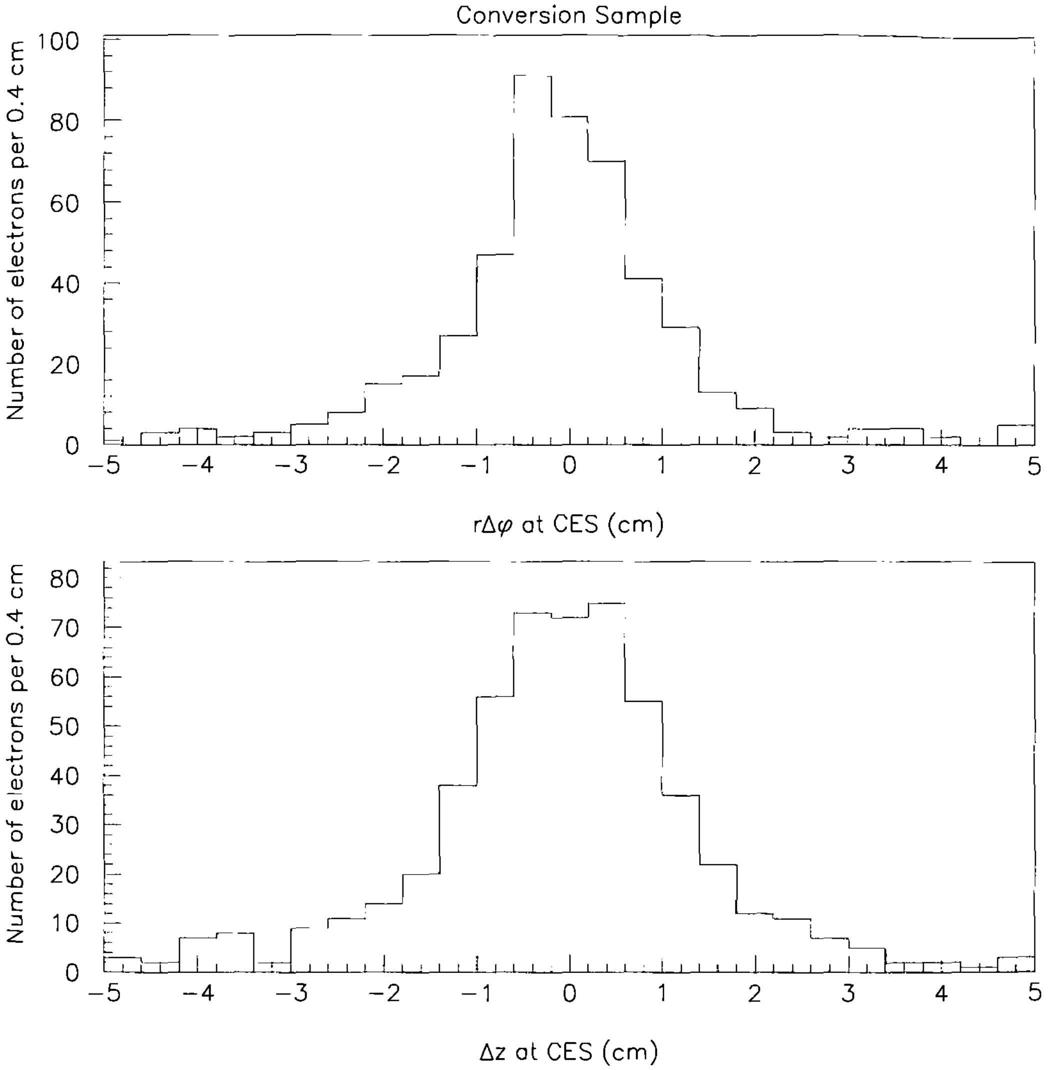

Figure 6.13: The CES cluster position match with tracks

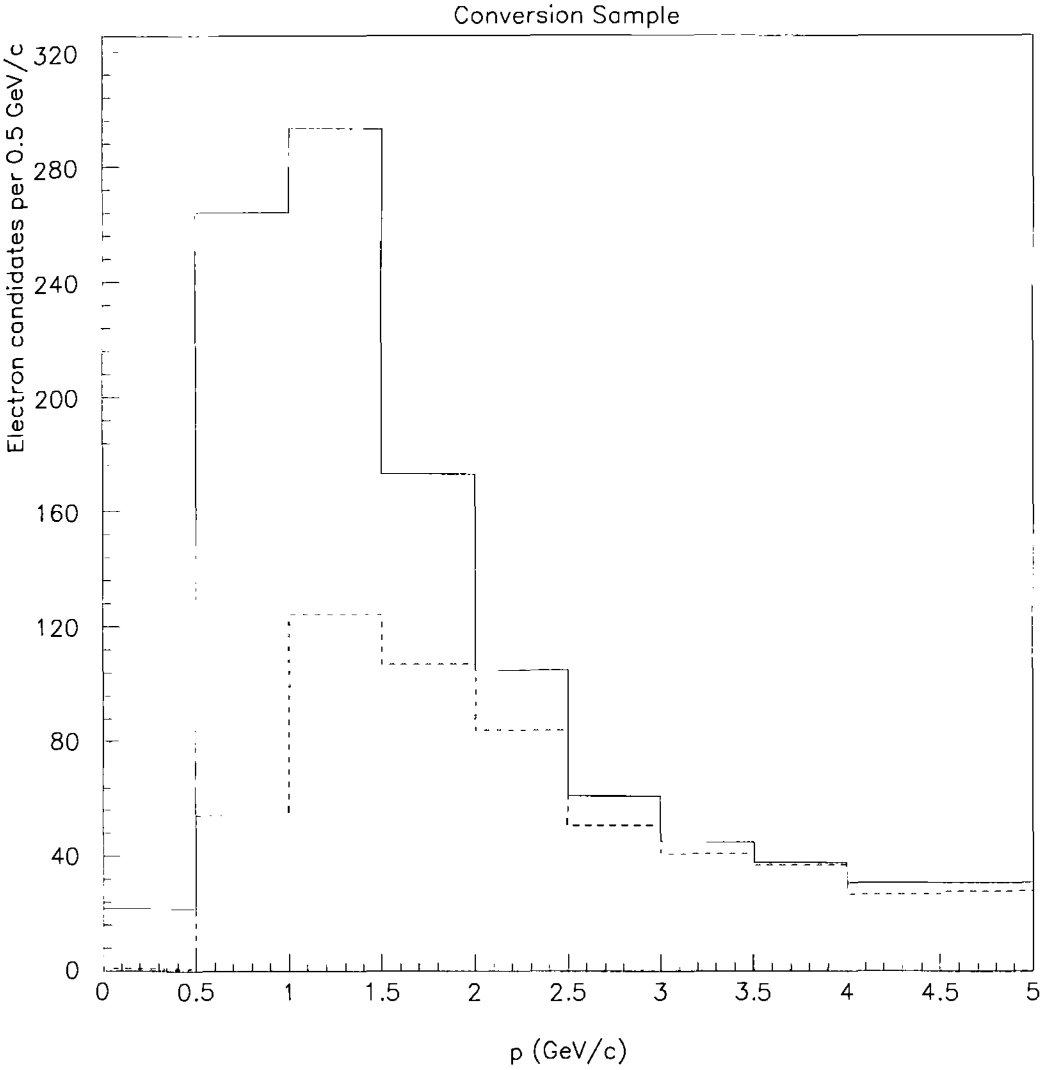

Figure 6.14: Electron momentum spectrum before (solid) and after (dashed) the CES cluster is found

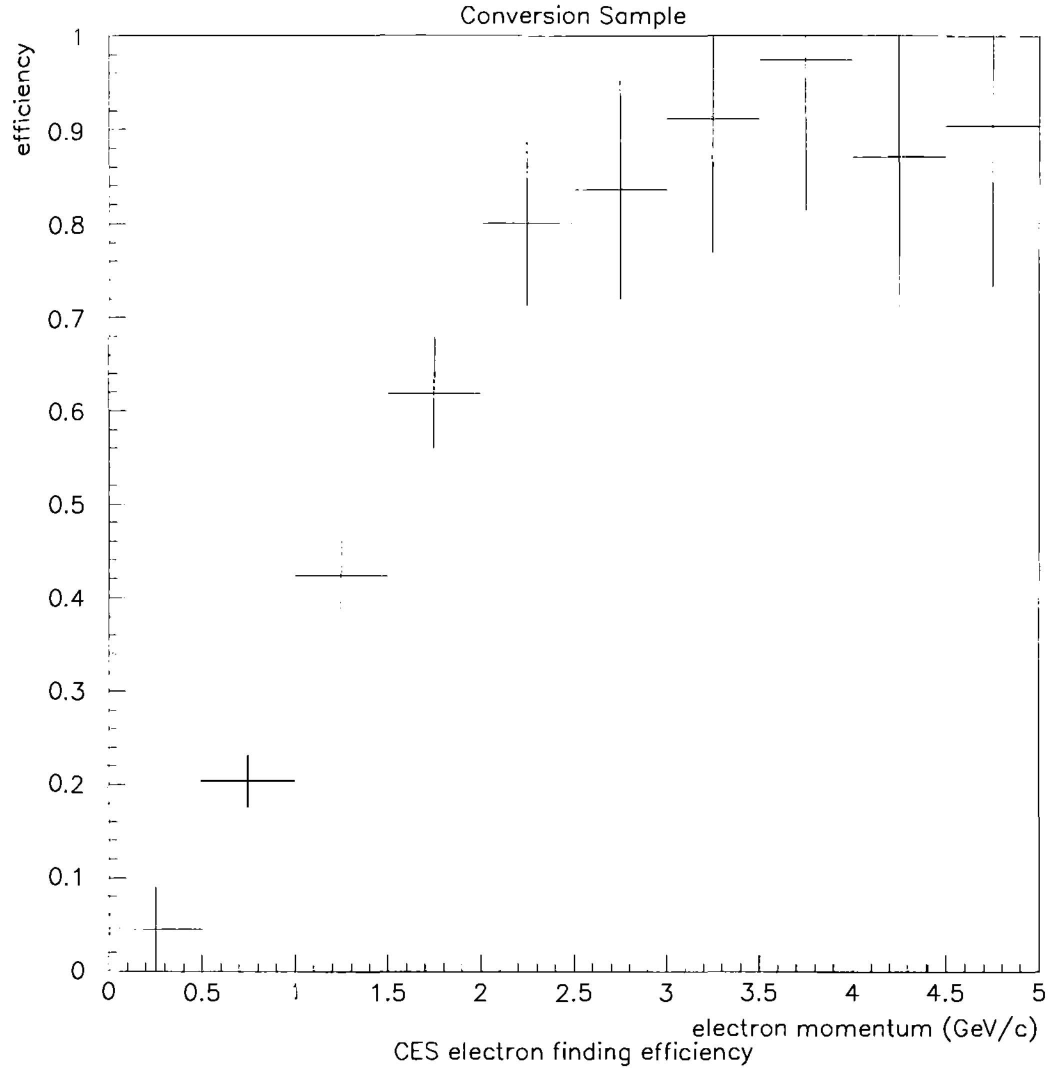

Figure 6.15: The CES efficiency for electrons

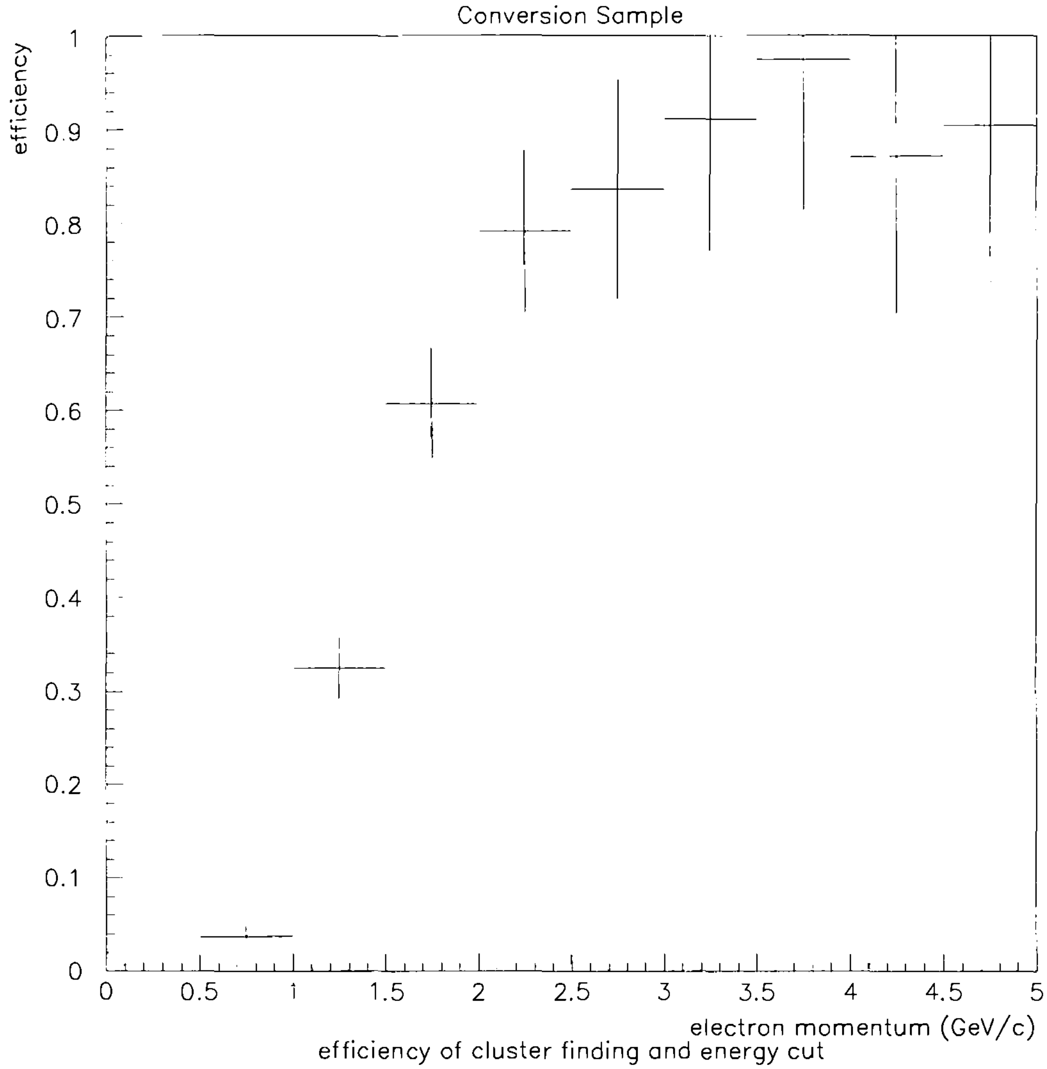

Figure 6.16: The electron finding efficiency

6.6 CES Simulation

The photon efficiency was slightly different from the electron efficiency due to a difference in longitudinal shower development. Electromagnetic showers produced by photons travelled further into the CEM, allowing more of the low-energy shower to reach the CES than was the case with electrons. To model the difference in efficiency arising from this fact, a GEANT (version 3.14) simulation of the CES response for both electrons and photons was performed. The GEANT simulations of electrons and photons in the CES were used to compare photon response with electron response. The electron simulation did a reasonable job of predicting the average pulseheight versus energy observed in the test beam electron runs, quantified in References [52, 53, 54]. This simulation produced tables of charge deposition segmented according to the CES geometry on an event by event basis. These events were then scaled according to the strip chamber gain and put into a form that could be processed by the strip chamber clustering code and clustered in the same way as the data was. The deviation of channel energy due to noise was $\frac{1}{3}$ the effective channel threshold and would contribute negligibly to the efficiency, so was not included in the model.

6.6.1 Comparison of GEANT Electron to Data

Electron showers were simulated with the CDF calorimeter geometry. The simulated electron shower profiles could be directly compared to those for the electrons in the conversion sample to ensure the showers were modelled correctly. First, a few distributions with widely varying detector gains (relative 0.625,1.0,1.25) for GEANT electrons were compared with data to test the efficacy of the GEANT simulation. These relative scales were to study the effects of uncertainties in the modelling of the gas gain in the simulation. Figure 6.17 compares the average wire cluster energy of GEANT electrons with the average from conversion electrons as a function of electron momentum. This figure shows that the actual gas gain in the detector was bounded by the chamber gain assignments in the simulation. Figure 6.18 compares the average energy for all generated GEANT events found to have non-zero cluster energy to the same average for the electron sample. This was the same as the previous plot with the exception of excluding events where no cluster was found. Again, the chamber gains used in the simulation resulted in similar energy response behavior to that observed in the cluster energies in the electron data. The real test of the usefulness of the simulation was how well it described the electron efficiency. Figure 6.19 compares the cluster finding efficiency for the simulation to that for electron data. The fact that the efficiencies match well shows the simulation did a good job at modelling electron shower development in CDF, and could be relied upon for a parameterization of electromagnetic shower development.

6.6.2 Comparison in GEANT: Electron to Photon

The simulation was then used to find the difference in CES detection efficiency for photon and electron showers. Figure 6.20 shows the GEANT ratio of efficiency for cluster finding of photons compared to that of electrons. The several different detector gains tested gave almost identical $e^{\pm}/\gamma$ response ratios. The electron to photon CES efficiency ratio differed from unity by less than 17% for all detector gains used and for all particle energies greater than 1.0 GeV, while the value of the ratio varied less than 3% for the different gains used. The slightly higher photon efficiency was due to the fact that at energies around 1.0 GeV, electron showers would be mostly included within the material before the CES, while photons would convert around 0.8 radiation lengths after the beginning of the material, and could reach into the CES more often.

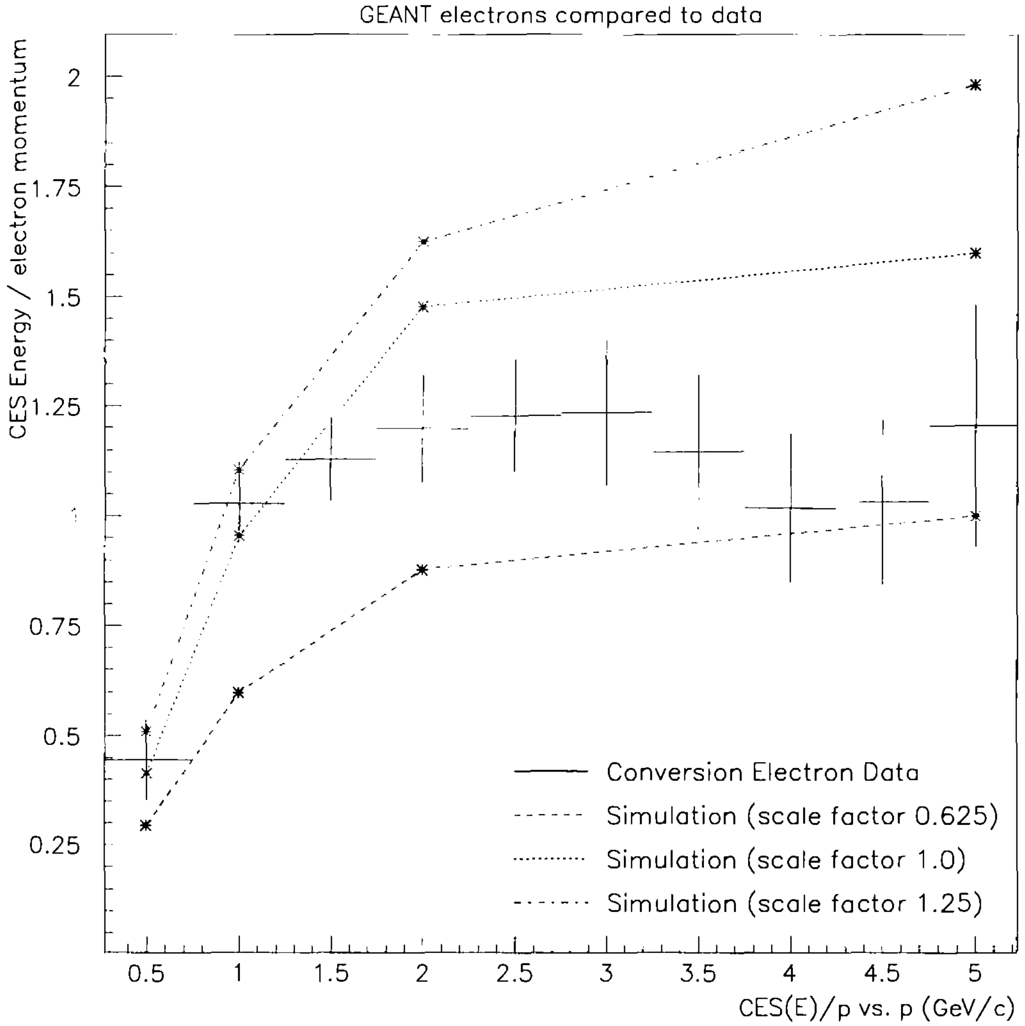

Figure 6.17: The average wire cluster energy: GEANT vs. data

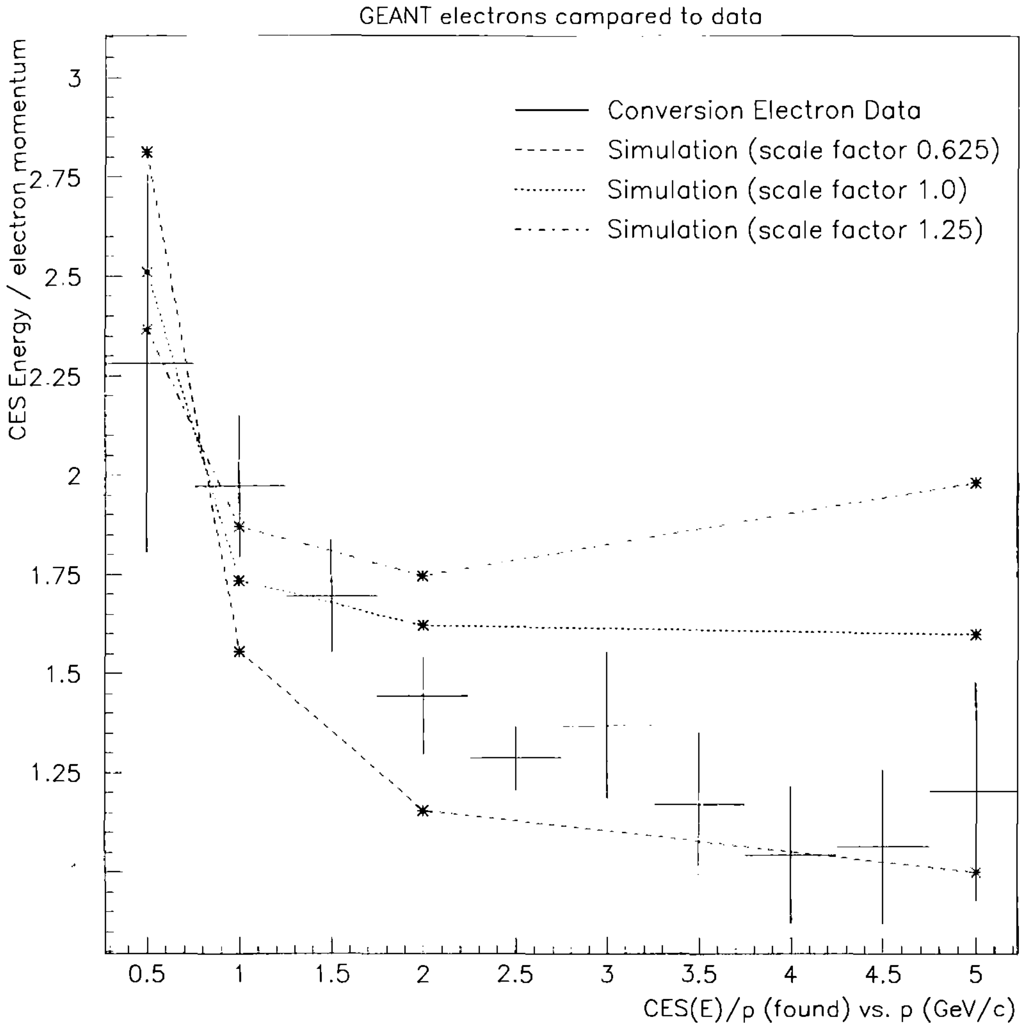

Figure 6.18: The average wire cluster energy for electrons with CES clusters

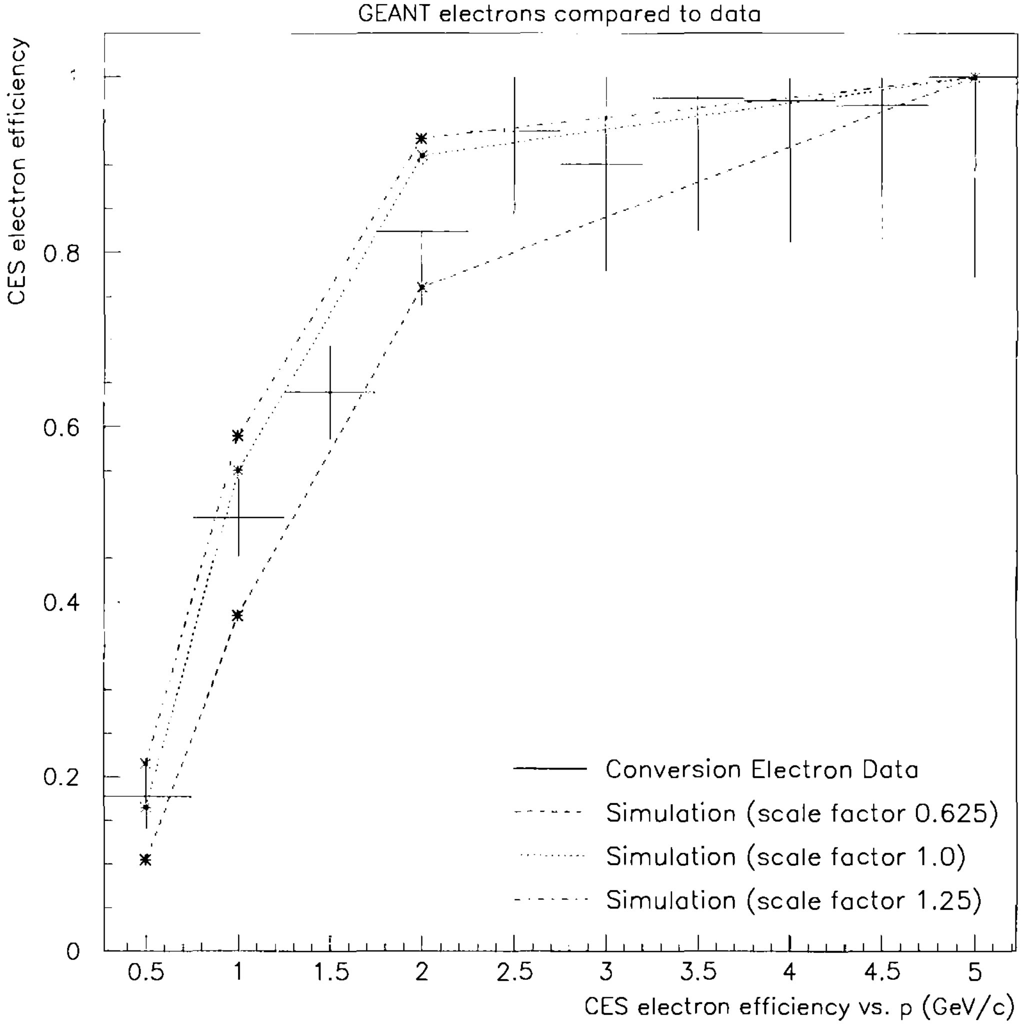

Figure 6.19: Comparison of CES efficiency for electrons: GEANT vs. data

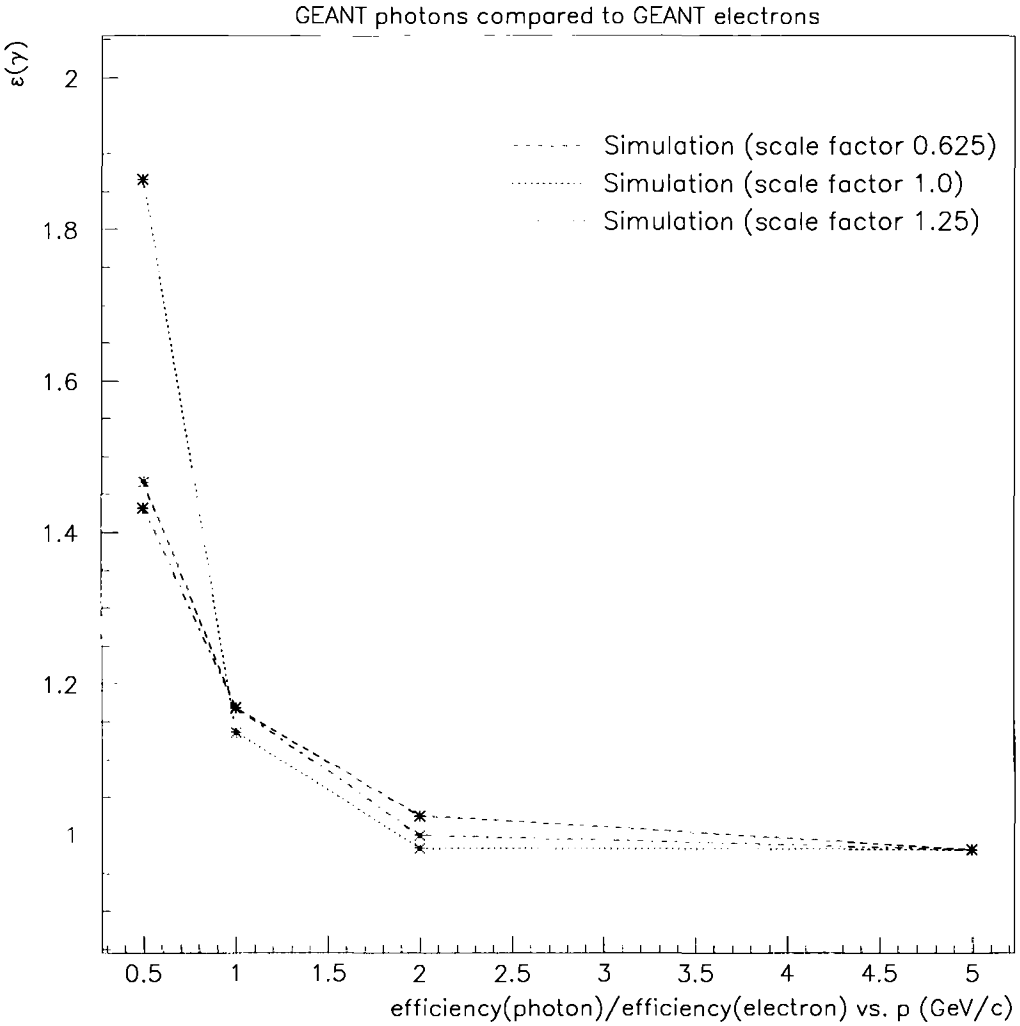

Figure 6.20: Comparison of CES efficiency: GEANT photons / GEANT electrons

6.7 Photon Efficiency and Uncertainties

The photon efficiency was calculated as the measured electron efficiency times the photon/electron efficiency ratio given by the detector simulation. This calculation was done as a function of momentum, and the efficiency obtained is shown in Figure 6.21. This efficiency curve was used in the Monte Carlo simulation for CEM and CES response to calculate the efficiency for reconstruction of $\chi_c \rightarrow J/\psi\gamma$. Since the simulated photon efficiency was less than 17% different from that for the simulated electron efficiency for all energies of interest, the uncertainty due to the response correction was chosen as half the largest change in efficiency, namely 9%. In addition, the uncertainty from the limited statistics of the electron sample contributed to the photon efficiency uncertainty, ranging from 9% for electron energy of 1.5 GeV to 16% for electron energies between 4 and 5 GeV. These effects are included in the uncertainty shown in the figure.

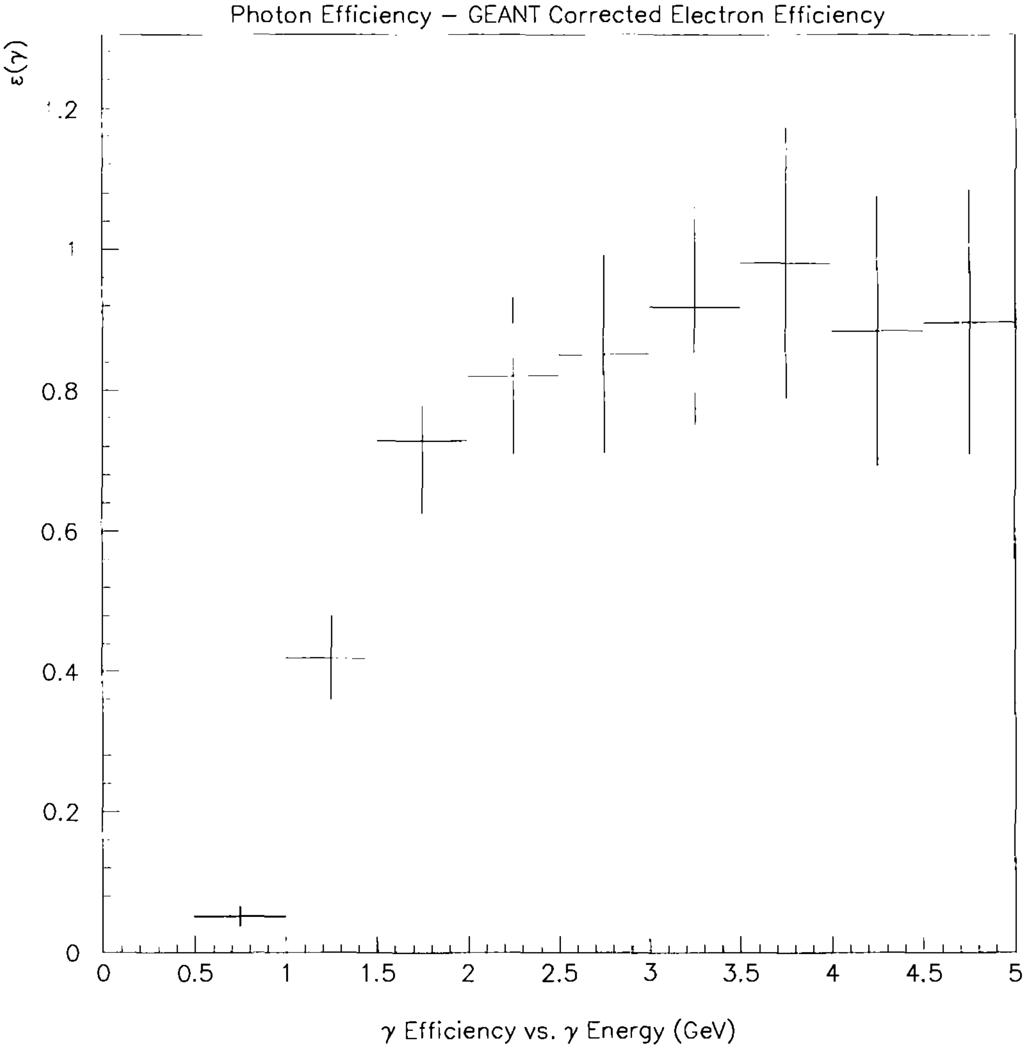

Figure 6.21: The photon finding efficiency

Chapter 7

Acceptance Determination

Calculating the detector acceptance for a given type of event can be an extremely difficult process. The actual detector geometry and response need to be applied to the kinematic distributions expected for the events. This can involve integrations which are extremely difficult to solve analytically. There are, however, ways of numerically evaluating complex integrals. One is a method involving random numbers, called the Monte Carlo method.

The Monte Carlo method generates simulated physics events randomly within the energy ranges allowed by a model of the physical process under investigation. These simulated events have the same momenta spectra, rapidity spectra, and other quantities as the model predicts for the actual process. The positions and energies can be used to determine the efficiency for the observation of the process in question. The application of the Monte Carlo method to the process $\chi_c \rightarrow J/\psi\gamma$ is discussed in this chapter.

The χ_c reconstruction efficiency can be factored into several terms: the geometric acceptance (a function of the muon and photon fiducial and kinematic cuts), the efficiency of the J/ψ selection requirements (which depends on the muon identification requirements, the muon trigger efficiency, and the J/ψ reconstruction efficiency), and the efficiency of the photon selection requirements. The simulation of the process and the determination of the acceptance is examined by the following method.

- Monte Carlo $\chi_c \rightarrow J/\psi\gamma$ events were generated for each production mechanism, providing different hypotheses for the χ_c p_T and η spectra. These Monte Carlo generators are outlined in Section 7.1.
- A detector simulation was applied to each generated sample, to find the acceptance times efficiency for reconstructing $\chi_c \rightarrow J/\psi\gamma$ from each initial hypothesis. The acceptance and efficiency will depend somewhat on the production hypothesis, as will be shown in Section 7.2.
- The question as to which set of production hypotheses for the Monte Carlo samples best simulated the actual is addressed in Section 7.3. This discussion will justify the central value for acceptance times efficiency which will be used to calculate the true number of events produced in the $\bar{p}p$ collisions.

7.1 Monte Carlo Generators

Two separate Monte Carlo programs generated the similated $\chi_c \rightarrow J/\psi\gamma$ for the efficiency studies. The first modelled direct χ_c production, while the second simulated B meson production and subsequent decay into χ_c states. Both of these are described in this section.

7.1.1 Direct χ_c Production

ISAJET: General Description

ISAJET is a Monte Carlo event generator for pp or $p\bar{p}$ interactions at the high energies [55] such as those produced at the Tevatron. It includes a perturbative QCD calculation of the parton level hard scattering process, leading order QCD initial and final state radiation, and some models for fragmentation of both the partons and the initial beams. The hard scattering processes available within the standard ISAJET program have not to date included quarkonia production, so a modification to the program to do this is described below.

ISACHI: Charmonia Generation

The modification of ISAJET for including the charmonia cross section calculation of Equation 2.4 was named ISACHI. It calculated the parton level cross sections for the process $gg \rightarrow \chi_c g$ for the angular momentum states J =0,1,2. These parton level cross sections were calculated from Equation 2.2 with the functional forms as outlined in Reference [18]. The cross sections were then multiplied by the branching ratio for the χ_c state to decay into $J/\psi\gamma$. These decays were the only ones allowed for χ_c mesons. This had the effect of properly scaling the relative number of $J/\psi\gamma$ from each angular momentum state.

The value of α_s was calculated with a number of different expressions for Q^2, to provide an estimate of the systematic uncertainty on the acceptance calculation due to the uncertainty in the scale. The central value was chosen from the Monte Carlo with the momentum transfer proportional to the transverse mass $Q^2 = (p_T^2 + m_\chi^2)/4$. For the purposes of p_T slope and acceptance determination, the constant had no effect. A stiffer spectrum (with more events in the higher p_T regions) was obtained from $Q^2 = m_\chi^2$. To examine softer spectra, one more function for Q^2, for which there was no physical basis except that it provided a steeply falling spectrum, were used to generate events as well. The funcional form for this was $Q^2 = (m_\chi^2 + p_T^3/m_\chi)/6$.

Resultant J/ψ and χ_c p_T Distributions

The kinematics for the simulated events with different forms for α_s are observably different. The χ_c p_T distributions from each Q^2 is shown in Figure 7.1. The J/ψ distributions from each are shown in Figure 7.2. In these Figures the difference in slope of the p_T spectrum from varying Q^2 is apparent. Simple exponentials do not fit well to the spectra, so a single number would not quantify the range, but the difference in the acceptance and overall efficiency for each is discussed in Section 7.2.

7.1.2 B Generation

To determine the efficiency for detecting χ_c mesons coming from B decay, a Monte Carlo program generated B mesons which decayed into charmonia [56], $B \rightarrow \chi_c X$. This program modelled b-quark production according to the Nason, Dawson, Ellis order-α_s^3 calculation [23] outlined in Section 2.2 providing the p_T and η spectrum of the b-quark.

B mesons were generated with the relative fractions outlined in Equation 2.7, which were

$$B^+(B^-) : B^\circ(\bar{B}^\circ) : B_s(\bar{B}_s) = 0.4 : 0.4 : 0.2 \tag{7.1}$$

while B_c mesons and b-baryons where ignored. A Peterson ϵ parameter of 0.006 was used, defined in Equation 2.6, along with a b-quark mass of 5.0 GeV/c^2.

The B mesons were then decayed into two body states containing χ_{c1} mesons. Since only $B \rightarrow \chi_{c1} X$ decays have been found [26], the other angular momentum states were not generated. The CLEO 90% upper confidence level limit on the $B \rightarrow \chi_{c2} X$ branching fraction is 0.4% [26], while the combined CLEO and ARGUS results for the branching

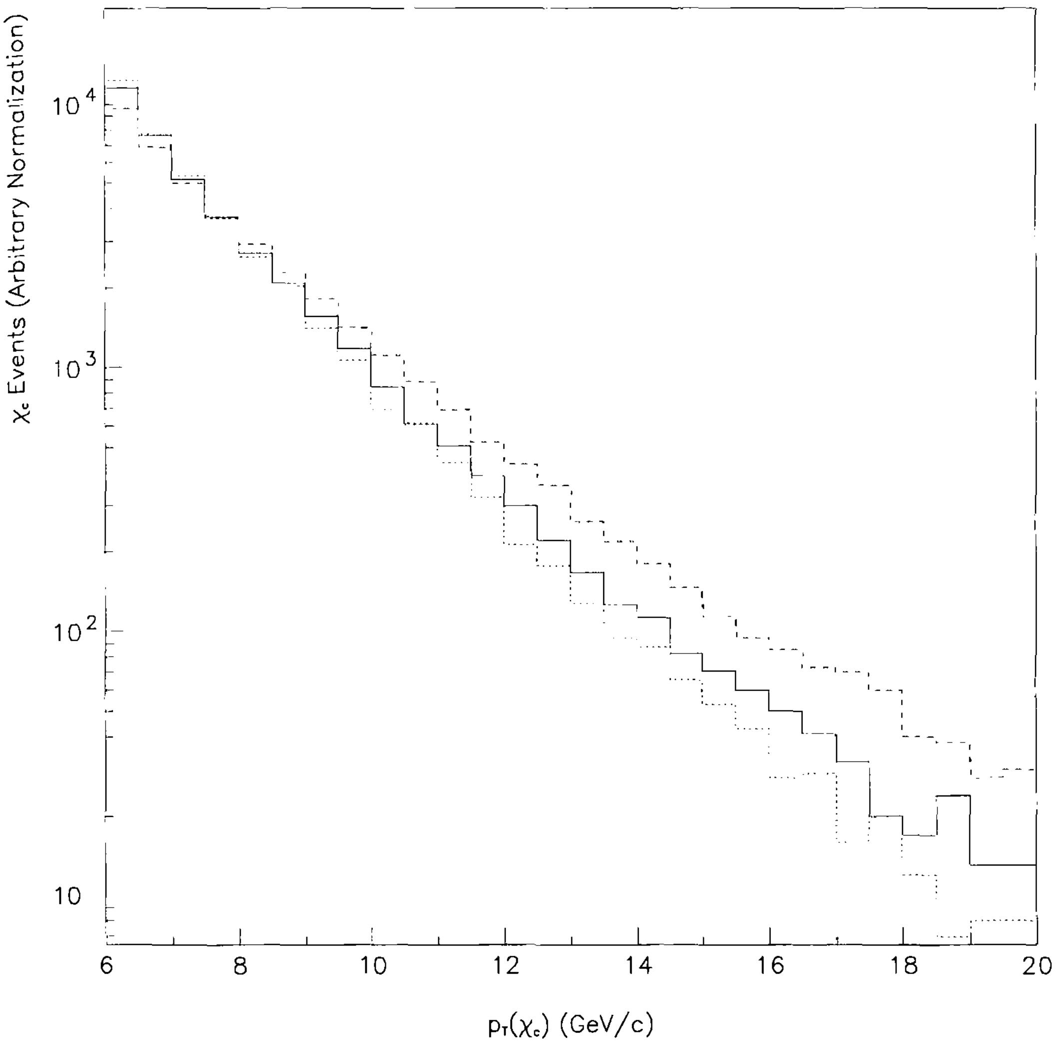

Figure 7.1: The $p_T(\chi_c)$ distributions for $Q^2 \propto m^2_{\chi_c} + p_T^2$ (solid), $Q^2 \propto m^2_{\chi_c}$ (dashed) and $Q^2 \propto n^2_{\chi_c} + p_T^3/m_{\chi_c}$ (dotted).

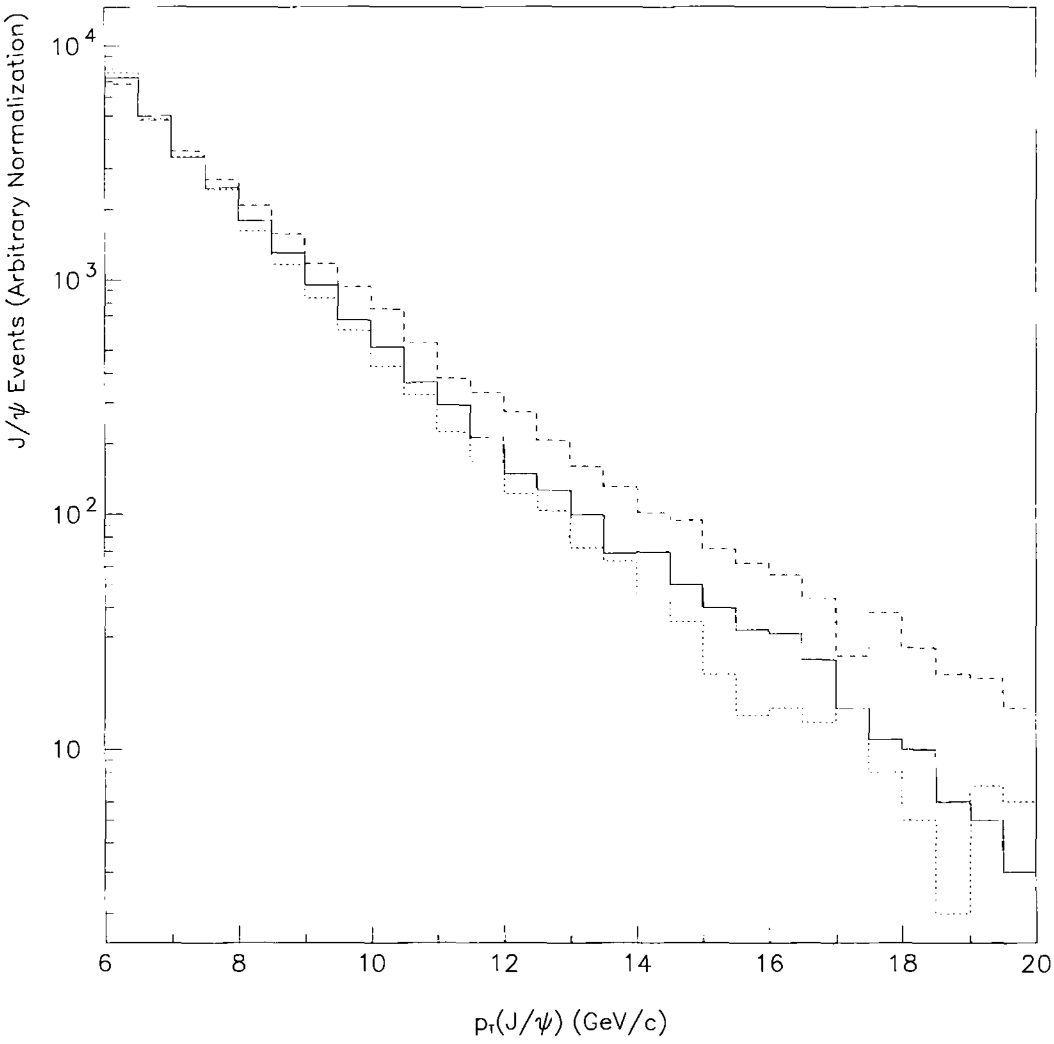

Figure 7.2: The $p_T(J/\psi)$ distributions for $Q^2 \propto m_{\chi_c}^2 + p_T^2$ (solid), $Q^2 \propto m_{\chi_c}^2$ (dashed) and $Q^2 \propto m_{\chi_c}^2 + p_T^3/m_{\chi_c}$ (dotted).

fraction for $B \rightarrow \chi_{c1}X$ is $(0.64 \pm 0.20)\%$ [26], so the assumption of no χ_{c2} mesons is a good one. The branching fraction for $\chi_{c0} \rightarrow J/\psi\gamma$ is less than 3% times that for $\chi_{c1} \rightarrow J/\psi\gamma$ [4], so χ_{c0} decays of B mesons were also negligible. The decays allowed were $B^+ \rightarrow \chi_{c1}K^+$, $B^\circ \rightarrow \chi_{c1}K^{\circ *}$, $B_s \rightarrow \chi_{c1}\phi$, $\chi_{c1} \rightarrow J/\psi\gamma$, $J/\psi \rightarrow \mu^+\mu^-$, $\phi \rightarrow K^+K^-$, $K^{\circ *} \rightarrow K^+\pi^-$, and charge conjugate modes. There was no reason to expect only two body decays, and many body decays would yield a slightly softer $p_T(\chi_c)$ spectrum, but the other uncertainties in the efficiency calculation (shown in section 7.3 to be 33% of the size of the overall efficiency) are much larger than this effect, and it can be neglected.

J/ψ p_T Distributions

The χ_c produced from b-hadron decays have larger transverse momenta than do directly produced χ_c. This means that the J/ψ distribution is stiffer as well (see Figure 7.3). The higher momenta of these mesons will translate into a higher efficiency for detecting charmonia from b-hadron decay (see Section 7.2).

7.2 Detector Model

A simple detector model was used for the study of acceptances. This model used only the μ^+, μ^- and γ particle four-vectors from the Monte Carlo programs described above. Since the acceptance was defined by requiring the muons and photon to pass only certain geometric and kinematic requirements, it was not necessary to use a complete detector simulation. The individual muon and photon selection efficiencies (which did not include kinematic and geometric acceptances) were determined from the data and were discussed in Chapters 4, 5, and 6.

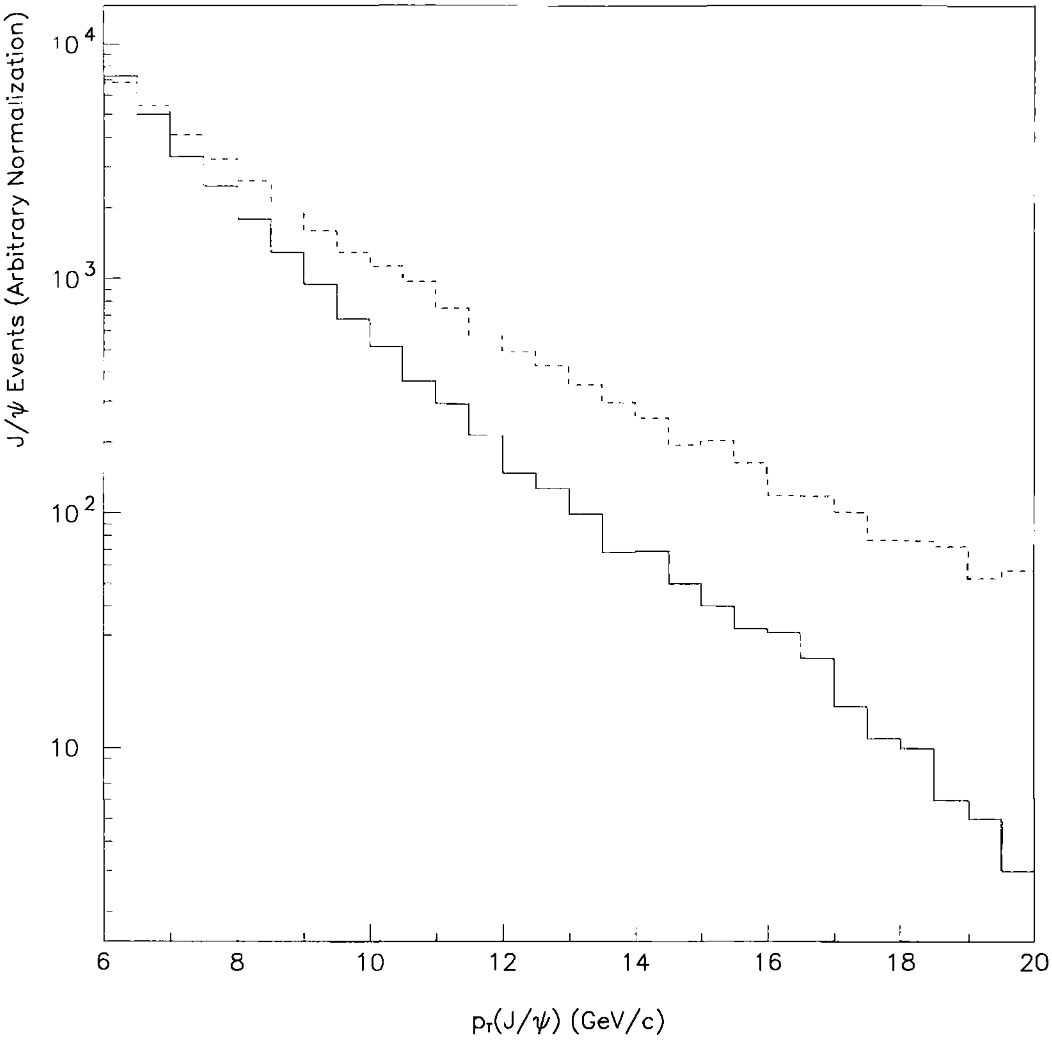

Figure 7.3: The $p_T(J/\psi)$ distributions for direct production (solid) and B decay (dashed).

7.2.1 Muon Geometry Simulation

In the model, an event vertex along z was chosen from a Gaussian distribution with $\sigma = 35$ cm. The decay muons were propagated through the magnetic field and calorimeters (including any return field) to the muon chambers. Fiducial cuts matched the Central Muon Detector geometry described in Chapter 3. The kinematic and fiducial cuts were applied in the same way as done for the muons in the data:

- each muon was in the CMU
- each muon had $p_T > 3.0$ GeV/c
- muons were not allowed to fall in the same or adjacent muon wedges (as defined in Chapter 4).

The dimuon acceptance with these requirements is shown as a function of $\eta(J/\psi)$ in Figure 7.4, for generated $\chi_c \rightarrow J/\psi$ events with $p_T(J/\psi) > 6.0$ GeV/c. The acceptance falls off dramatically at larger $|\eta|$ because the muon chambers covered a limited rapidity range. Since the efficiency is so low above $|\eta| = 0.5$, the requirement

- $|\eta(J/\psi)| < 0.5$

defined the kinematic region of interest for all events decaying to $J/\psi \rightarrow \mu^+\mu^-$ final states. To minimize the uncertainties due to extrapolation to higher rapidity, the requirement also defined the region of interest for this analysis. All subsequent calculations will make this requirement both on the data and the Monte Carlo simulated events.

The acceptance depended on the transverse momentum of the J/ψ meson. Figure 7.5 shows the acceptance as a function of $p_T(J/\psi)$. The muon p_T requirement for both muons resulted in a very low acceptance for the lower values of J/ψ transverse momentum. This motivated the cut of

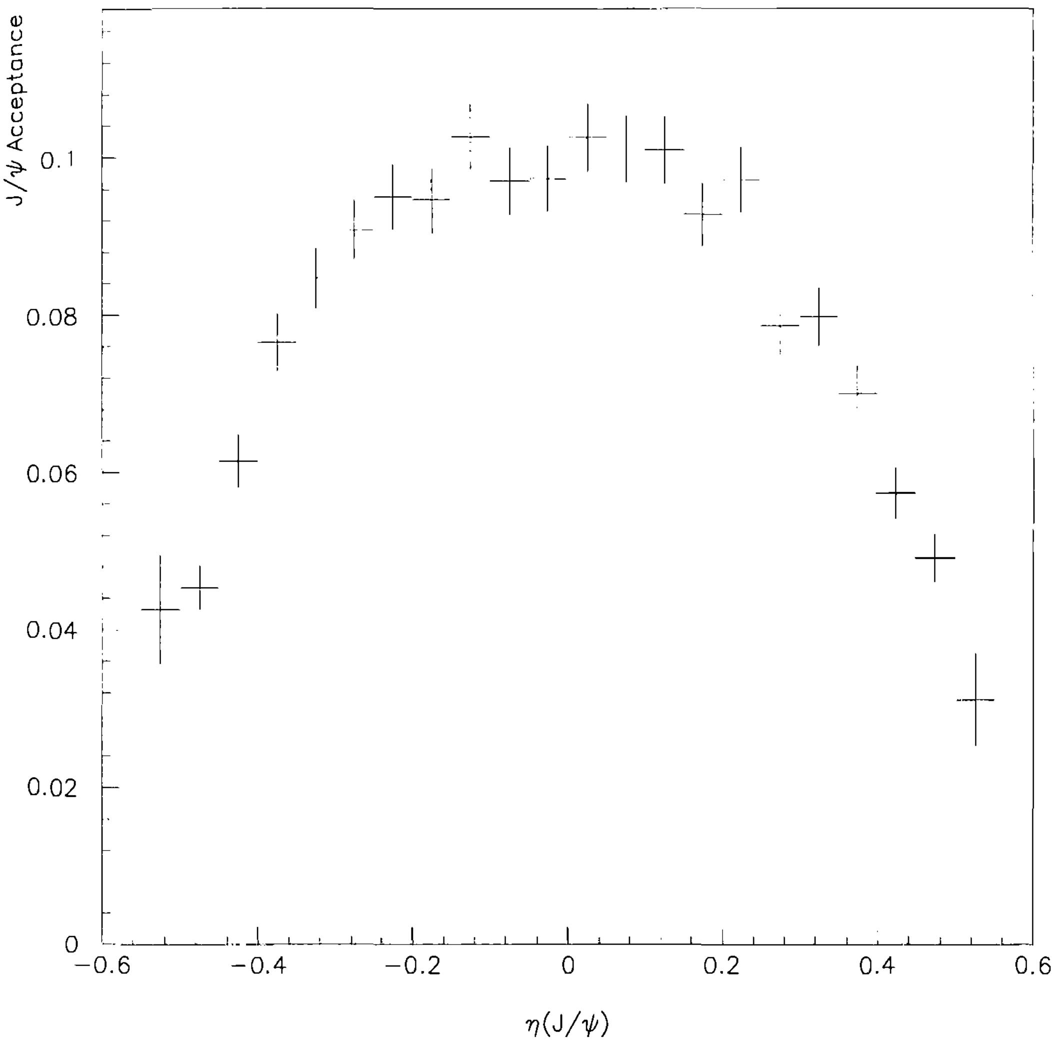

Figure 7.4: The J/ψ acceptance as a function of $\eta(J/\psi)$ for $p_T(J/\psi) > 6.0$ GeV/c.

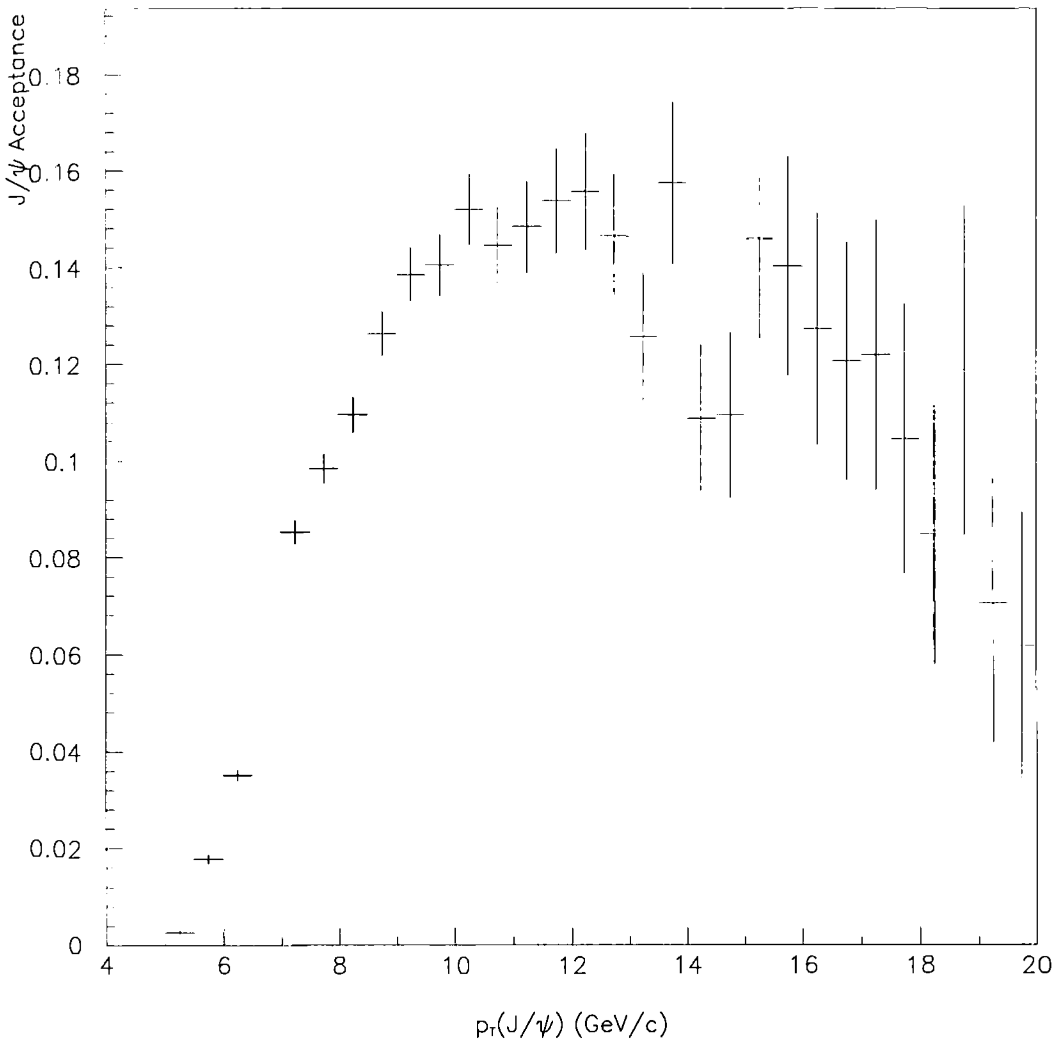

Figure 7.5: The J/ψ acceptance as a function of $p_T(J/\psi)$ for $|\eta(J/\psi)| < 0.5$.

Process		Acceptance
$B \rightarrow \chi_c X$		$(9.27 \pm 0.17)\%$
Direct χ_c	$Q^2 = m_\chi^2$	$(8.83 \pm 0.18)\%$
	$Q^2 \propto m_\chi^2 + p_T^2$	$(7.74 \pm 0.11)\%$
	$Q^2 \propto m_\chi^2 + p_T^3/m_\chi$	$(7.48 \pm 0.18)\%$

Table 7.1: The geometric and kinematic acceptance in the region $p_T(J/\psi) > 6.0$ GeV/c and $|\eta(J/\psi)| < 0.5$ for various simulated $\chi_c \rightarrow J/\psi\gamma$ event samples.

- $p_T(J/\psi) > 6.0$ GeV/c

which defined the region of interest for J/ψ production at CDF. All calculations will make this requirement for both the data and simulated events. All conclusions and simulations will be quoted for the kinematic range $p_T(J/\psi) > 6.0$ GeV/c and $|\eta(J/\psi)| < 0.5$. The efficiency also began to fall off at higher values of $p_T(J/\psi)$ since very energetic J/ψ mesons were more likely to have the μ^+ and μ^- fall into adjacent muon wedges.

Since the acceptance is p_T dependent, J/ψ production mechanisms with different p_T spectra had different acceptances. The acceptances, defined by all the above cuts for each of the simulated χ_c samples are summarized in Table 7.1. The uncertainties arise from Monte Carlo statistics.

7.2.2 Muon Trigger Simulation

To simulate the trigger efficiency more fully, a paramaterization of the level one trigger was used which relied on an understanding of the effects of multiple scattering on the muons traversing the detector (see Chapter 8). To do this, the muons were assigned a track stub slope in the CMU region depending on the p_T. As discussed for the real data in Chapter 4, the slope was modelled as a random gaussian with a mean [57]

$$\alpha_0 = \frac{0.126}{p_T} \tag{7.2}$$

and deviation σ_α. The magnitude of the slope deviation (as determined by multiple scattering, energy loss, and measurement error) was given by

$$\sigma_\alpha^2 = (\frac{0.131}{p_T})^2 \frac{0.27 + 0.73/\sin\theta}{1 - 1.43/p_T} + (0.0062)^2. \tag{7.3}$$

If the absolute value of this slope was greater than or equal to the cutoff slope $\alpha_c = 0.086$ [57], the Monte Carlo muon trigger failed.

Another random number was generated with a flat distribution between 0 and 1 to model the plateau of the Level 1 efficiency, and if it was greater than or equal to 0.918 [57] the Monte Carlo trigger failed as well. The Level 1 trigger efficiency resulting from this simulation is shown in Figure 7.6. This compares favorably with the measured efficiency, as shown in Figure 7.7 where both the measured Level 1 trigger efficiency and the muon Level 1 trigger simulation are displayed. The decrease in efficiency at the lower muon p_T motivated the $p_T > 3.0$ GeV/c cut as discussed in Chapter 4. In the same way, a CFT efficiency of 99 % was simulated for both legs to model the CFT component of the Level 2 efficiency. The dimuon trigger simulation led to an event which either passed or failed the trigger. The events were required to

- pass the dimuon trigger.

7.2.3 J/ψ Selection Requirements

To model the J/ψ mass resolution, the muon momenta and directions were smeared by the uncertainties for momenta and direction of tracks found in the CTC for beam-constrained tracks. The magnitudes of these resolutions are given in Section 5.2. The reconstructed

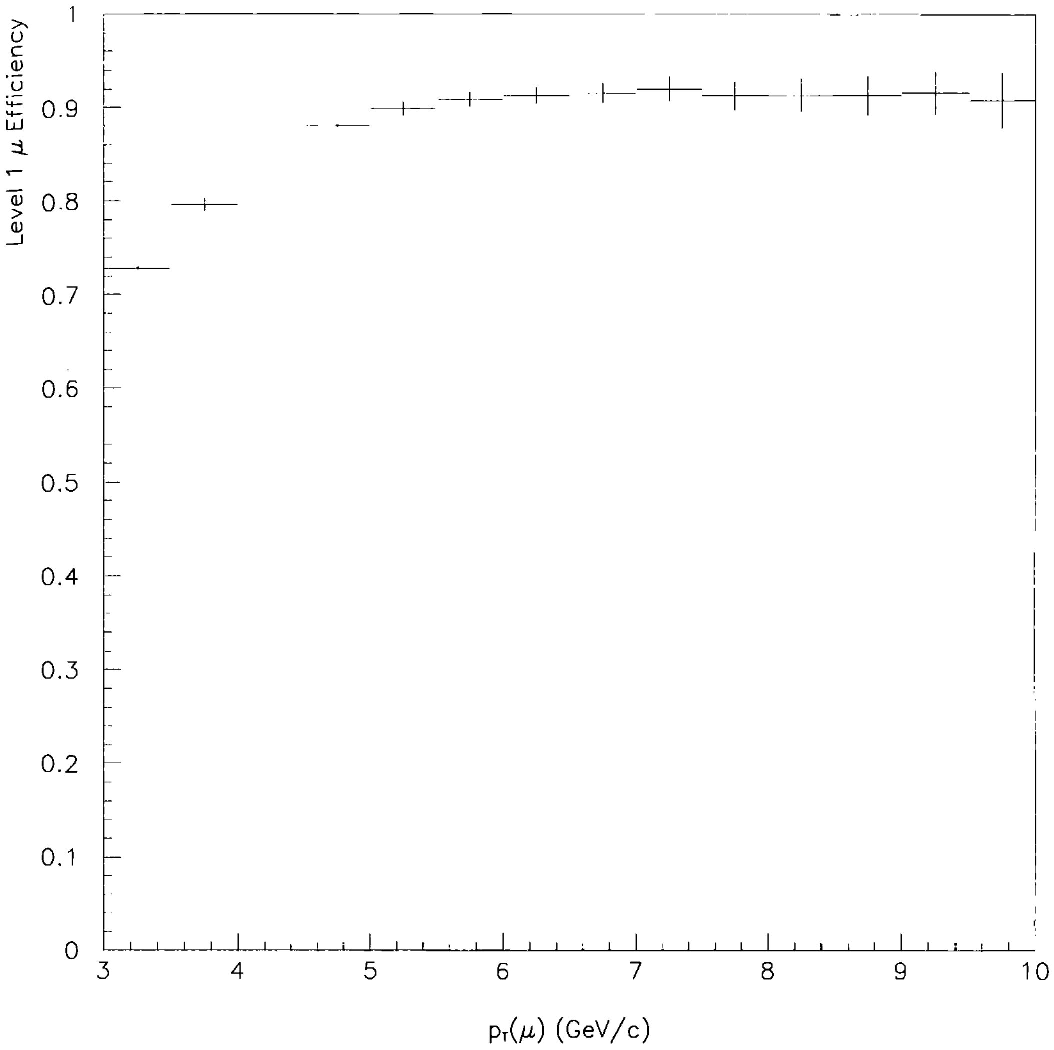

Figure 7.6: The simulated Level 1 muon trigger efficiency as a function of muon p_T.

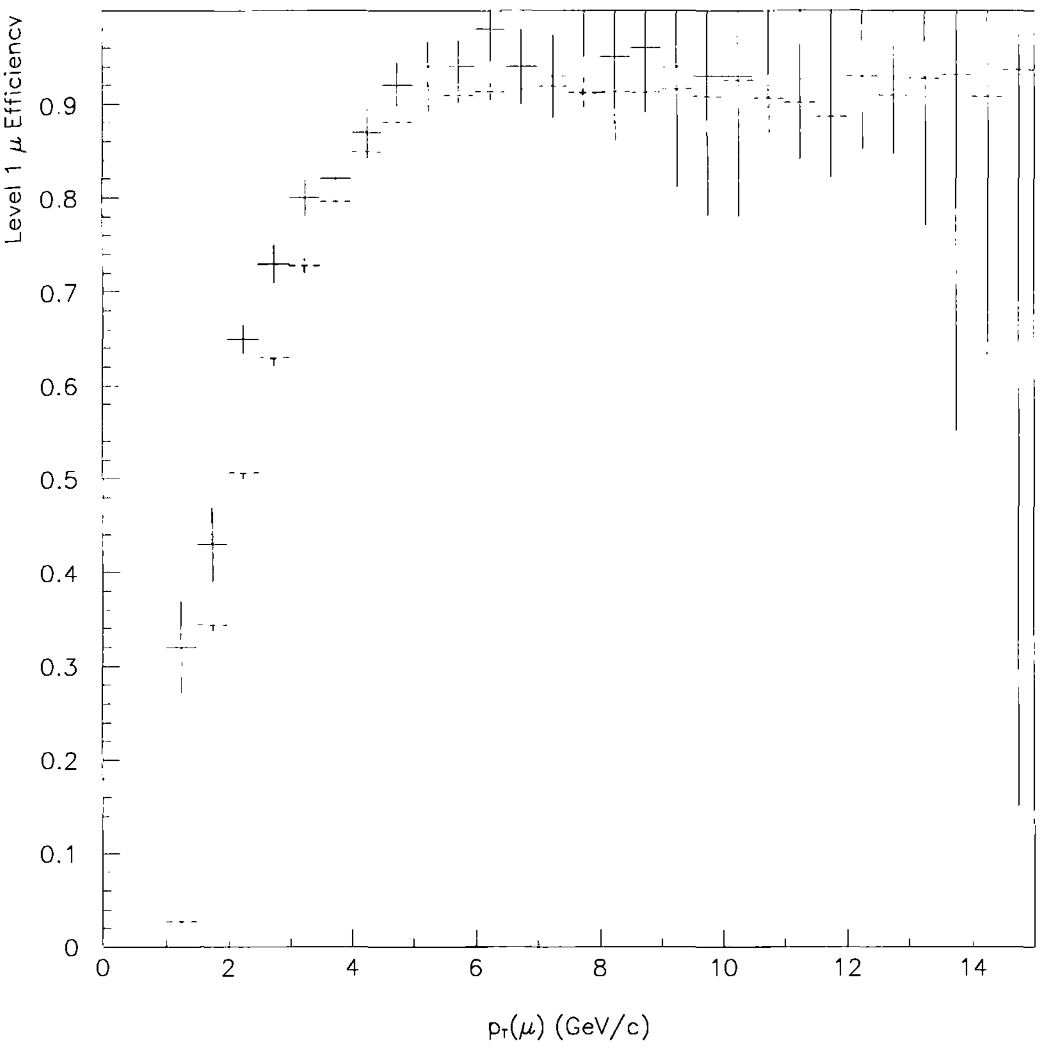

Figure 7.7: The level 1 muon trigger efficiency, comparing the measuremed efficiency (solid) with the simulation (dashed).

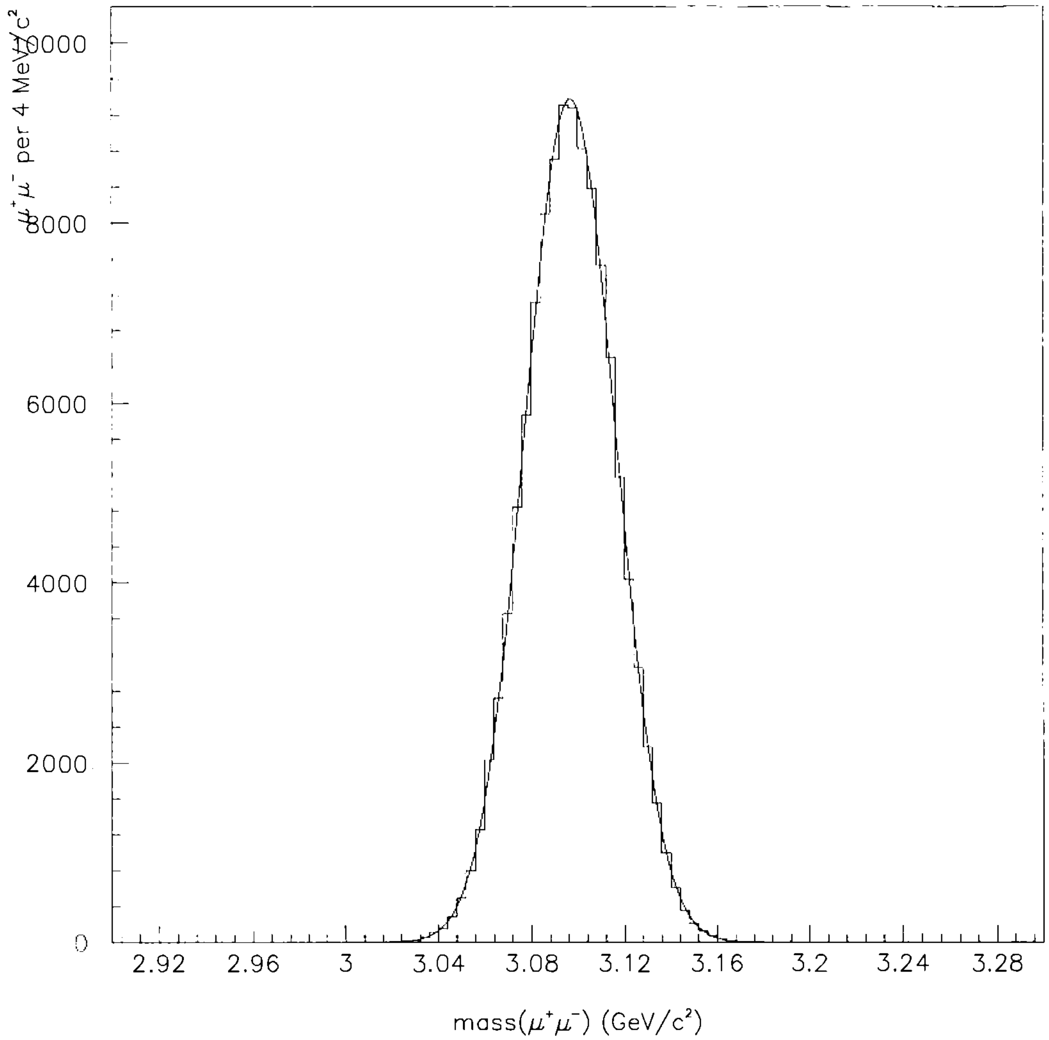

Figure 7.8: The simulated dimuon mass.

Process		$\epsilon(J/\psi)(\%)$
$B \to \chi_c X$		5.10 ± 0.20
Direct χ_c	$Q^2 = m_\chi^2$	4.72 ± 0.20
	$Q^2 \propto m_\chi^2 + p_T^2$	4.02 ± 0.15
	$Q^2 \propto m_\chi^2 + p_T^3/m_\chi$	3.91 ± 0.17

Table 7.2: The acceptance times efficiency in the region $p_T(J/\psi) > 6.0$ GeV/c and $|\eta(J/\psi)| < 0.5$ for various simulated $\chi_c \to J/\psi\gamma$ event samples.

mass distribution is shown in Figure 7.8. This was fit to a Gaussian, and a resolution of 19 MeV/c^2 was observed. A dimuon mass cut to weed out non-J/ψ dimuon candidates of

- $3.05 < M(\mu^+\mu^-) < 3.15$ GeV/c^2

was measured to be (97 ± 2)% efficient for retaining real J/ψ events.

When the acceptance was calculated, there were a few more effects which had to be taken into account. The 3 σ matching cuts between muon stub position in the CMU and extrapolated CTC position were determined from the Gaussian nature of the distributions (97 ± 1)% efficient, where the uncertainty arises from uncertainties in the parameters of the Gaussian. Another effect was the loss of one muon wedge (Number **17E**) during the run which lost $\frac{2}{48}$ of the dimuon data. Also, the CTC track reconstruction for the two muons was (97 ± 2)% efficient if the muons had passed all the other cuts. Finally, the muon reconstruction probability for two muons was (98 ± 1)%.

The acceptance times efficiency, $\epsilon(J/\psi)$, for J/ψ mesons passing all the above requirements is summarized in Table 7.2. The uncertainties are Monte Carlo statistics in quadrature with the other uncertainties listed above.

7.2.4 Photon Geometry Simulation

The photon geometry cuts were simulated as well. The photon geometry simulation began with the same generated event vertex as the muon geometry simulation. From this and the photon momentum given by the Monte Carlo generator, the photon shower position in the CES was calculated. The fiducial requirements were the same as for the χ_c reconstruction:

- The photon hit at least 9 cm in z from the joining of the two η halves of the calorimeter at 90° from the beamline
- The photon hit within 21 cm from the center of a CEM tower in the $r - \phi$ direction to avoid the cracks between wedges
- The photon hit in the most central region of the CEM, $55^\circ <$ detector $\theta < 125^\circ$
- The photon did not fall into the same calorimeter tower as either muon

7.2.5 Photon Efficiency Simulation

The photon energy spectrum for events passing all J/ψ and photon geometry requirements was different for each Monte Carlo sample. Because the photon efficiency is also energy dependent, the difference in photon energy spectra of these samples implies that the integrated average photon efficiency will be different for each sample. It should be noted that the J/ψ selection requirements, which preferentially select higher p_T J/ψ mesons, and therefore higher p_T χ_c mesons, will bias the average photon energy to a higher value than for events without the J/ψ cuts. This is why the total efficiency is determined for each process separately, taking into account the correlations between all the generated decay products.

The photon efficiency was simulated using the efficiency curve for the photon (shown in Figure 6.21). Each event was weighted by the value of the efficiency for the energy bin the photon fell into. The weight was zero if the photon failed the geometry requirements listed above. The weights were summed for events passing all the J/ψ requirements, and the average efficiency was just this sum divided by the number of events. Thus, the photon acceptance times efficiency, $\epsilon(\gamma)$, was determined by the equation

$$\epsilon(\gamma) = \frac{\sum_{i=1}^{N(J/\psi)} w(E_\gamma)}{N(J/\psi)} \tag{7.4}$$

where $w(E_\gamma)$ is the efficiency weight which depends upon the energy and position of the photon and $N(J/\psi)$ is the number of events passing all the J/ψ requirements. The product of $\epsilon(\gamma)$ and $\epsilon(J/\psi)$ was the total χ_c acceptance times efficiency ϵ. This was a simple product since the J/ψ requirements were made first (both in the Monte Carlo and the data) and then the photon requirements were made after the J/ψ had already been reconstructed. The values for $\epsilon(\gamma)$ and ϵ for the different Monte Carlo runs are summarized in Table 7.3, along with the relative fractions of each χ_c state reconstructed. The importance of determining different values of ϵ for the various assumptions for Q^2 was primarily to show that the central value obtained for direct production (ϵ calculated with $Q^2 \propto m_\chi^2 + p_T^2$) was not close to a non-linear dropoff of efficiency that a slightly different p_T spectrum would experience. The relatively linear progression of ϵ with the exponent on p_T shows that such a non-linear dropoff does not exist near the kinematic region generated. An estimate of the magnitude of the uncertainty in ϵ arising from uncertainties in the underlying χ_c p_T distribution will be found in Section 7.3.

7.2.6 χ_c Polarization

The unknown polarization of the χ_c mesons introduced another uncertainty in the acceptance calculation. If the angle of the γ momentum direction, boosted into the χ_c rest frame with respect to the χ_c momentum direction was θ^*, the similar angle for the J/ψ was $-\theta^*$.

Process		$\epsilon(\gamma)$ (%)	ϵ (%)
$B \to \chi_c X$		22.2 ± 3.6	1.15 ± 0.23
Direct χ_c	$Q^2 = m_\chi^2$	18.3 ± 2.3	0.91 ± 0.15
	$Q^2 \propto m_\chi^2 + p_T^2$	17.3 ± 2.3	0.72 ± 0.15
	$Q^2 \propto m_\chi^2 + p_T^3/m_\chi$	15.0 ± 2.3	0.62 ± 0.15

Table 7.3: The photon efficiency, $\epsilon(\gamma)$, and the full χ_c reconstruction efficiency, ϵ, in the region $p_T(J/\psi) > 6.0$ GeV/c and $|\eta(J/\psi)| < 0.5$ for various simulated $\chi_c \to J/\psi\gamma$ event samples.

The decay distribution in $\cos\theta^*$ could be described as proportional to $1+\alpha(\cos\theta^*)^2$. Here α is the measure of χ_c polarization. The photon selection, including the 1 GeV energy requirement, sculpts the reconstructed distribution since it is more efficient where the photon is along the χ_c momentum axis ($\cos\theta^* = +1$), while photons pointing backwards are less likely to have the required energy and the efficiency is less where $\cos\theta^* = -1$. The uncertainty was determined by varying the χ_c polarization between $\alpha = -1$ and $\alpha = +1$. Although the J/ψ efficiency was only affected by 3%, the total χ_c reconstruction efficiency varied by 11%. This uncertainty was added in quadrature to the uncertainty of the final result.

7.2.7 χ_c Mass Resolution

To model the χ_c mass resolution, the photon energy and position in the calorimeter were smeared by the uncertainties (measured in Chapter 6) for the quantities given by $\frac{\sigma(E)}{E} = \frac{18\%}{\sqrt{E_T}}$, $\sigma(r\phi) = 0.8$ cm and $\sigma(z) = 1.0$ cm. The J/ψ mass was smeared as in Section 7.2.3. All of the χ_c reconstruction requirements were applied, including event weighting defined for the photon efficiency simulation. The mass was fit to a Gaussian, and the mass resolution was 66 MeV/c^2 (for the sample with $Q^2 \propto m_\chi^2 + p_T^2$) as shown in Figure 7.9. For comparison, the unsmeared masses are also displayed in the hatched bins. The mass difference ΔM = mass(χ_c)-mass(J/ψ) is shown in Figure 7.10, also compared to the unsmeared ΔM in the hatched bins. A Gaussian fit to the peak yielded a resolution of 62 MeV/c^2, somewhat smaller than the resolution for the full mass since the part of the uncertainty due to the J/ψ resolution is common to both the $\mu^+\mu^-\gamma$ mass and the $\mu^+\mu^-$ mass. The other Monte Carlo samples provided similar resolutions.

7.3 Acceptance Results

The J/ψ acceptance times efficiency for J/ψ mesons arising from direct production was taken as $\epsilon(J/\psi)$ for the Monte Carlo sample generated with $Q^2 \propto m_\chi^2 + p_T^2$, determined in the last Section as $(4.19 \pm 0.16)\%$. An additional uncertainty due to the uncertainty of the p_T spectrum was taken as the range of values determined from the samples with the different Q^2 expressions, a range of ±19% of the central value for $\epsilon(J/\psi)$. Thus direct χ_c production led to a J/ψ reconstruction efficiency of $\epsilon(J/\psi)$(direct)= $(4.19 \pm 0.81)\%$. Similarly, the χ_c reconstruction efficiency for direct χ_c production was taken as ϵ for the process with $Q^2 \propto m_\chi^2 + p_T^2$. As previously, the additional uncertainty due to the uncertainty of the underlying momentum spectrum was the range of values, ±25% of the value for ϵ, 19% of which was due to the variation in $\epsilon(J/\psi)$, and 6% of which was due to the variation in $\epsilon(\gamma)$. Since the momenta of the J/ψ and γ were correlated, these were added directly and not in quadrature. The reconstruction efficiency for directly produced χ_c mesons was determined to be ϵ(direct)= $(0.72 \pm 0.24)\%$.

The acceptance depended on the relative amount that each production process contributed to the total cross section. Figure 7.11 shows the reconstruction efficiency the

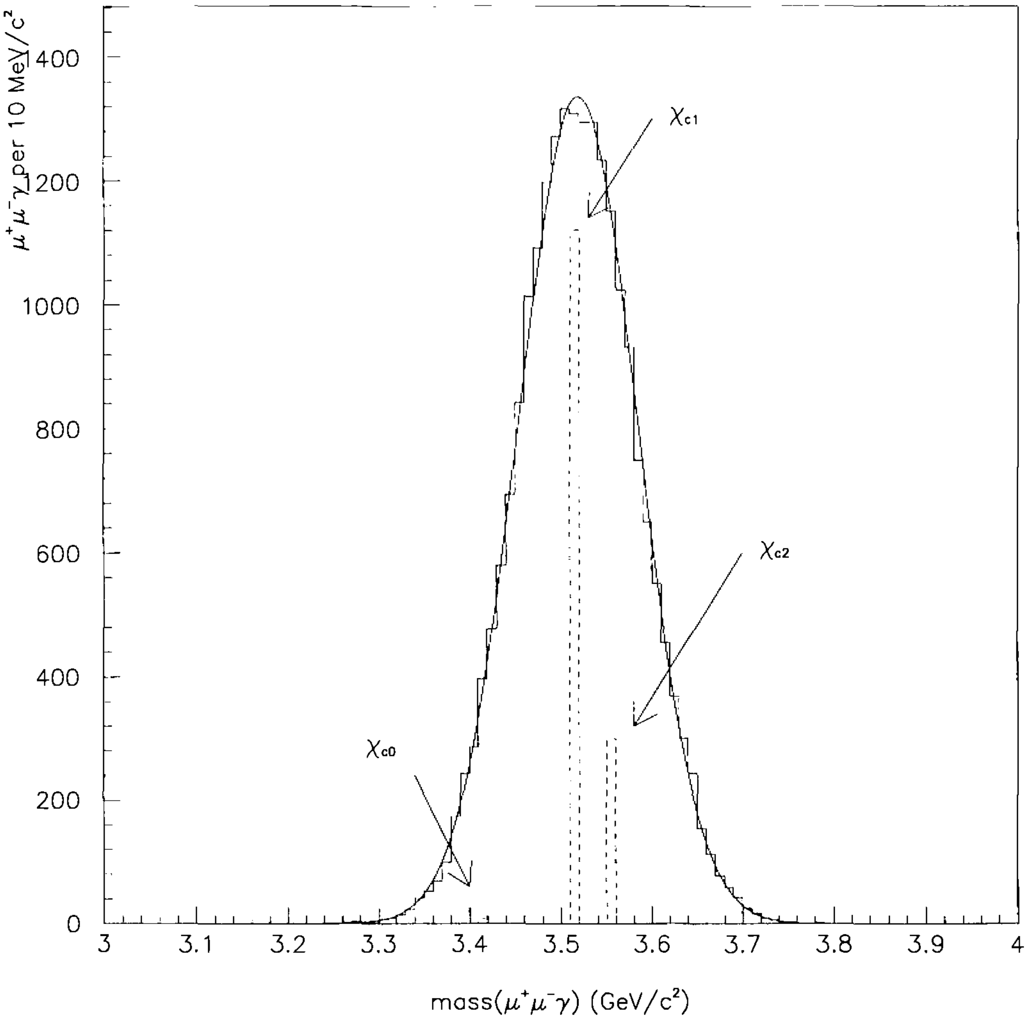

Figure 7.9: The simulated $\mu^+\mu^-\gamma$ mass.

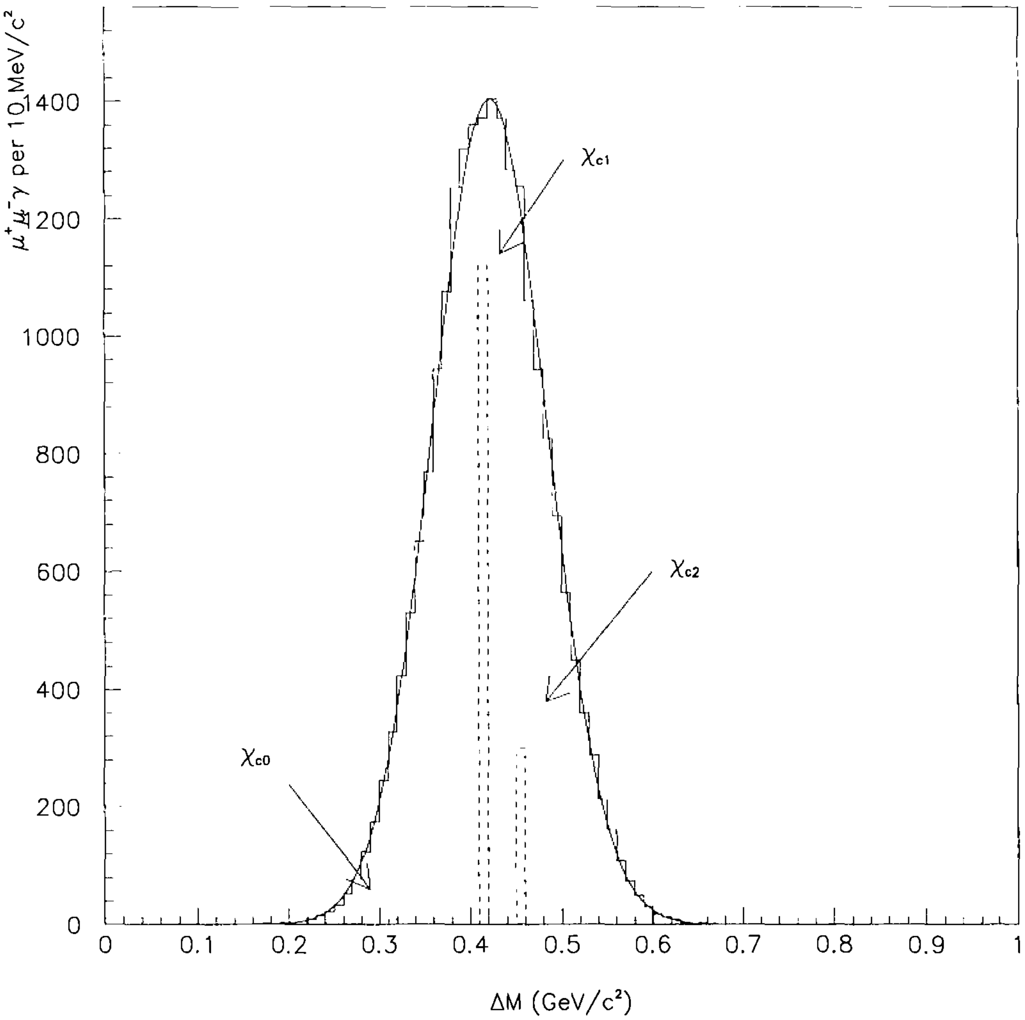

Figure 7.10: The simulated ΔM distribution.

model assigns to χ_c mesons as a function of the relative fraction of the cross section arising from B decays, f_b. An assumption of 37% direct $\chi_c \to J/\psi\gamma$ to 63% J/ψ produced from B decay (checked in Chapter 9) would yield a J/ψ efficiency of (4.80 + 0.36 - 0.57)%. This fraction for the two production methods is shown to be a relatively good assumption by the fact that the value obtained for the efficiency using the J/ψ p_T data itself was (4.99 + 0.37 - 0.59)%. Another way of seeing this is by comparing the resultant Monte Carlo J/ψ p_T

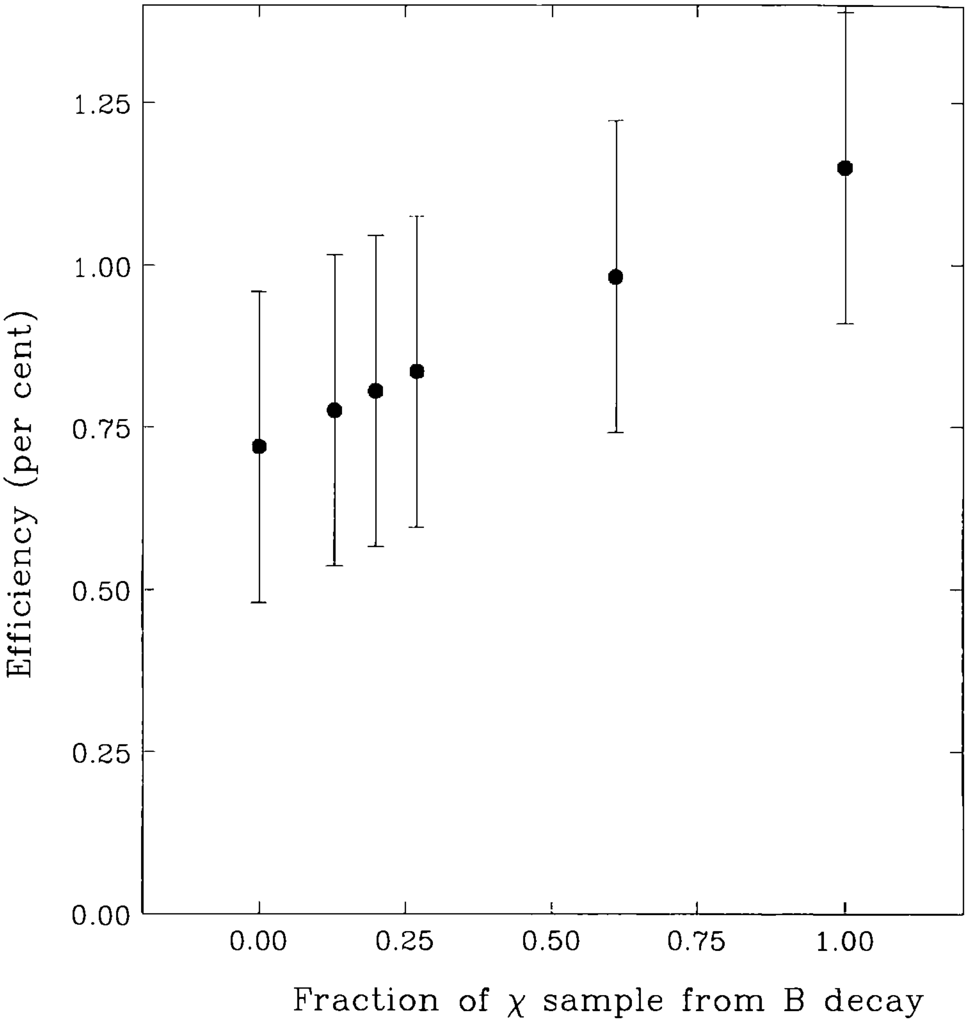

Figure 7.11: The Monte Carlo efficiency for χ_c reconstruction as a function of the relative fraction of the cross section which comes from B decays.

Cause	Uncertainty (fractional)
J/ψ reconstruction	10%
γ identification	16%
χ_c p_T and η distributions (including production mechanisms)	25%
χ_c polarization	11%
total $\epsilon(\chi_c)$	33%

Table 7.4: Summary of uncertainties in the calculation of the total χ_c efficiency.

distribution to data (see Figure 7.12).

Because the branching ratio for $B \longrightarrow \chi_{c1}X \longrightarrow J/\psi\gamma X$ accounts for $(15 \pm 5)\%$ of the total $B \longrightarrow J/\psi X$ branching ratio (from Equation 2.8), the above assumption on the ratio of direct $\chi_c \longrightarrow J/\psi\gamma$ to J/ψ from b-hadron decay translates into an assumption of a ratio of directly produced χ_c mesons to χ_c mesons arising from B decay of $(0.37) : (0.63)(.15 \pm .05) = 0.37 : (0.095 \pm 0.032) = 0.80 : (0.20 \pm 0.07)$. Assuming the ratio of direct χ_c production to χ_c from B decay is 0.80 ± 0.41 we obtain a total combined χ_c reconstruction efficiency of $(0.79 \pm 0.26)\%$. The uncertainties are summarized in Table 7.4. This is the value used to determine the χ_c cross section in Chapter 9.

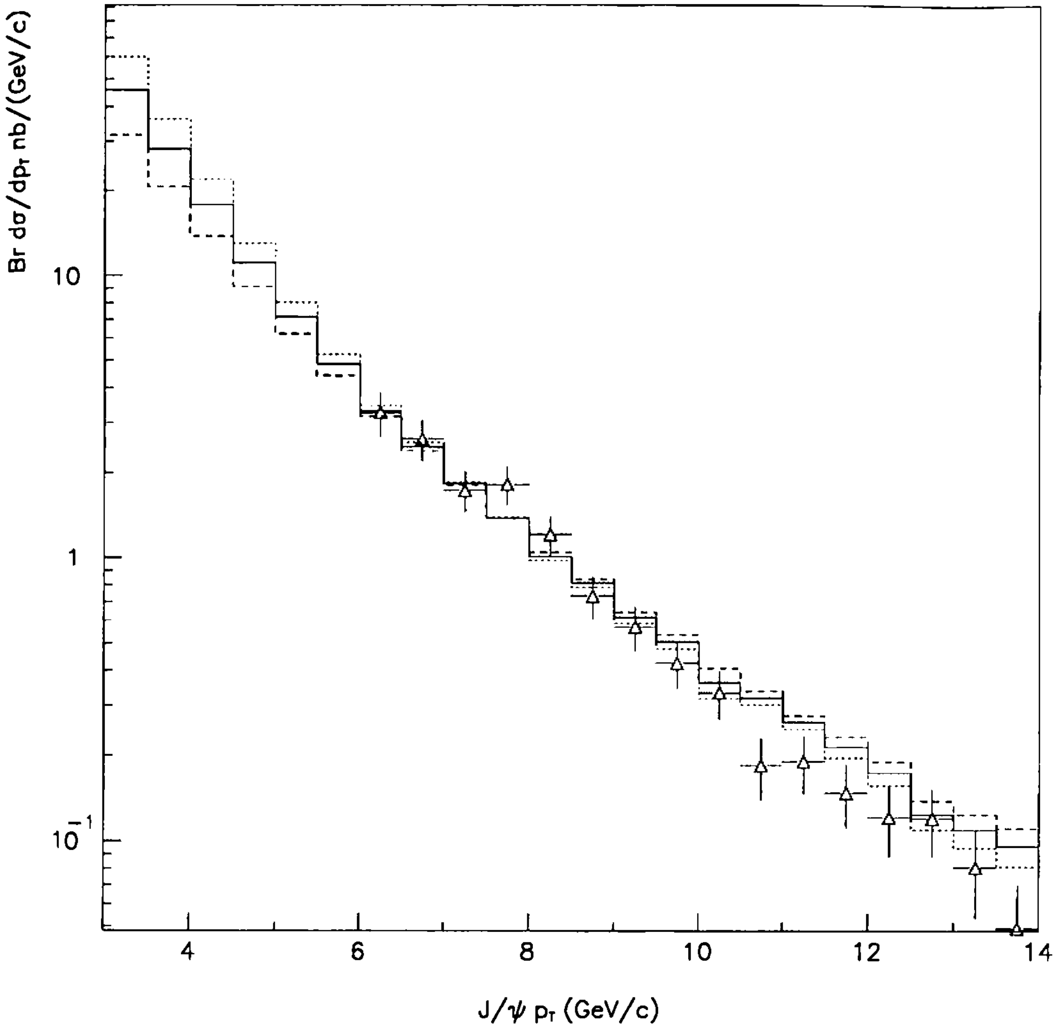

Figure 7.12: The Monte Carlo $p_T(J/\psi)$ spectrum compared to the data points from Reference [57]. The solid line was for the fraction of J/ψ from B decay equal to 0.63, the dashed line for 0.80, while the dotted line was for 0.46.

Chapter 8

Reconstruction of the χ_c Mesons

8.1 Selection of J/ψ Sample

The event selection for this analysis began with the definition of a J/ψ data sample from the decay $J/\psi \to \mu^+\mu^-$. This technique exploited the easily implemented $\mu^+\mu^-$ trigger. The identification of two muons from the decay of quarkonia produced an especially clean event sample. The J/ψ sample obtained was the starting point of many measurements at CDF. For instance, B to J/ψ decays have been reconstructed at CDF [11, 12]. Herein is presented the reconstruction of $\chi_c \to J/\psi\gamma$.

8.1.1 Definition of μ Candidates

Muon candidates were defined through a procedure which matched tracks in the CTC to stubs in the muon chambers. Such a matching produced a muon candidate because hadrons and electrons were not typically able to penetrate the 5.5 interaction lenghts of material between these detector elements, whereas a muon could. Also, track quality requirements on the relative positions and angles of the CTC track and muon chamber stub helped to further isolate the real muons from hadron punchthrough, particle decays and other fake events.

The uncertainty in the track matching after passage through the calorimeters was dominated by multiple Coulomb scattering for muons with momentum less than 20 GeV/c and by chamber resolution for muons of higher momenta. In a given amount of material of thickness, L, the angle of incident charged particles would be changed by multiple scattering to a Gaussian distribution centered on the initial angle. The width of this distribution was given by [4]

$$\sigma_\phi = \frac{13.6MeV/c}{\beta p} Z_{inc}\sqrt{L/L_R}[1 + 0.038\ \ln(L/L_R)]. \tag{8.1}$$

Here L/L_R was the number of radiation lengths traversed, p was the momentum of the particle, β was the ratio of the velocity of the particle to the velocity of light, $v/c = p/E$, and Z_{inc} was the charge of the incident particle, i.e. Z_{inc} =1 for muons.

For the material in CDF this reduced to [58]

$$\sigma_{I_x} = \frac{13.8cm}{p_T}\sqrt{0.59 + 0.41/sin\theta}. \tag{8.2}$$

Once energy loss in the calorimeter was taken into account, this became [58]

$$\sigma_{I_x} = \frac{13.8cm}{p_T}\sqrt{\frac{0.59 + 0.41/sin\theta}{1 - 0.71/p_T}}. \tag{8.3}$$

Upon including detector resolution effects, the final width of the matching in the x direction became [58]

$$\sigma^2_{I_x} = (\frac{13.8cm}{p_T})^2 \frac{0.59 + 0.41/sin\theta}{1 - 0.71/p_T} + (0.3cm)^2. \tag{8.4}$$

The first term in the above expression was due to multiple scattering. At a momentum of 4 GeV/c perpendicular to the beam direction its magnitude was about $(3.8cm)^2$. The second term was due to detector resolution effects. The momentum for calculating the expected spread in matching σ_{Ix} was calculated from the CTC helix parameters for the track associated with the CMUO. The width of the difference in slope in the x direction was expected to be

$$\sigma^2_{S_x} = (\frac{0.131}{p_T})^2 \frac{0.27 + 0.73/sin\theta}{1 - 1.43/p_T} + (0.0062)^2. \tag{8.5}$$

The width of the difference in the local CMU z position was calculated to be

$$\sigma^2_{I_z} = (\frac{13.8cm}{p_T})^2 \frac{0.59 + 0.41/sin\theta}{1 - 0.71/p_T} \frac{1}{(sin\theta)^2} + (1.5cm)^2. \tag{8.6}$$

Finally, the difference in slope in the z-y plane was calculated to have a width

$$\sigma^2_{S_z} = (\frac{0.131}{p_T})^2 \frac{0.27 + 0.73/sin\theta}{1 - 1.43/p_T} (sin\theta)^2 + (0.14)^2. \tag{8.7}$$

Muons with momenta less than approximately 1.43 GeV/c ranged out in the CDF detector, that is they stopped before reaching the muon chambers.

These variables were measured for CMUO's by propagating the CTC track to the associated CMU wedge. This propagation included the effects of the solenoid magnetic field value and radius, the geometry of the calorimeter, the expected return field, and the geometry of the central muon detectors. The difference in the propagated position and the measured stub position defined the matching variables. The difference in local CMU coordinates in the x direction was I_x, and I_z in the local z direction. The difference in expected slope in the x-y plane relative to that of the stub was S_x, and S_z in the z-y plane.

A variable for determining the significance of the matching of the track to the muon stub was defined. This included alignments of the detector elements and values of the return fields. The significance of the matching in the x-y plane was defined as

$$M_{I_x} = \frac{I_x}{\sigma_{I_x}}. \qquad (8.8)$$

The significance for z-y matching was

$$M_{I_z} = \frac{I_z}{\sigma_{I_z}}. \qquad (8.9)$$

Studies indicated that fake muon tracks from hadron punchthrough and other sources generally had a poor matching in several of these variables, so cuts on all of them were not required. Specifically, for the final muon identification, only the cuts $|M_{I_x}| \leq 3.0$ and $|M_{I_z}| \leq 3.0$ were needed. The efficiency of requiring events described by a Gaussian distribution to be within 3 σ of the mean was taken to be 99.73 %.

A small number of events were discarded due to a hardware problem. Occasionally, an ADC overflow in the z determination for the CMUO occured which meant the z coordinate could not be determined. For the sake of event sample purity such tracks were eliminated. The efficiency including CMUO reconstruction and no ADC overflow was determined to be 96.7 ± 0.7 %.

These cuts gave a muon sample definition. Since J/ψ candidates were the tag for the signal, events with 2 muon candidates as defined above were examined.

8.1.2 Dimuon Sample

The analysis started by identifying two muon candidate tracks which came from the decay of a J/ψ meson. An algorithm to loop over all muon candidate pairs was used for this identification. All dimuon combinations with opposite charge were examined for consistency with the hypothesis that they came from a J/ψ decay.

First, each muon candidate's CTC track was associated with a z vertex in the track reconstruction. Both muon candidate tracks were required to be associated with the same vertex number so tracks from different interactions would not fake a J/ψ signal. Additional cuts were motivated by the specifics of the trigger and the understanding of the trigger efficiency.

Data selection included a trigger requirement. The CDF trigger system has been discussed in detail in Chapter 4. CDF ran with a complex trigger table involving many triggers, some of which used information from the central muon chambers. For J/ψ reconstruction, the dimuon_central_3 trigger was used. All events for this analysis were required to have passed the dimuon_central_3 trigger.

As previously noted (see Chapter 4), the dimuon_central_3 trigger started with the level one central_muon_3 trigger, which was a 3 GeV/c single muon trigger. The transverse momentum was determined using the beam constraint described in Section 5.2. The efficiency of this trigger plateaus at about 92 ± 3 % for $p_T > 6.0$ GeV/c. (Figure 4.2). This motivated a cut of 3 GeV/c for the transverse momentum of all muon candidates obtained from the data which passed the dimuon_central_3 trigger. This was the first cut motivated by an understanding of the trigger.

The level 2 dimuon_central_3 trigger chose "gold muons" (defined in Chapter 4) in the hardware decision making process. Since any measurements obtained with this trigger relied on an understanding of the efficiency of the trigger, only events which contributed to the level 2 trigger were used to form J/ψ candidates. All muon candidates were required to fall in a wedge tagged as a gold muon wedge.

A wedge geometry cut was motivated by the trigger. As noted previously, the gold muon wedges were clustered for use in the dimuon_central_3 trigger. This resulted in events with muons in neighboring wedges not causing the level 2 trigger to latch. The dimuon efficiency was understood only for dimuons that helped the event pass the trigger. For instance, in events with 3 or more muons, the number of dimuons contributing to the trigger cross section could have been overestimated unless the gold muon wedge requirement was applied. Therefore, the muon pairs in consideration were required to not be in adjacent wedges. The definition of adjacent was the same as for gold muon wedge clustering. Muons were considered adjacent if they were in the exact same wedge, or although in different wedges in η they were the same in ϕ, or if in the same η side they were in the next wedge over in ϕ. The dimuons that pass these requirements would have caused the trigger to latch.

As seen in Chapter 7, the efficiency for J/ψ reconstruction dropped off significantly for values of pseudorapidity above $\eta = 0.5$ (Figure 7.4). Because the efficiency should be well understood for any analyis using J/ψ candidate events, all dimuon events were required to have a dimuon pseudorapidity in the region $|\eta| \leq 0.5$.

These cuts gave a sample of dimuon events for which the trigger efficiency was understood. The cuts are summarized here: 1) The position matching of the muon stubs with the associated CTC tracks was required to be measured and $\leq 3.0\sigma$ in both (x, y) and (z, y) views. 2) The 2 muon candidates must have opposite charge. 3) The tracks of the 2 μ candidates must be associated with the same z vertex. 4) The event must have passed the dimuon_central_3 trigger. 5) The transverse momentum of each μ must be ≥ 3.0 GeV/c. 6) Each μ CMU stub must have fallen in a wedge tagged as a gold muon wedge. 7) The μ^+ and μ^- must have fallen into wedges which were not adjacent. 8) The dimuon pseudorapidity must have fallen in the region $|\eta| \leq 0.5$. The dimuon sample thus defined formed the basis of the data selection for the analysis described here. All pairs of tracks passing these cuts were thus identified as $\mu^+\mu^-$ events with high purity.

The resolution of the central tracking chamber was discussed in Section 5.2. The resulting error in the determination of transverse momentum was $\sigma_{p_T} = \sqrt{(0.0011 p_T)^2 + (0.0066)^2}$. The error on $cot(\theta)$ was $\sigma_{cot(\theta)} \simeq 0.003$. These track resolution effects dominated the resolution of a particle's momentum vector, $\mathbf{p}$. The momentum vector of each track, $\mathbf{p_i}$, could be found, and an energy could be calculated based on the assumption of the particle type and mass, $E_i = \sqrt{\mathbf{p_i} \cdot \mathbf{p_i} + m_i^2}$. A four-vector for any pair of tracks could then be defined, $\mathbf{p} = \Sigma \mathbf{p_i}$, $E = \Sigma E_i$, and a pair mass could be calculated, $M = \sqrt{E^2 - \mathbf{p} \cdot \mathbf{p}}$.

The dimuon mass was formed for all events passing the cuts described. Figure 8.1 shows the mass distribution in the region $2.9 \leq M \leq 3.3$ GeV/c^2. The J/ψ resonance is clearly seen. Also shown is a fit of a Gaussian on a constant background. Figure 8.2 shows the mass distribution in the region $3.5 \leq M \leq 3.9$ GeV/c^2 (without the above trigger requirements for more staticstics). The $\psi(2S)$ resonance is evident. Also shown is the fit of a Gaussian of the same width and a linear background. The widths of the Gaussians were the same because the detector resolution was much wider than the natural width of the J/ψ and $\psi(2S)$. The resolution determined from the Gaussian fit was 18 MeV/c^2. Figure 8.3 shows the mass distribution in the region $9.0 \leq M \leq 10.8$ GeV/c^2 (with some additional isolation requirements [59]). The individual Υ states (the $b\bar{b}$ $^3\mathrm{S}_1$ states in Figure 1.5 which can decay into $\mu^+\mu^-$) are clearly resolved in this Figure. Also shown is the fit of 3 Gaussians of the same width and a linear background. The fit allowed the number under each peak, the mass of each peak, and a common resolution width to vary. The resolution on the Υ states was 50 MeV/c^2. The masses found from the reconstruction of these resonances was a test on the mass scale of CDF, because they could be compared to the known values from other experiments. The fits to the J/ψ, $\psi(2S)$, $\Upsilon(1S)$, $\Upsilon(2S)$ and $\Upsilon(3S)$ returned mass values of 3.097±0.001, 3.687±0.007, 9.458±0.004, 10.02±0.01 and 10.36±0.01 GeV/c^2 respectively, in agreement with world average values for these particle masses [4] within uncertainties.

8.1.3 The J/ψ Signal Region

A J/ψ signal region was defined to identify the J/ψ events for further use in this experiment. The measured J/ψ mass was centered on 3.097±0.001 GeV/c^2, less than one σ from the

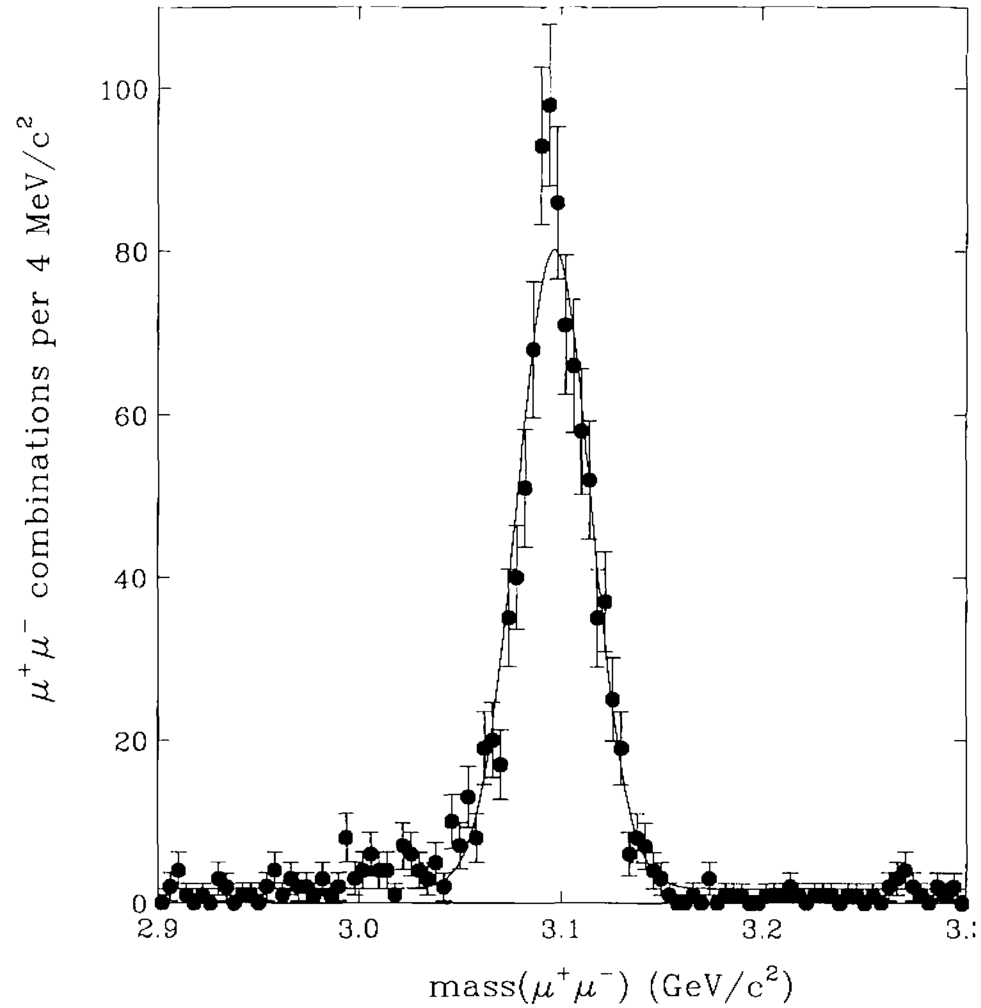

Figure 8.1: The J/ψ dimuon mass region

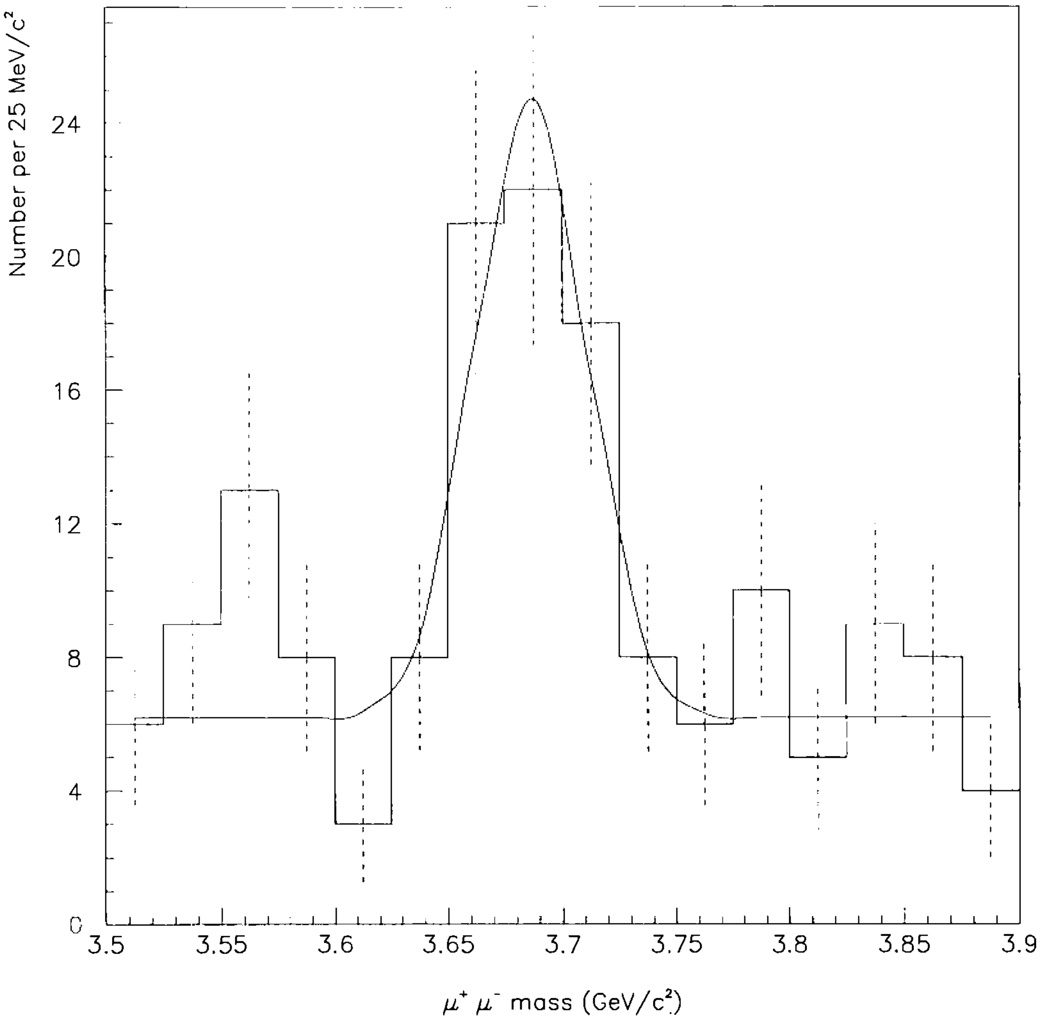

Figure 8.2: The $\psi(2S)$ dimuon mass region (without trigger requirements)

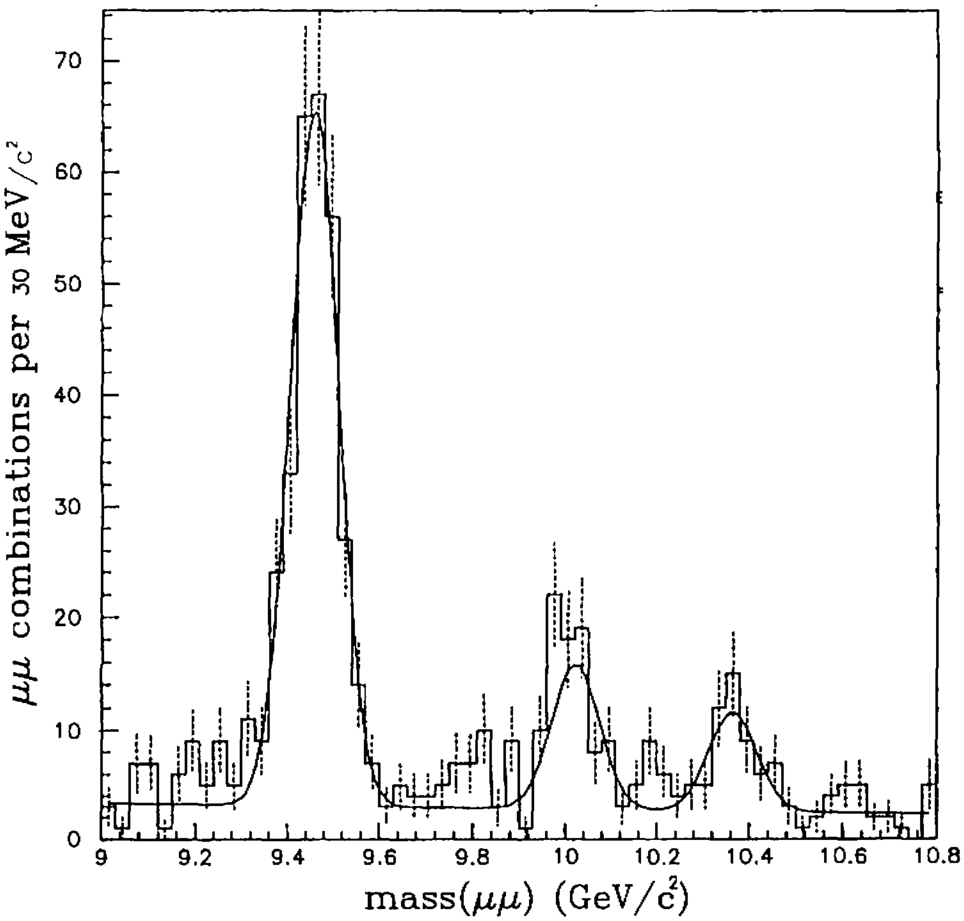

Figure 8.3: The Υ dimuon mass region (without trigger requirements, isolated muons)

world average, and had a resolution width of 18 MeV/c^2. A mass window for the J/ψ signal was defined from 3.05 to 3.15 GeV/c^2. This mass region is shown as the hatched area in Figure 8.4. For control, a background sample was obtained of dimuon candidates which were like those which could have faked the J/ψ signal. This sample came from the mass sideband regions defined as $2.90 \leq M \leq 3.00$ and $3.20 \leq M \leq 3.30$. The number of non-J/ψ events from the sideband regions was 90 ± 16 in a total window of 0.2 GeV/c^2. Multiplying this by the ratio of the J/ψ signal window width to sideband window width gives an expected background in the J/ψ window of 45 ± 8. Since there were 941 ± 31 events in the J/ψ candidate region, the number of true J/ψ mesons in the candidate sample was determined to be 896 ± 32. Another way to determine the number of J/ψ events was to fit the distribution to a Gaussian with a linear background. The result of this fit is shown in Figure 8.1. The Gaussian contribution corresponds to 907 ± 32 J/ψ events. These two results agree fairly well with one another.

Many measurements were made starting from this dimuon sample. These J/ψ candidates were used for the determination of the differential cross section of J/ψ events at Tevatron energies [57]. Also, they were used to reconstruct many decays, such as $\psi(2S) \rightarrow J/\psi\pi^+\pi^-$. In addition, the decays of heavy quark mesons were reconstructed, such as the decay $B_u^{+-} \rightarrow J/\psi K^{+-}$ [11], and $B_d^0 \rightarrow J/\psi K^{0*}$ [12]. Presented in this thesis is the reconstruction of $\chi_c \rightarrow J/\psi\gamma$.

8.2 Reconstruction of the Decay $\chi_c \rightarrow J/\psi\gamma$

Full reconstruction of the χ_c states required not only a J/ψ candidate, but a γ candidate as well. The central electromagnetic calorimeter, consisting of the CEM and CES was used to identify photons. These photon candidates were used in the χ_c analysis.

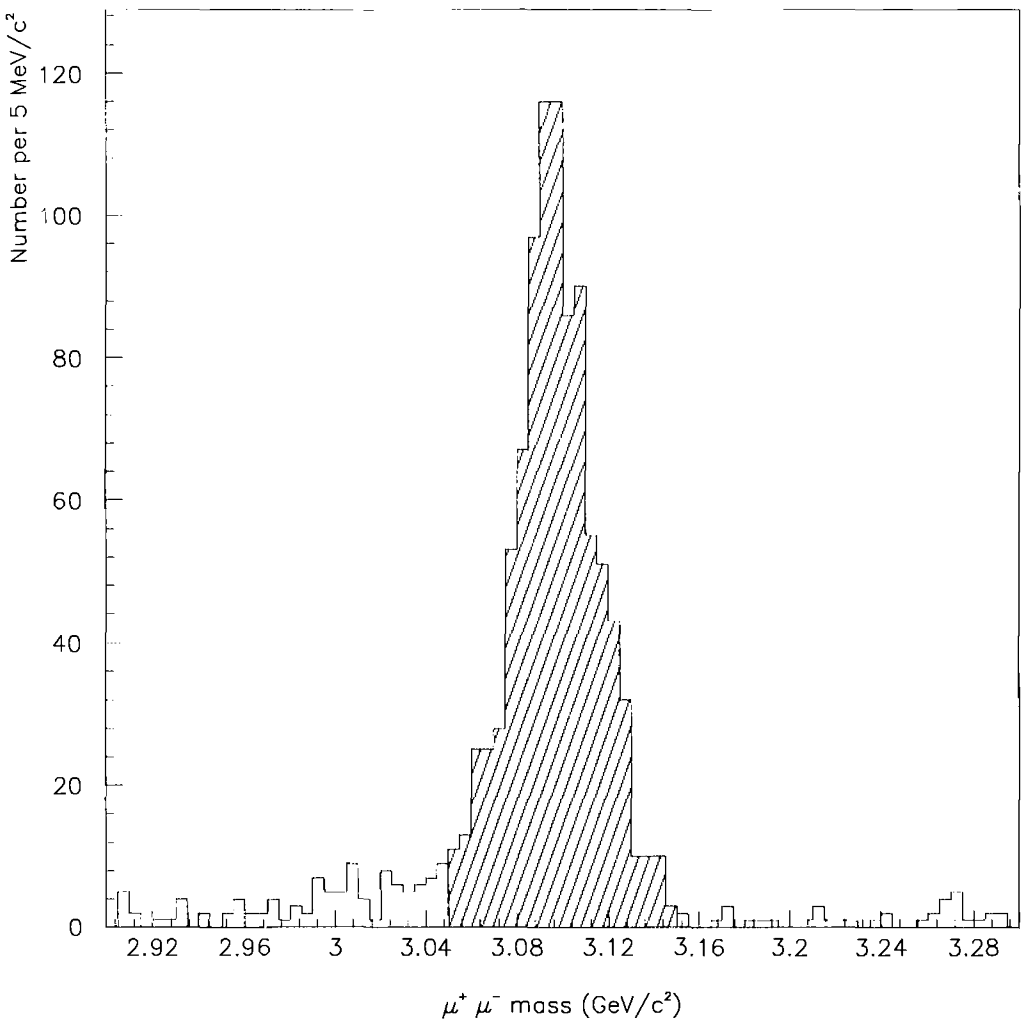

Figure 8.4: Definition of the J/ψ signal region

8.2.1 Photon Identification

A photon deposited energy in the form of a shower in the electromagentic calorimeter. The identification of such low energy γ events required here began with the energy in the CEM. "Low energy" was defined as well below the calibration energies of 10 to 50 GeV. After this, the position was found using the strip chamber (CES). The position, in combination with the determination of the primary vertex, also gave the γ candidate's direction. The direction and energy determined the momentum of the γ.

Photon identification began by finding electromagnetic energy. All central towers were examined for energy deposition. Since muons also deposited energy, towers which the muons traversed were excluded as possible γ candidate towers. The γ analysis was continued for towers with uncorrected energy greater than 0.7 GeV. This cut was the first criterion for isolation of a γ candidate sample. The value of 0.7 GeV was chosen because the efficiency for energies below this value dropped sharply. This was discussed in detail in Chapter 6.

Once a tower with at least the minimum energy was identified, a CES cluster match with the tower was performed. This cluster gave the position information for the γ candidate. The strip chamber measured the profile of the electromagnetic shower and the energy deposition at 6 radiation lengths into the calorimeter.

Associating a CES cluster to the calorimeter tower began by looping over the CES clusters, produced as noted in Section 5.5. The information calculated for such clusters included the cluster energy and the position of the cluster in the appropriate η or ϕ view. A CES cluster was required to be in the central region. The cluster was required to be in the same end of the calorimeter as the tower selected. Due to the geometry of the CES, the clusters were required to be in the same θ half module as the γ candidate tower. The clusters were also required to come from the same phi wedge as the tower. The fitted energy of the cluster for both the θ and ϕ view was required to be greater than 0. The CES clustering algorithm gave a fit position of the center of the shower. The closest cluster to the center of the tower for that view was considered to be the cluster arising from any activity in the tower. After the loop over the clusters, each view had associated with it a cluster that was closest to the center of the tower.

The photon candidate direction was defined as the direction vector from the beam position at the z vertex of the muons to the position of the CES cluster. The momentum vector of the photon was defined to have the magnitude of the corrected CEM energy and the direction of the direction vector defined above. The photon energy was taken as the corrected CEM energy. The momentum and energy thus defined were used as the momentum and energy of the photon candidate.

There were a few additional cuts on the γ candidates. First, the photon candidate energy was required to be greater than 1 GeV. This was motivated by the efficiency of the photon finding algorithm and the energy resolution (see Chapter 6). Second, for good measurement of energy, fiducial cuts were performed on the CES clusters. These cuts were used to exclude regions of the detector which would result in poor measurements, such as the edge of calorimeters, precisely as performed in Chapter 6. The clusters were required to be away from the wedge boundaries in ϕ, which corresponded to a requirement that the CES cluster position be within 21 cm of the center of the tower in $r - \phi$. In addition, the cluster was not used if it was too close to the boundary between the 2 ends, i.e. the crack at 90 degrees. This boundary was avoided by requiring that the cluster position in z be greater than 9 cm away from the $z = 0$ plane. Finally, only the first 6 towers on either side of $z = 0$ were used. This cut was motivated by an examination of the detector resolution at these extremely low energies (compared to the energies the CDF calorimeters were designed for), the expected photon distribution from $\chi_c \rightarrow J/\psi\gamma$ decays, and the occupancy of the detectors as the forward region was approached. As mentioned previously, the towers which the muons traversed were not used. A photon candidate sample with a well measured energy and momentum was thus ready to be combined with the J/ψ in each event. The energy distribution of these γ candidates is shown in Figure 8.5.

8.2.2 Formation of χ_c Candidates

The χ_c reconstruction then proceeded with the normal combination of 4-vectors. The χ_c candidate momentum vector was just the vector sum of the J/ψ candidate momentum and the γ candidate momentum. The energy of the χ_c candidate was taken as the sum of the J/ψ candidate and γ candidate energies. A mass for the system was then defined as

$$M = \sqrt{E_\chi^2 - \mathbf{p}_\chi \cdot \mathbf{p}_\chi} \tag{8.10}$$

There was a possibility of some common systematics in the mass combinations of the χ_c and the J/ψ candidates from any mismeasurements in the muon momenta. To minimize these systematics, a mass difference was used to define the χ_c signal region, defined as $\Delta M = \text{mass}(\mu^+\mu^-\gamma)$ - $\text{mass}(\mu^+\mu^-)$.

Figure 8.6 shows the resulting mass difference spectrum. The full range is visible for the ΔM distribution. There is an excess in the 0 to 1 GeV/c^2 bin which will be shown in the next figure to be explained by the presence of χ_c mesons. There is a smoother background distribution from electromagnetic activity in J/ψ events which rises slowly and then falls off above 4 to 5 GeV/c^2. Figure 8.7 shows the low mass region where the χ_c signal would appear. The peak due to $\chi_c \to J/\psi\gamma$ decays is clearly visible near $\Delta M \simeq 0.41$ GeV/c^2. Also shown is the ΔM spectrum for the J/ψ sideband region defined above, which was normalized to the relative mass($\mu^+\mu^-$) window used. No peaking at $\Delta M \simeq 0.41$ GeV/c^2 is seen in the sideband distribution. The ΔM distribution was then used for the final definition

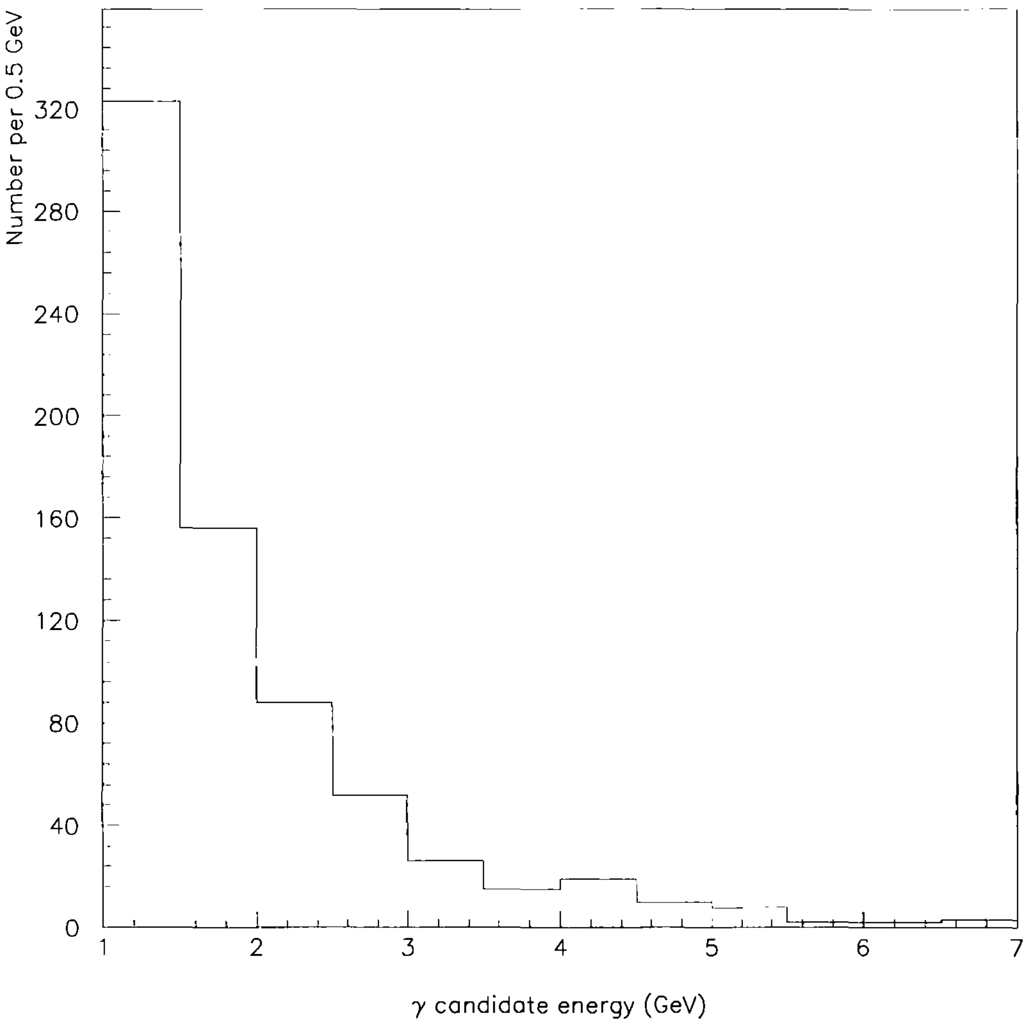

Figure 8.5: The photon candidate energy spectrum

of χ_c candidates.

8.2.3 Backgrounds

An examination of possible backgrounds in the ΔM spectrum was necessary to determine the number of reconstructed χ_c events. Since the contribution from the J/ψ sideband region was small, it was concluded that most of the background resulted from real J/ψ particles combined with other particles in the event.

The process $J/\psi\pi^0 \rightarrow J/\psi\gamma\gamma X$

The primary hypothesis as to the source of the background was that it was due to $J/\psi\pi^0 X$ where the π^0 decayed into $\gamma\gamma$ and one of these photons combined with the J/ψ. A background shape was found for this hypothesis by assuming that the kinematics of π^0's in these events would be well modeled by the kinematics of π^+ and π^-. Thus, J/ψ candidate events were used with tracks in the same event, assumed to be charged π's. A simple Monte Carlo was then applied for each pion candidate, treating the charged π momentum as a π^0 momentum. A simulated $\pi^0 \rightarrow \gamma\gamma$ decay at rest was used, and each γ was boosted into the π reference frame. The energy of the simulated photon as well as the position it would have in the central electromagnetic calorimetry was calculated.

The ΔM distribution was reconstructed as if the simulated photon were real. The energy of the simulated γ was required to be greater than 1 Gev. All the J/ψ requirements were the same as for the χ_c reconstruction. A geometric requirement that the photon would have hit in the same central region used above was applied. In addition, the distribution obtained was weighted by the photon efficiency (as determined in Chapter 6). The normalization depends upon the fraction of π^0 decays which send both photons into the same calorimeter tower (expected to be about 6% which would lead to an overestimate of the background rate),

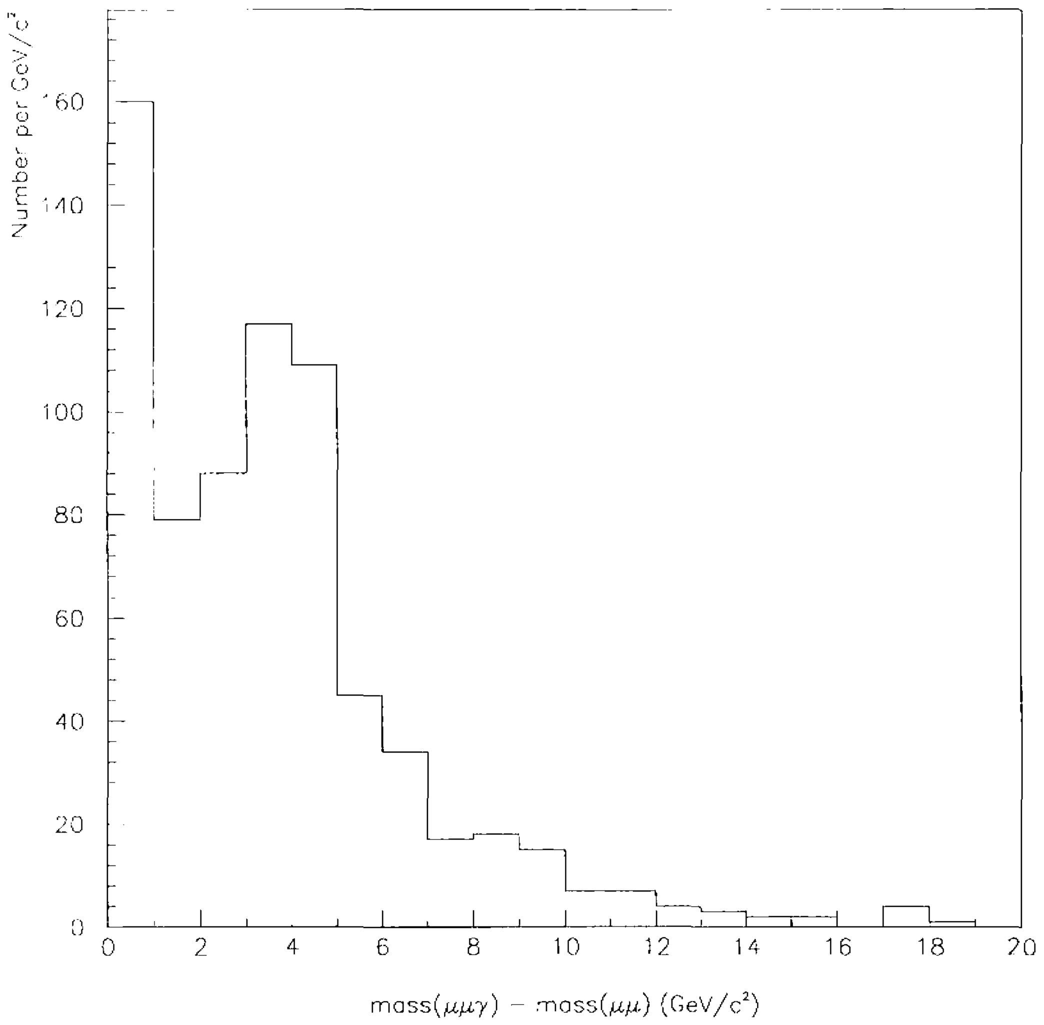

Figure 8.6: The ΔM distribution

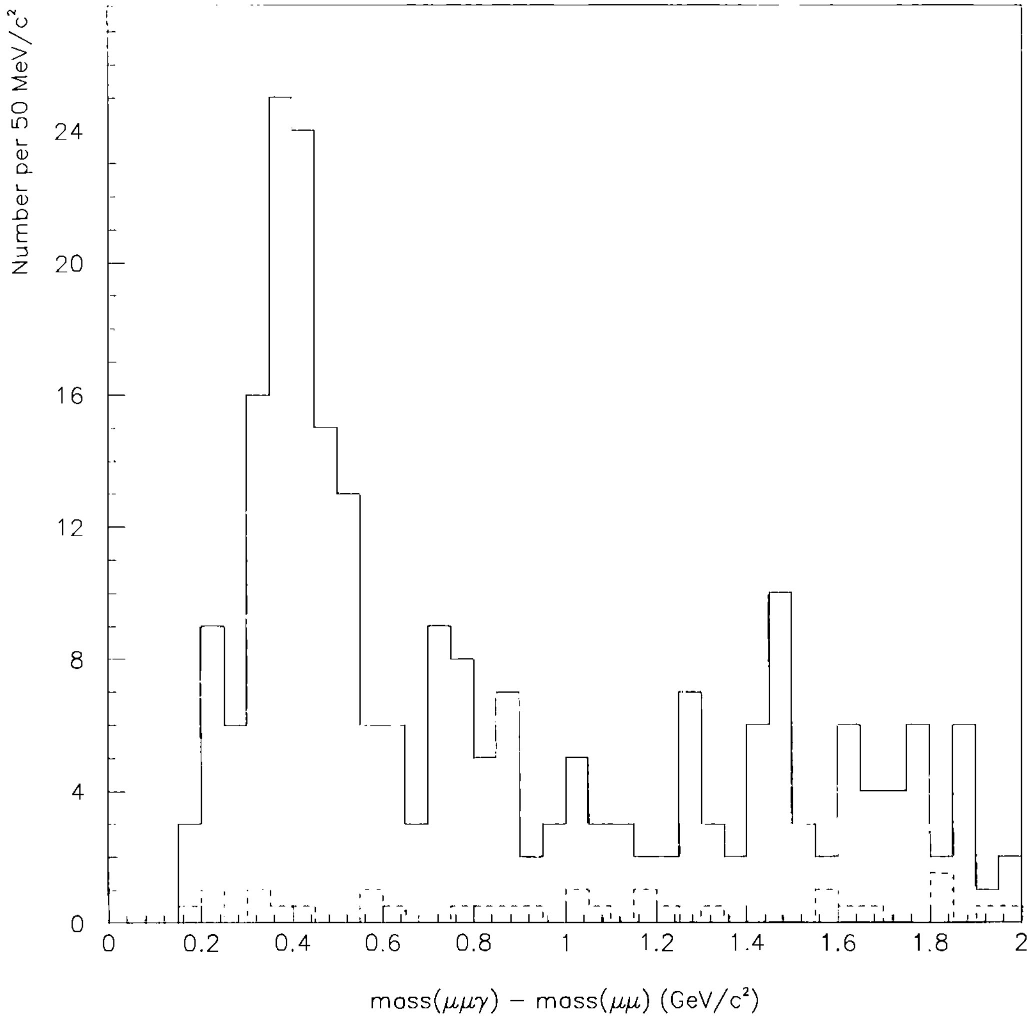

Figure 8.7: The ΔM distribution near the χ_c mass

function	p_1	p_2	p_3	p_4	p_5
$(p_1 + p_2 e^{p_3 x})(1 - e^{p_4(x-p_5)})$	3.1 ± 1.2	6.0 ± 3.7	1.4 ± 1.5	9.0 ± 6.5	0.11 ± 0.01
$(p_1 + p_2 x + p_3 x^2)(1 - e^{p_4(x-p_5)})$	7.7 ± 1.5	-4.6 ± 2.5	1.1 ± 1.0	10.6 ± 4.9	0.11 ± 0.01
$(p_1 + p_2 x)(1 - e^{p_3(x-p_4)})$	6.4 ± 0.5	-1.7 ± 0.4	14.3 ± 5.6	0.12 ± 0.01	
$(p_1 + p_2 x + p_3 x^2)\sqrt{x - p_4}$	15.5 ± 1.3	-14.4 ± 2.2	4.0 ± 0.8	0.117 ± 0.001	

Table 8.1: The functional fits to the background spectrum, x here is ΔM.

and the $K^{\pm}/\pi^{\pm}$ ratio (about 25% for the track momenta involved), leading to about a 75% scale factor. The simulated photon events were also weighted by this scale factor, to directly compare the background shape obtained with the data. Figure 8.8 through Figure 8.11 show the resulting simulated ΔM distribution, along with the functional fits shown in Table 8.1. This spectrum exhibits the behavior expected for the background under the χ_c peak, with a low, relatively flat plateau region for $1 < \Delta M < 2$ GeV/c^2, while at low ΔM having a shoulder which has no entries below $\Delta M = 0.1$ GeV/c^2. The amount of background in the plateau region was about 4 or 5 events per 50 MeV/c^2, comparing favorably to the same region in the signal plot. In Figure 8.12, this is compared to the signal.

The background obtained by the simulated photon method was then used to determine the number of χ_c events in the signal region. The background shape was paramaterized by different functional forms, summarized in Table 8.1.

Fake J/ψ events

Backgrounds arising from fake J/ψ events might also contribute to the background under the χ_c peak. If events were not J/ψ events, but passed all the muon and J/ψ requirements, they should also give similar shapes from the J/ψ mass sideband regions. The number of

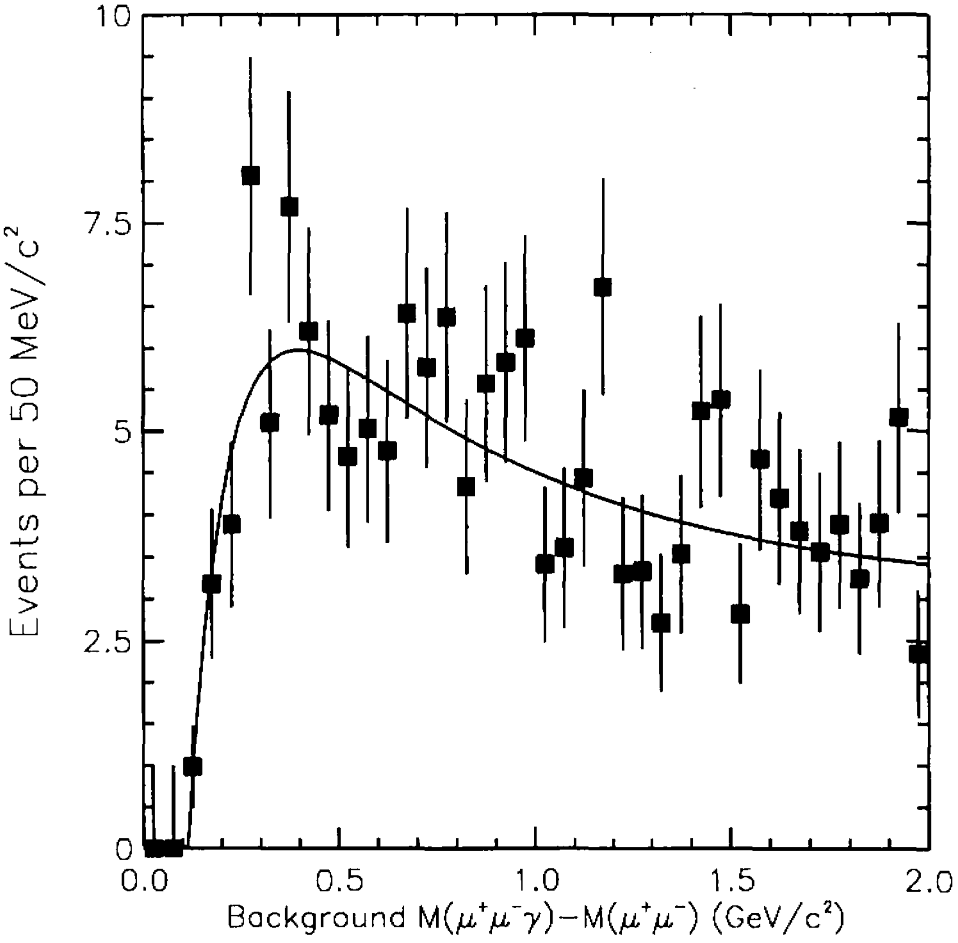

Figure 8.8: Background for the χ signal, fit with the first function in Table 8.1

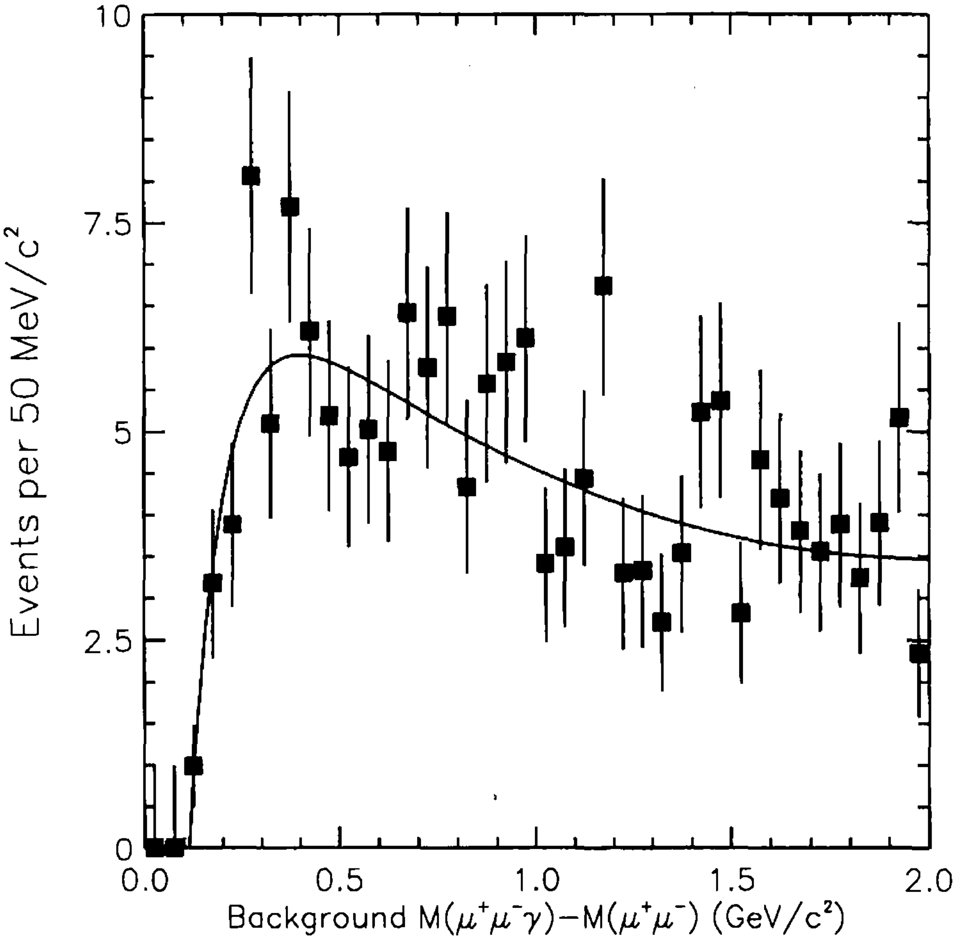

Figure 8.9: Background for the χ signal, fit with the second function in Table 8.1

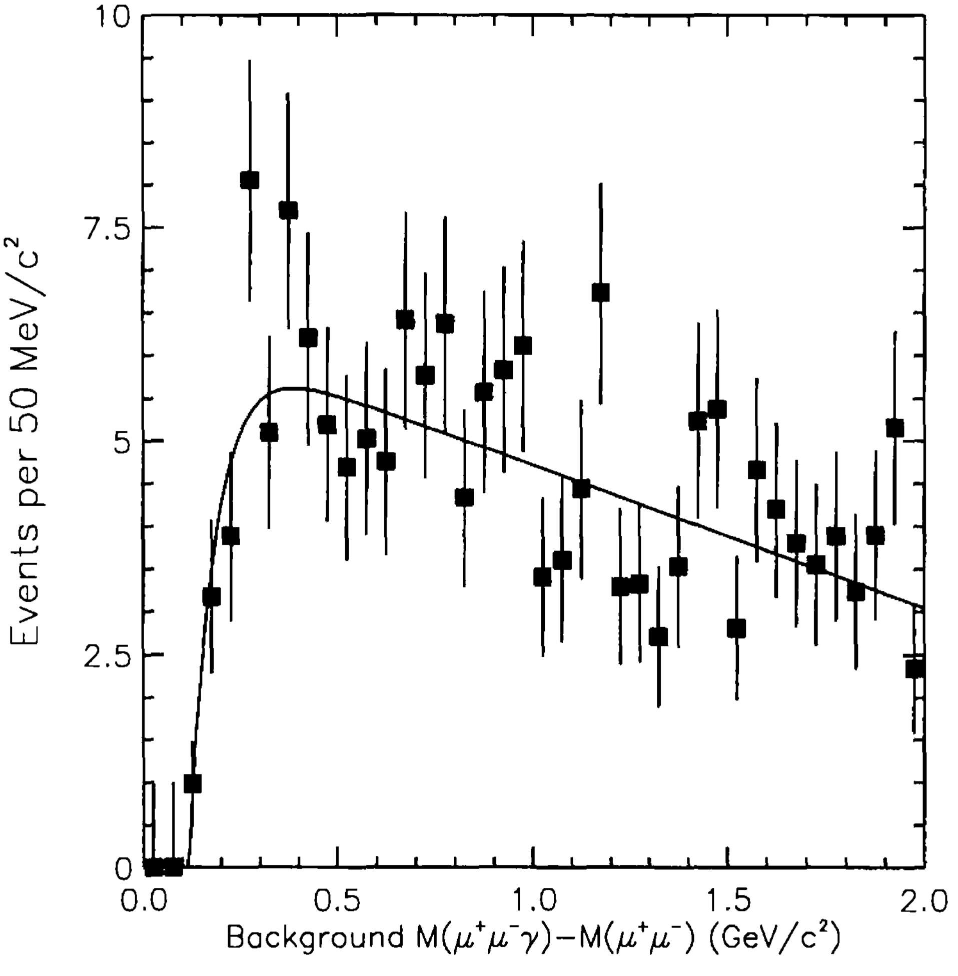

Figure 8.10: Background for the χ signal, fit with the third function in Table 8.1

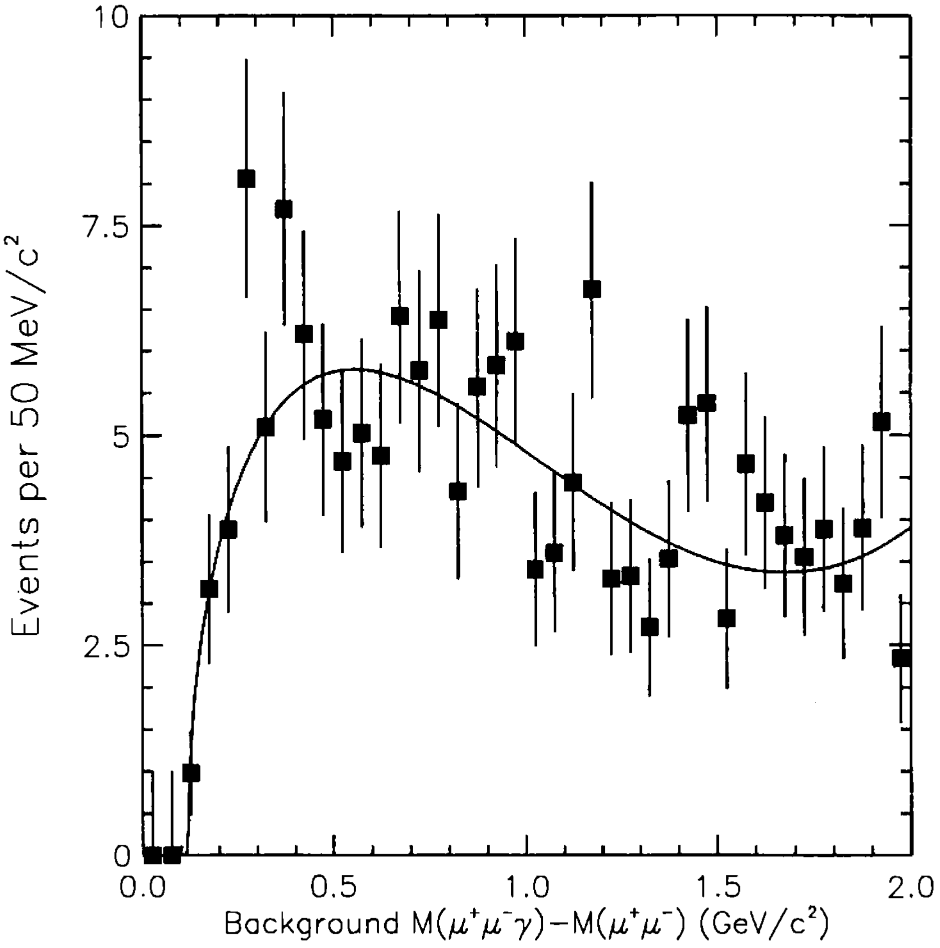

Figure 8.11: Background for the χ signal, fit with the fourth function in Table 8.1

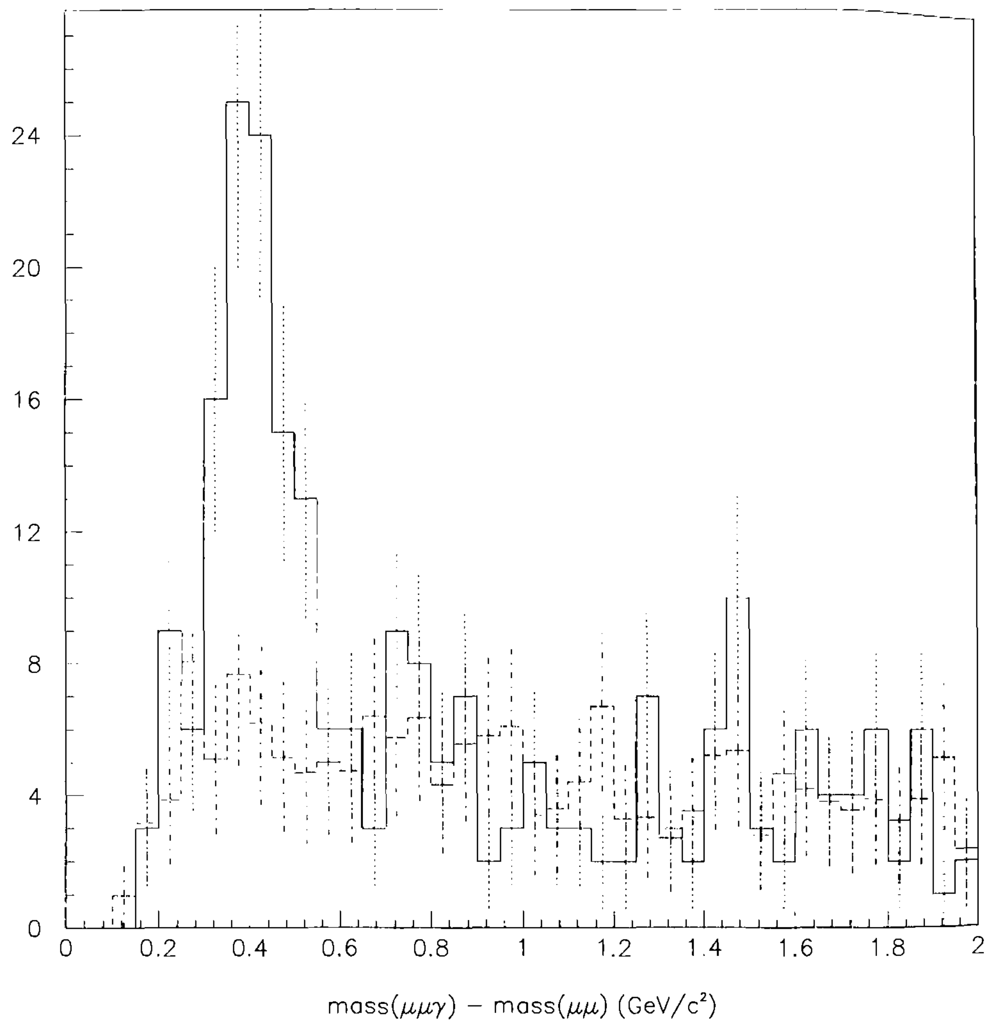

Figure 8.12: The χ signal and background distributions

events were shown to be small in Figure 8.7. This ΔM distribution from the J/ψ sideband regions is shown again in Figure 8.13 in a different scale. The events are normalized to the size of the dimuon mass window. It can easily be seen that the rates for this background is much smaller than for real J/ψ events including π^0 decays. Most importantly, however, the spectrum shows that no peak is produced in the χ_c region for this type of background.

Other sources of backgrounds

Other attempts to understand the background proved not as fruitful as the above. If the J/ψ is combining with activity from a jet, then flipping the J/ψ momentum around a jet axis would show the same background distribution, while smearing out the ΔM peak from real χ_c decays. However, the jet axis can only be well understood for jets with energy greater than 10 GeV or so. The dimuon data sample in the J/ψ region had very few jets above this energy, so there were not enough statistics to find a background curve. If the J/ψ momentum is merely flipped 180°, or combined with photon candidates from other events, the connection with jet activity in the event is lost. Such backgrounds have similar statistics to the signal, but are much flatter, and showed no peaking effect at small ΔM. They were not thought to describe the actual background production reliably. For these reasons, the $\pi^0 \rightarrow \gamma\gamma$ background hypothesis was the one used in this analysis to model the $\mu^+\mu^-\gamma$ candidate background.

8.2.4 The Number of Reconstructed χ_c Events

The number of χ_c events in the data sample was then determined by fitting the ΔM spectrum to a Gaussian signal over functions describing the background shape. The states χ_{c0}, χ_{c1},and χ_{c2} were not distinguishable due to the resolution. The part of the resolution

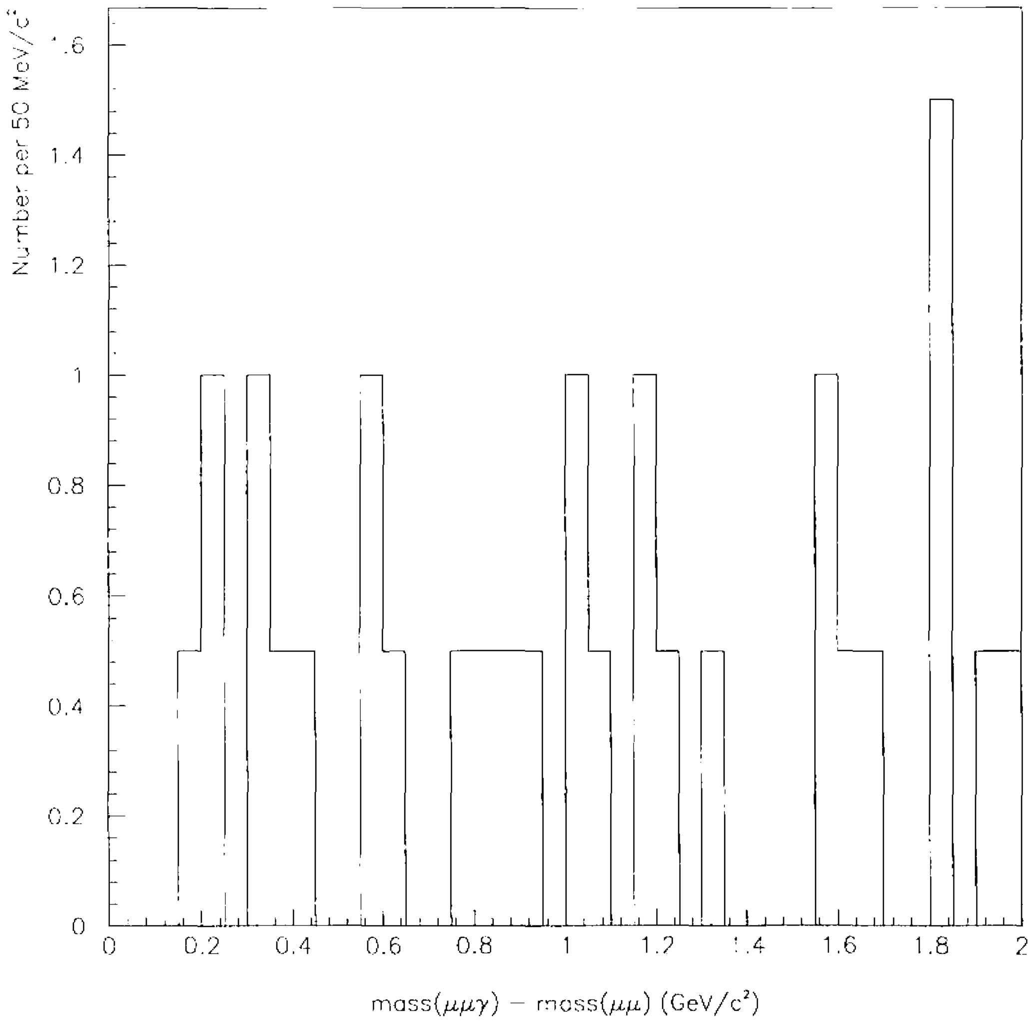

Figure 8.13: Background from the J/ψ sideband regions

expected due to photon energy resolution was

$$\frac{\sigma(\Delta M)}{\Delta M} = \frac{M_\chi + M_{J/\psi}}{2M_\chi}\frac{\sigma(E)}{E} \simeq (.942)(\frac{.18}{\sqrt{E}}) \simeq .16 \tag{8.11}$$

The energy resolution was determined in Chapter 6. The value of the expected resolution was calculated to be about 70 MeV/c^2. However, this was broadened by the fact that the different χ_c states have different masses. The ΔM for χ_{c0}, χ_{c1} and χ_{c2} mesons decaying to $J/\psi\gamma$ are 318.2, 413.6 and 459.2 MeV/c^2 respectively. Figure 8.12 shows the data with the background shape as determined in Section 8.2.3. A fit was also performed using a Gaussian for the χ_c signal. A Gaussian shape is used since the width of the distribution was dominated by the photon energy resolution. Fits to the signal with the paramaterizations of the background were performed, and the results are shown in Figure 8.14. The resolution for all the fits was around 70 MeV/c^2 as expected from the photon energy resolution contribution. These fits were averaged, and the number of χ_c events observed was taken as the average of 67 ± 8 (statistical) $\pm^{13}_{6}$ (systematic due to the fit). The systematic error was dominated by the uncertainty in the background shape. This number was then used in the subsequent cross section calculations.

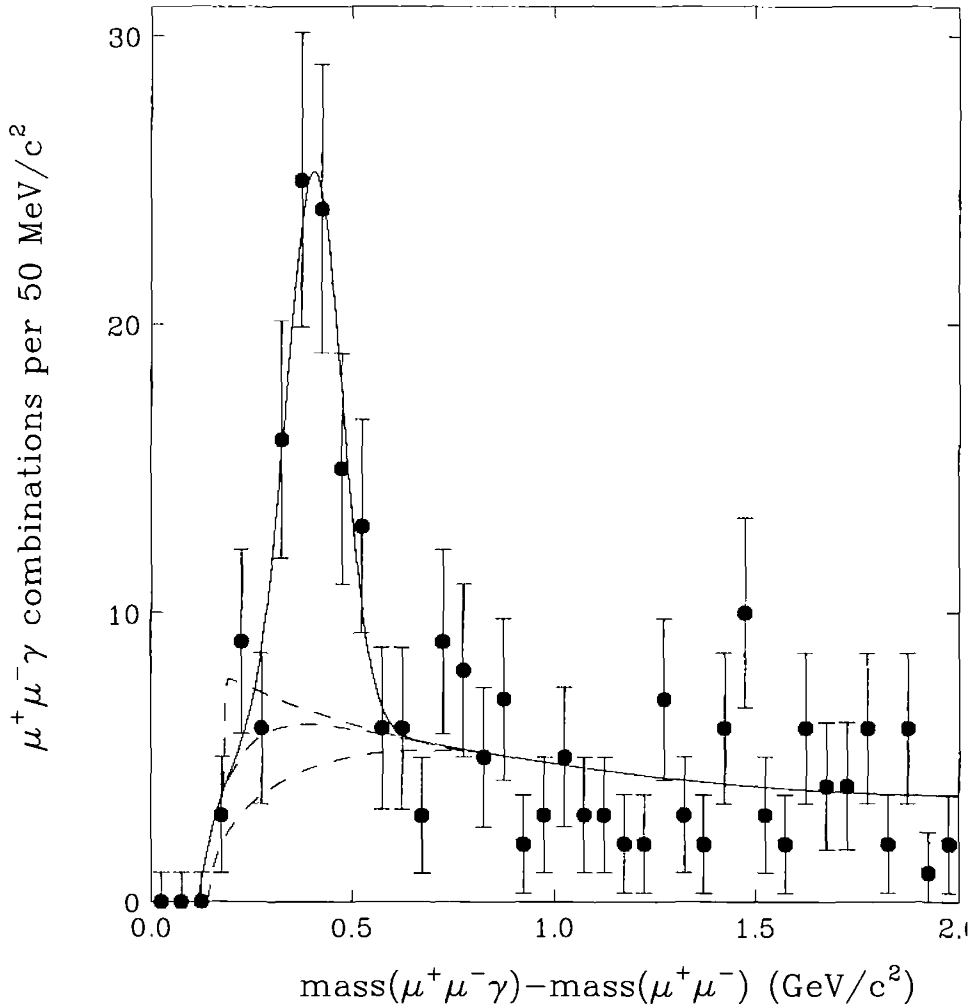

Figure 8.14: Fit of the χ_c signal

Chapter 9

Cross Sections

9.1 Inclusive χ_c Cross Section

This analysis was the first complete reconstruction of the χ_c mesons at Tevatron energies. The success of this χ_c reconstruction meant that the cross section times branching ratio could be found for the process $\chi_c \to J/\psi\gamma$, $J/\psi \to \mu^+\mu^-$. The cross section times branching fraction was calculated from the formula

$$\sigma(\chi_c \to \mu^+\mu^-\gamma) = \frac{N_{\chi_c}}{\epsilon L}. \tag{9.1}$$

Here $\sigma(\chi_c \to \mu^+\mu^-\gamma)$ was the cross section times branching ratio for the process $\bar{p}p \to \chi_c X \to J/\psi\gamma X \to \mu^+\mu^-\gamma X$, for the region $p_T(J/\psi) > 6$ GeV/c and $|\eta(J/\psi)| < 0.5$. The cross section was described in terms of the J/ψ momentum and pseudorapidity because some collider experiments previous to CDF could only fully reconstruct the J/ψ and theoretical predictions have listed the cross section calculations in terms of these variables. The observed number of χ_c mesons was termed N_{χ_c}, ϵ was the χ_c detection acceptance times efficiency, and L was the integrated luminosity. The cross section was calculated from the

Quantity	Uncertainty
N_{χ_c}	12% (stat), $^{+19\%}_{-9\%}$ (sys)
Luminosity, L	±7.7%
Efficiency, ϵ	±33%
Uncertainty in $\sigma(\chi_c \rightarrow \mu^+\mu^-\gamma)$	±0.4 (stat) $^{+1.2}_{-1.1}$ nb

Table 9.1: Summary of the uncertainties in the measurement of the χ_c cross section

values for each of the variables described in the previous sections:

$$\frac{N_{\chi_c}}{\epsilon L} = \frac{67 \pm 8 \pm^{13}_{6}}{(0.0079 \pm 0.0026)(2.6 \pm 0.2 pb^{-1})} \tag{9.2}$$

yielding

$$\sigma(\chi_c \rightarrow \mu^+\mu^-\gamma) = 3.2 \pm 0.4 \pm^{1.2}_{1.1} nb. \tag{9.3}$$

This result was the sum over the χ_c angular momentum states, since they could not be resolved. The first uncertainty was statistical and the second combined in quadrature the systematic uncertainties due to the fitting procedure, the efficiency calculation, and the luminosity measurement. These uncertainties are summarized in Table 9.1. To compare this cross section result with theoretical calculations, it was necessary to determine the relative fraction of the χ_c cross section which came from each of the possible production mechanisms outlined in Chapter 2. This determination is discussed below.

9.2 J/ψ Production

The observed χ_c sample was used in Equation 9.1 to measure the χ_c production cross section times branching fractions. This result in combination with the J/ψ production cross section measured previously by the CDF collaboration [57] (shown in Figure 7.12) could then be

Process		name for	partial cross section
$\bar{p}p \to b$-hadron $\to J/\psi$	consisting of	σ_1	
	b-hadron $\to \chi_c \to J/\psi$		σ_a
	b-hadron $\to \psi(2S) \to J/\psi$		σ_b
	b-hadron $\to J/\psi_{direct}$		σ_c
$\bar{p}p \to \chi_c \to J/\psi$		σ_2	
$\bar{p}p \to J/\psi_{direct}$	(including $\bar{p}p \to \psi(2S) \to J/\psi$)	σ_3	

Table 9.2: The contributions to the total J/ψ cross section

used to calculate the b-quark cross section. This calculation relied on the assumption that charmonia states are produced via a small number of known mechanisms. This calculation is outlined in this section. All partial cross sections discussed below include branching fractions and are for the kinematic region $p_T(J/\psi) > 6$ GeV/c, $|\eta(J/\psi)| < 0.5$. Most models of charmonia production [15, 9] include only the mechanisms shown in Table 9.2 as was discussed in Chapter 2.

Some relations are immediately apparent from the table. The first is that the b to J/ψ cross section, σ_1, is the sum of the three separate decay chains: $\sigma_1 = \sigma_a + \sigma_b + \sigma_c$. Second, the total cross section for J/ψ production, $\sigma(J/\psi)$ is $\sigma(J/\psi) = \sigma_1 + \sigma_2 + \sigma_3$. Third, the total cross section for the process $\chi_c \to J/\psi\gamma$, $\sigma(\chi_c)$ is $\sigma(\chi_c) = \sigma_2 + \sigma_a$. The parts σ_a, σ_b and σ_c were related to σ_1 by the respective branching ratios. These relations were the beginning point for the calculation of the b-quark cross section.

In the models referenced above, the production of J/ψ mesons proceeded primarily via the decay of χ_c mesons and b-hadrons. The calculations yielded $\sigma_3 \simeq (0.08)\sigma_2$ or less [9, 16]. This partial cross section was thus nearly negligible for the region $p_T(J/\psi) > 6$ GeV/c,

Constraint		
$\sigma(\chi_c) = \sigma_2 + \sigma_a$	$= 3.2 \pm 1.2$ nb	this analysis
$\sigma(J/\psi) = \sigma_1 + \sigma_2 + \sigma_3$	$= 6.88 \pm 1.11$ nb	Reference [57]
$\sigma_a/\sigma_1 = r_\chi$	$= 0.15 \pm 0.05$	Equation 2.8
$\sigma_3/\sigma_2 \sim r_{dir}$		

Table 9.3: Constraints on the relationships between the partial J/ψ cross sections.

$|\eta(J/\psi)| < 0.5$ at Tevatron energies. For lower transverse momenta, such would not be the case, since the direct cross section has a steeply falling spectrum with p_T and will be more significant for lower $p_T(J/\psi)$. The constraints in the partial cross sections are summarized in Table 9.3. The = signs in the table signify experimental measurements, while the $\sim$ signs signify assumptions from theoretical models. Solving for σ_1 and σ_2 yields

$$\sigma_1 \simeq \frac{\sigma(J/\psi) - (1 + r_{dir})\sigma(\chi_c)}{1 - r_\chi(1 + r_{dir})} \tag{9.4}$$

and

$$\sigma_2 \simeq \frac{\sigma(\chi_c) - r_\chi \sigma(J/\psi)}{1 - r_\chi(1 + r_{dir})}. \tag{9.5}$$

The results for σ_1 and σ_2 for different assumptions for r_{dir} are listed in Table 9.4.

At this point the assumption for the fraction of the J/ψ cross section from b-decay used in the efficiency determination in Section 7.3 could be checked. The fraction is defined as $f_b = \sigma_1/\sigma(J/\psi)$ and the results from this section yield

$$f_b \simeq \frac{\sigma_1}{\sigma(J/\psi)} = \frac{4.3 \pm 1.4}{6.88 \pm 1.1} = 0.63 \pm 0.17 \tag{9.6}$$

where is should be noted that some of the uncertainty is correlated. The value used for the efficiency determination was $f_b = 0.63$, which is consistent with Equation 9.6.

r_{dir}	J/ψ from b	J/ψ from direct χ_c
$r_{dir} = 0$	$\sigma_1 = 4.3 \pm 1.4$ nb	$\sigma_2 = 2.6 \pm 1.2$ nb
$r_{dir} = 0.085$	$\sigma_1 = 4.1 \pm 1.3$ nb	$\sigma_2 = 2.6 \pm 1.2$ nb
$r_{dir} = 0.17$	$\sigma_1 = 3.8 \pm 1.2$ nb	$\sigma_2 = 2.6 \pm 1.2$ nb
$r_{dir} = 1$	$\sigma_1 = 0.7 \pm 0.2$ nb	$\sigma_2 = 3.1 \pm 1.2$ nb
$r_{dir} = 1.15$	$\sigma_1 = 0$ nb	$\sigma_2 = 3.2 \pm 1.2$ nb

Table 9.4: Results for contributions to the total J/ψ cross section.

9.3 The b Quark Cross Section

The J/ψ cross section times branching ratios for the process $\bar{p}p \to b\text{-hadron}X \to J/\psi X$ was found in Table 9.4 to be $\sigma(b \to J/\psi \to \mu^+\mu^-) = \sigma_1 = 4.3 \pm 1.4$ nb. This was then used to determine the b-quark cross section. The method for this determination began with a model of b-quark production and subsequent production of b-hadrons. The decay of b-hadrons was simulated using measured J/ψ branching ratios and J/ψ momentum in the b-hadron rest frame (described below).

9.3.1 Evaluation of the b-Quark Cross Section

The J/ψ cross section arising from b-hadron decays gives no direct measurement of the initial b-quark momentum or direction. To measure the b-quark cross section, a b-quark p_T shape is assumed in order to calculate the efficiency for reconstructing the resultant J/ψ mesons.

By assuming the χ_c and B-meson decays constituted the total J/ψ production rate, the b-quark cross section could be determined from the above result and the measured J/ψ cross section. To convert the $B \to J/\psi$ rate into the b-quark cross section, it was multiplied by the ratio, R, of the b-quark cross section to the observed J/ψ cross section as determined using a Monte Carlo program, a full detector simulation and the same analysis as performed on the data:

$$\sigma^b(p_T^b > p_T^{min}, |y^b| < 1) = \frac{Br(J/\psi \to \mu^+\mu^-)\sigma(\bar{p}p \to J/\psi X) - \sigma(\chi_c \to \mu^+\mu^-\gamma)}{2Br(B \to J/\psi X|_{\mathrm{no}\chi_c})Br(J/\psi \to \mu^+\mu^-)} R. \quad (9.7)$$

Here

$$R = \frac{\sigma^b_{MC}(p_T^b > p_t^{min}, |y^b| < 1)}{\sigma^{J/\psi}_{MC}(p_T^{J/\psi} > 6 \text{ GeV}/c, |\eta^{J/\psi}| < 0.5)} \quad (9.8)$$

and $Br(B \to J/\psi X|_{\mathrm{no}\chi_c})$ is that part of the B to J/ψ decay which does not include χ_c intermediate states. The value of p_T^{min} was chosen such that approximately 90% of the Monte Carlo J/ψ events originated from b-quarks with $p_T^b > p_T^{min}$ following Reference [60]. We found $p_T^{min} = 8.5$ GeV/c. The Monte Carlo program generated b-quarks according to the p_T and rapidity distributions provided by Nason, Dawson, and Ellis [23], and fragmented the b-quark into mesons using the Peterson fragmentation model [24]. The J/ψ momentum spectrum in the B rest frame was taken from ARGUS data [61] (See Table 9.5). These data were fit to a 4th order polynomial for use in Monte Carlo generation of the appropriate spectrum.

Evaluating Equation 9.7 yielded the result $\sigma(b) = 12.0 \pm 4.5$ μb for $p_T^b > 8.5$ GeV/c and $|y^b| < 1$. The calculation is summarized in Table 9.6. The value of $\sigma(b)$ relies on the assumption that direct J/ψ production is negligible. If this assumption is changed to one in which direct production accounts for 9% of the J/ψ mesons then the value for $\sigma(b)$ drops by 6%. It would be difficult to quote a systematic uncertainty until this portion was measured, so the cross section was quoted given the assumption that direct production was negligible. However, if the direct J/ψ and $\psi(2S)$ contributions to the total J/ψ cross sections were shown to be non-negligible (as some gluon fragmentation models hold [62]), this result would be suspect for both the J/ψ and $\psi(2S)$ data points.

Momentum of J/ψ GeV/c	$\frac{d\sigma}{dp}$ (arb. units)
0.375 ±0.125	0.089 ± 0.021
0.625 ±0.125	0.116 ± 0.034
0.875 ±0.125	0.149 ± 0.036
1.125 ±0.125	0.199 ± 0.041
1.375 ±0.125	0.169 ± 0.036
1.625 ±0.125	0.225 ± 0.045
1.875 ±0.125	0.057 ± 0.033

Table 9.5: Momentum of the J/ψ in the B rest frame.

Table 9.6: Calculation of b-quark cross section.

$Br(J/\psi \rightarrow \mu^+\mu^-)\sigma(\bar{p}p \rightarrow J/\psi X)$	6.88±1.11 nb [57]
$\sigma(\chi_c \rightarrow \mu^+\mu^-\gamma)$	3.2±1.2 nb
$Br(J/\psi \rightarrow \mu^+\mu^-)$	5.97±0.25%
$Br(B \rightarrow J/\psi X\|_{\mathrm{no}\chi_c})$	1.1±0.2%
R	4.28±0.02
σ^b, $p_T^b > 8.5$ GeV/c, $\|y\| < 1$	12.0±4.5 μb

Chapter 10

Conclusions

The purpose of this work was to perform a measurement of the χ_c meson cross section at $\bar{p}p$ interactions, and compare this to the cross section calculated within the theoretical framework outlined in the first two chapters. The b-quark cross section was also determined as a by-product, due to the shared J/ψ possible in the final state of χ_c and b-hadron decays. In this chapter, the measurements are compared to the calculations, and conclusions on the efficacy of the predictions are arrived at. First, the χ_c cross section (central to this work) is examined below, then the b-quark cross section is briefly discussed.

10.1 χ_c production theory

The portion of χ_c meson production cross section not arising from b-hadron decays (decaying into J/ψ mesons with $p_T(J/\psi) > 6$ GeV/c and $|\eta(J/\psi)| < 0.5$) was determined from Table 9.4 to be 2.6 ± 1.2 nb. The theoretical estimate of this same cross section, assuming a K-factor of 2.0 (as at lower energies [9, 20]) and $Q^2 = (p_T^2 + m_\chi^2)/4$, was 2.8 nb, in agreement with the actual measurement. If the assumptions for the value of Q^2 was changed to $(p_T^2 + m_\chi^2)$, the estimate was lowered to 1.4 nb, still within the uncertainties of the measurement. Within the precision of the measurement performed in this analysis, the model proved useful for describing the production process. However, some concerns with the model still exist. Some of these are discussed below.

A K-factor of 2.0 may indicate that each additional term (an order higher in α_s) may be of a similar magnitude to the entire cross section. Thus, the model would be outside a regime where perturbative calculations could be trusted, and the ability of the calculation to arrive at the measured value may have been serendipitous, or the higher order terms could significantly alter the expected p_T and η shapes of the production cross section.

Another concern is the value chosen for Q^2. A naive approach might indeed be to choose the approximate energy of the χ_c divided by the number of initial partons as an approximate magnitude for $|Q|$. But the possibility exists that the dividing factor of 4 in $Q^2 = (p_T^2 + m_\chi^2)/4$ is indicative of a problem with the scale Λ used in the α_s calculation. In addition, some choices of Q^2 have a different p_T dependence, which would again alter the calculated p_T spectrum of χ_c meson production.

Additionally, the theoretical calculations give direct J/ψ production estimates significantly less than χ_c or b-hadron to J/ψ processes. Although the direct χ_c cross section does not depend significantly upon this ratio (being bounded from 2.6 ± 1.2 to 3.2 ± 1.2 nb as seen in Table 9.4), at some future level of precision for measurements of this cross section this might pose a real concern.

As it stands, however, no major modifications of the framework for the calculation of χ_c mesons is now required. A QCD perturbative approach with reasonable assumptions has resulted in a match between calculations and χ_c mesons observed at $\sqrt{s} = 1.8$ TeV. This shows the success and usefulness of the model.

10.2 b-quark production

The b-quark cross section arrived at in this work (through the decay into final states containing J/ψ) was

$$\sigma(b, p_T^b > 8.5 GeV/c, |y^b| < 1) = 12.0 \pm 4.5 \mu b. \tag{10.1}$$

Other methods of estimating the b-quark cross section at CDF have also been employed, including from $\psi(2S)$ final states [57], inclusive lepton production (both electrons [63] and muons [64]) as well as full reconstruction of B mesons [11, 12]. These results are summarized in Figure 10.1, which also includes the α_s^3 calculation for the b-quark cross section as a function of the minimum b-quark p_T. The value obtained here (in Equation 10.1) was labelled the $J/\psi X$ point, since it was arrived at by the J/ψ production subtracting out χ_c mechanisms. This is consistent with the b-quark cross section estimated from $\psi(2S)$ production [57]. Both of these methods assume that direct production of J/ψ and $\psi(2S)$ are negligible. The other points on the curve do not rely on this assumption. It is useful to note that the calculated curve lies below the measurements. This poses a challenge to physicists, to find a variation to the model (possibly a new choice for Q^2, higher order calculations, or a new set of structure functions) to describe the measurements. The general shape is as expected, although more precise quantitative tests need to be made. The state of the model may not change much before it is as useful describing b-quark production as it is describing χ_c meson production.

10.3 Summary

The production of χ_c mesons was relatively well understood within the framework of perturbative QCD, a part of the standard model of particles and interactions. The calculations from this model are consistent with observations. While refinements continue to be made

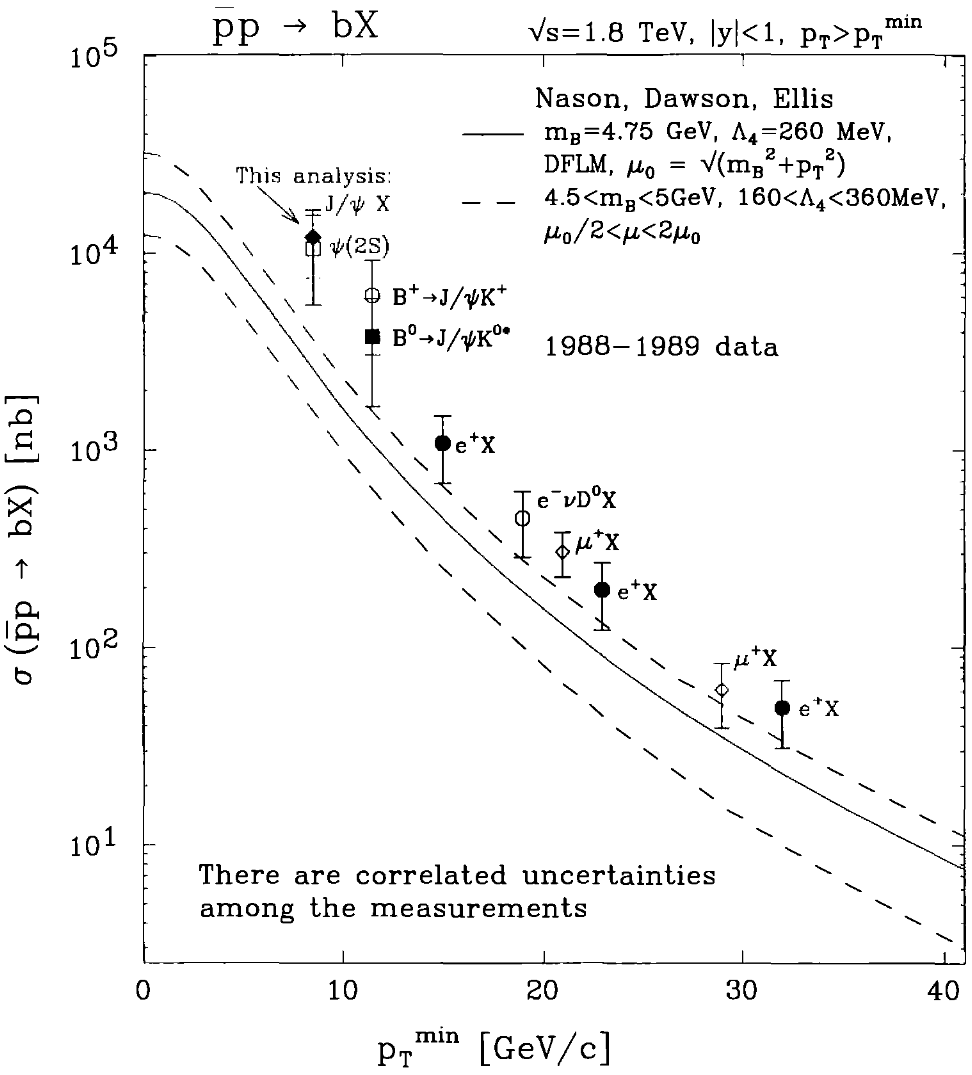

Figure 10.1: Results for the b-quark cross section

to the models, QCD remains a useful map of strong interactions.

Bibliography

[1] See, for example, *Genesis in Space and Time* and *No Final Conflict*, Francis Schaeffer, In "The Complete Works of Francis A. Schaeffer", Volume 2, p.3-148 Second Edition, 1986, Crossway Books, Westchester, Illinois, or, "Foundations of Christian Scholarship", Gary North, editor, 1979, Ross House Books, Vallecito, California.

[2] "The Structure of Scientific Revolutions", Thomas S. Kuhn, 1962, The University of Chicago Press, Chicago, Illinois.

[3] W. Weinberg, Physical Review Letters **19** 1264 (1967), A. Salam, *Elementary Particle Theory: Relativistic Groups and Analyticity* (8th Nobel Symposium) 367 (1968).

[4] Particle Data Group, K. Hidasa *et al.*, Review of Particle Properties Physical Review, **D 45**, 11 Part II (1992)

[5] J.-E. Augustin, *et al.*, Physical Review Letters **33** 1406-1408 (1974).

J.J. Aubert, *et al.*, Physical Review Letters **33** 1404-1406 (1974).

G.S. Abrams, *et al.*, Physical Review Letters **33** 1453-1455 (1974).

[6] T. Appelquist, *et al.*, Physical Review Letters **34** 365-369 (1975).

E. Eichten, *et al.*, Physical Review Letters **34** 369-372 (1975).

[7] S.W. Herb, *et al.*, Physical Review Letters **39** 252-255 (1977).

W.R. Innes, *et al.*, Physical Review Letters **39** 1240-1242,1640(E) (1977).

[8] Examples of the use of spectroscopic variables in atomic phenomena are listed in many textbooks, for example "Elementary Atomic Structure", G.K. Woodgate, 1980, Oxford University Press, Oxford.

[9] E.W.N. Glover, A.D. Martin, W.J. Stirling, Z. Phys. **C 38**, 473-478 (1988).

[10] E.W.N. Glover, F. Halzen, A.D. Martin Physics Letters **B 185**, 441-445 (1987).

[11] F. Abe, *et al.*, Physical Review Letters, **68** 3403-3407 (1992).

[12] *A Measurement of the B Quark and Neutral B meson Production Cross Sections in Proton-Antiproton Collisions at a Center of Mass Energy of 1.8 TeV* By Steve Vejcik, III (The Johns Hopkins University), UMI-93-13448-mc, Aug 1992. 175pp. Ph.D.Thesis.

[13] R. Baier, R. Ruckl, Z. Phys. **C 19**, 251-266 (1983).

[14] Z. Kunszt, *et al.*, Physical Review **D 21** 733 (1980).

[15] M Mangano, INFN Report No. IFUP-TH 2/93, 1993 (to be published).

[16] Nigel Glover, private communication.

[17] R. Baier, R. Ruckl, Nuclear Physics **B 208** 381-396 (1982).

[18] B. Humpert, Physics Letters **B 184** 105-107 (1987).

[19] R. Gastmans, W. Troost, Tai Tsun Wu, Physics Letters **B 184** 257-260 (1987).

[20] A.G. Clark, *et al.*, Nuclear Physics **B 142**, 29 (1978),

C. Kourkoumelis, *et al.*, Physics Letters **81 B**, 405 (1979).

C. Kourkoumelis, *et al.*, Physics Letters **91 B**, 481 (1980).

[21] T.A. Armstrong, *et al.*, Nuclear Physics **B 373** 35-54 (1992).

[22] A. Martin, R. Roberts, J. Stirling, RAL-92-021, DTP/92/16 (1992).

[23] P. Nason, S. Dawson, R.K. Ellis, Nuclear Physics **B 303** 607 (1988), Nuclear Physics **B 327** 49 (1989), Nuclear Physics **B 335** 260 (1990).

[24] C. Peterson, D. Schlatter, I. Schmitt, P. Zerwas, Physical Review **D 27** 105 (1983).

[25] D. Bortoletto, *et al.*, Physical Review **D 37** 1719 (1988).

[26] B. Gittelman, in *Proceedings of the Vancouver Meeting (1991 DPF Meeting)* (World Scientific, Singapore, 1991), p.181.

[27] L.M. Lederman, Scientific American **264** No.3 26-33 (1991).

[28] F. Abe, *et al.*, Nuclear Instruments and Methods **A 271** 387-403 (1988).

[29] S. Mori, *et al.*, Nuclear Instruments and Methods **A 238** 18-34 (1985).

[30] T. Kamon, *et al.*, Nuclear Instruments and Methods **213** 261 (1983).

[31] K. Yasuoka, *et al.*, Nuclear Instruments and Methods **A 267** 315-329 (1988)

[32] R.G. Wagner, *et al.*, Nuclear Instruments and Methods **A 267** 330-350 (1988)

[33] D. Amidei *et al.*, Nucl. Instrum. Methods A **267**, 51 (1988).

[34] T. Carroll *et al.*, Nucl. Instrum. Methods A **263**, 199 (1988).

[35] G. Ascoli *et al.*, Nucl. Instrum. Methods A **267**, 272 (1988).

[36] A. Gauthier, CDF internal note 937, 1989 (unpublished.)

[37] R. Hughes, *et al.*, CDF internal notes 1625 and 1385, 1991 (unpublished).

[38] G. W. Foster *et al.*, Nucl. Instrum. Methods A **269**, 93 (1988).

[39] Rick Snider, private communication

[40] Peter Berge, private communication.

[41] F. Abe *et al.*, Physical Review D, **43**, 2070 (1991).

[42] F. Abe *et al.*, Physical Review Letters, **68**, 3403 (1992).

[43] F. Bedeschi *et al.*, Nucl. Instrum. Methods A **268**, 50 (1988).

[44] R. Harris, CDF internal note 1329, (1991). See also F. Abe *et al.*, Fermilab Report No. Fermilab-PUB-92/01-E, 1992.

[45] F. Abe *et al.*, Physical Review Letters, **68**, 2734 (1992).

[46] K. Yasuoka *et al.*, Nucl. Instrum. Methods A **267**, 315 (1988).

[47] R. Wagner *et al.*, Nucl. Instrum. Methods A **267**, 330 (1988).

[48] F. Abe *et al.* Physical Review Letters, **63**, 720 (1989).

[49] M. Bozzo *et al.*, Phys. Lett. **147B**, 392 (1984).

[50] F. Abe *et al.*, Physical Review D **44**, 29 (1991).

[51] L. Balka, *et al.*, Nuclear Instruments and Methods **A267** 272-279 (1988).

[52] CDF internal note 1436 (unpublished).

[53] CDF internal note 1435 (unpublished).

[54] CDF internal note 1432 (unpublished).

[55] F. Paige, S.D. Protopopescu, ISAJET Monte Carlo version 6.36, BNL Report No. BNL38034, 1986 (unpublished).

[56] W. Wester, private communication.

[57] F. Abe, *et al.*, Physical Review Letters, **69** 3704-3708 (1992).

[58] D. Frei, CDF internal note 1430, 1991 (unpublished).

[59] C. Boswell, Minutes of the CDF dilepton meeting, January 23, 1992 (unpublished).

[60] N. Ellis, A. Kernan, Physics Reports **195** 23-125 (1990).

[61] H. Schroder, in *25th International Conference on High Energy Physics* Singapore, August 2-8, 1990, K.K. Phua and Y. Yamaguchi, editors, pp.846-849 (Volume II), published by South East Asia Theoretical Physics Association and the Physical Society of Japan, Distributed by World Scientific Publishing, Singapore.

[62] E. Braaten and T.C. Yuan, preprint NUHEP-TH-92-23 (UCD-92-25), (revised version) February 1993.

[63] F. Abe, *et al.*, Physical Review Letters **71**, 500-504 (1993).

[64] F. Abe, *et al.*, FERMILAB-PUB-93-145-E, June 1993, submitted to Physical Review Letters.

Christopher Mark Boswell

BIRTHPLACE: [redacted]

EDUCATION:

EDUCATION:	B.S.:	Seattle Pacific University, 1986.
	M.A.:	The Johns Hopkins University, 1988.
	Ph.D:	The Johns Hopkins University, 1993.

EXPERIENCE: Experimental High Energy Physics

Postgraduate Reasearch Scientist,
University of California, Riverside
Silicon Detector Group,
D0 detector at FNAL,
April 1993 to present.

Research Assistant, The Johns Hopkins University,
Silicon Vertex detector (SVX) group,
CDF detector at FNAL,
March 1989 to April 1993.
Silicon Strip Vertex Detector (SSVD) group,
Mark-II detector at SLAC,
July 1988 to March 1989.